

Cover Page



Universiteit Leiden



The handle <http://hdl.handle.net/1887/67080> holds various files of this Leiden University dissertation.

Author: Ridden, - Harper A.

Title: Inferno Worlds

Issue Date: 2018-11-21

Inferno Worlds

Proefschrift

ter verkrijging van
de graad van Doctor aan de Universiteit Leiden,
op gezag van Rector Magnificus prof. mr. C.J.J.M. Stolker,
volgens besluit van het College voor Promoties
te verdedigen op woensdag 21 november 2018
klokke 10:00 uur

door

Andrew Ridden-Harper
geboren te Christchurch, Nieuw-Zeeland
in 1991

Promotiecommissie

Promotores: Prof. dr. I. A. G. Snellen
Prof. dr. C. U. Keller

Overige leden: Prof. dr. H. J. A. Röttgering
Prof. dr. H. V. J. Linnartz
Prof. dr. M. Fridlund
Dr. D. M. Stam T. U. Delft
Dr. M. Min SRON

Cover design: An artist's impression of a hot rocky exoplanet that has a dust-tail. Cover designed by Andrew Ridden-Harper, using a false colour photograph of the Sun in ultra-violet wavelengths (credit: NASA Solar Dynamics Observatory) to represent the host star. The image of the planet was adapted from an artist's impression of 55 Cancri e (credit: ESA/Hubble, M. Kornmesser).

ISBN: 978-94-6323-396-5

© 2018 Andrew Ridden-Harper

*To my parents for their unwavering
support and encouragement.*

*“Imagination will often carry us to worlds that
never were, but without it we go nowhere.”
– Carl Sagan*

Contents

1	Introduction	1
1.1	Summary	1
1.2	Overview of the field	1
1.3	Planet formation	3
1.4	Hot rocky exoplanets	5
1.4.1	Sputtering	6
1.4.2	Possible mineral vapour atmospheres	6
1.5	Characterisation with spectroscopy	7
1.6	Disintegrating rocky exoplanets	8
1.6.1	Mass-loss mechanism	10
1.6.2	Dust particle dynamics	11
1.7	This thesis	13
1.7.1	Chapter 2	13
1.7.2	Chapter 3	14
1.7.3	Chapter 4	14
1.7.4	Chapter 5	14
1.8	Future outlook	15
2	Search for an exosphere in sodium and calcium in the transmission spectrum of exoplanet 55 Cancri e	19
2.1	Introduction	21
2.2	Observational data	24
2.2.1	UVES data	25
2.2.2	HARPS data	25
2.2.3	HARPS-N data	26
2.3	Data analysis	26
2.3.1	Processing of UVES spectra	26
2.3.2	Processing of HARPS and HARPS-N data	31
2.3.3	Combining the different data sets	31
2.3.4	Injection of artificial planet signals	32

2.4	Results	33
2.4.1	Sodium	33
2.4.2	Ionized calcium	35
2.5	Discussion and conclusions	36
3	Chromatic transit light curves of disintegrating rocky planets	47
3.1	Introduction	48
3.2	Method: The model	51
3.2.1	Dust dynamics code	51
3.2.2	Particle dynamics simulations	54
3.2.3	Ray tracing with MCMa3D	55
3.3	Results of simulations	58
3.3.1	Modelling the light curve of Kepler-1520 b with a low planet mass	58
3.3.2	Optically thick tail	62
3.3.3	Modelling the light curve of Kepler-1520 b with a planet mass of $0.02 M_{\oplus}$	69
3.3.4	Modelling the light curve of Kepler-1520 b with a planet mass of $0.02 M_{\oplus}$ and larger maximum height	70
3.3.5	Behaviour of large particles	75
3.4	Wavelength dependence	79
3.5	Constraints on particle ejection velocity	82
3.5.1	Particle trajectories	84
3.5.2	Constraint from the transit depth	86
3.5.3	Polarimetry	86
3.6	Discussion	88
3.6.1	Observational implications	88
3.6.2	Limitations of the model	88
3.6.3	High mass-loss rates	89
3.6.4	Constraints from dynamics	90
3.6.5	Plausibility of volcanic particle ejection mechanism	90
3.7	Summary	92
3.8	Appendix: Derivation of linear relationship between maximum tail height and vertical velocity	93
4	Self-shielding in dust tails of disintegrating rocky exoplanets	97
4.1	Introduction	98
4.2	Method: The model	99
4.3	Results and Discussion	101
4.3.1	General effects of self-shielding	101

4.3.2	Fitting the average transit of Kepler-1520 b with the self-shielding model	104
4.3.3	Reduction of the intrinsic sublimation rate	104
4.3.4	Short-time scale outbursts	107
4.3.5	Highly optically thick regime	112
4.4	Conclusions	112
4.5	Future outlook	115
5	Search for gas from the disintegrating rocky exoplanet K2-22b	117
5.1	Introduction	118
5.2	Observational data	119
5.3	Analyses	120
5.4	Synthetic planet signal injection	125
5.5	Results and discussion	126
5.5.1	Instantaneous gas-mass limits	126
5.5.2	Dust and gas mass-loss comparison	132
5.5.3	Important Caveats: high velocity gas	133
5.5.4	Alternative interpretations	136
5.6	Conclusions and future outlook	136
6	Samenvatting	143
6.1	Gas van hete rotsachtige planeten	143
6.2	Waarnemen van exoplaneet atmosferen	145
6.3	Stofstaarten	146
7	Summary	149
7.1	Gas from hot rocky planets	149
7.2	Observing exoplanet atmospheres	151
7.3	Dust tails	152
	Curriculum Vitae	153
	List of publications	155
	Acknowledgements	157

1 | Introduction

1.1 Summary

A remarkable population of short period transiting rocky exoplanets with equilibrium temperatures on the order of 2,000 K has recently been discovered. They have masses ranging from approximately $8 M_{\oplus}$, such as the hot super-Earth 55 Cancri e, to possibly that of Mercury or smaller, such as Kepler-1520 b. Their high temperatures make them very different to the planets in our Solar System. In particular, hot super-Earths are thought to have mineral atmospheres that are produced by the vaporisation of their surfaces, or large exospheres that are produced by sputtering of their exposed surfaces by intense stellar winds. Additionally, some smaller, low surface gravity hot rocky exoplanets have been found to be actively disintegrating and forming ‘comet-like’ dust tails that produce asymmetric transit light curves with forward scattering features.

These enigmatic objects inspire many questions such as: How did they form? How will they evolve? What is their composition and internal structure? What processes control their mass-loss?

Such fundamental questions can potentially be addressed to a far greater extent for hot rocky exoplanets than is currently possible for cooler rocky exoplanets because their atmospheres and released gas and dust can be observed, presenting the tantalising prospect of directly probing the composition of rocky planets.

The purpose of this thesis is to work towards answering these questions by searching for gas around hot rocky exoplanets with observational spectroscopy (Chapters 2 and 5), and by modelling the transit light curves produced by their ‘comet-like’ dust tails (Chapters 3 and 4).

1.2 Overview of the field

The first extra solar planetary system was discovered in 1992 (Wolszczan & Frail 1992) and consisted of a $2.8 M_{\oplus}$ and a $3.4 M_{\oplus}$ planet orbiting a millisecond radio pulsar. These planets could be identified because their orbits induce a variation in

the time-of-arrival of the pulsar’s pulses. Pulsar timings can be accurately measured, which enabled the signal of the planets to be detected. However, it is an exotic and unusual system, as pulsars have previously gone through a supernova explosion. The planets possibly formed from the remnants of the supernova explosion (e.g. Lin et al. 1991).

The era of mainstream exoplanet discovery started in earnest in 1995 with the discovery of a $\gtrsim 0.5$ Jupiter-mass planet orbiting the main-sequence star 51 Pegasi with an orbital period of 4.2 days, placing it well within the orbit of Mercury in our own Solar System. The existence of a Jupiter mass gas giant planet at such a short orbital distance came as a surprise because our Solar System only has gas giants at significantly larger distances. It is still not completely understood how these ‘hot-Jupiters’ form, however, the favoured models involve planetary migration (Dawson & Johnson 2018).

51 Pegasi b was discovered with the radial velocity method, which uses the fact that gravitationally bound objects orbit their common centre of mass. In a situation like a planetary system, where the host star is many orders of magnitude more massive than the planets, the centre of mass (or barycentre) is inside the star (but not at its centre). This means that the host star will exhibit small periodic changes in velocity, which can be described with a sinusoid of semi-amplitude, K , given by

$$K = \left(\frac{2\pi G}{P_{orb}} \right)^{\frac{1}{3}} \frac{M_p \sin(i)}{(M_s + M_p)^{\frac{2}{3}}} \frac{1}{\sqrt{1 - e^2}} \quad (1.1)$$

where G is the universal gravitational constant, P_{orb} is the planet’s orbital period, M_p is the mass of the planet, M_s is the mass of the host star, e is the planet’s orbital eccentricity and i is the planet’s orbital inclination (e.g. Wright 2017).

This equation shows that K is largest if the planet has a short orbital period and large mass, explaining its sensitivity to 51 Pegasi b. The inclination, i , is the angle between the normal of the planet’s orbital plane and the line of sight. Therefore, it is most sensitive to planets in near edge on orbits. Radial velocity measurements allow the planet’s mass to be determined if it is a transiting planet, since $\sin(i) \approx 1$.

In the years since the first detection of 51 Pegasi b, new technology and methods have enabled the discovery of smaller planets on longer period orbits. At the time of writing, there are 3735 confirmed exoplanets, of which 2327 were discovered by NASA’s Kepler Space Telescope¹, which monitored a field of about 150,000 stars to detect the periodic dimming caused by an orbiting planet transiting its host star (Borucki et al. 2010; Koch et al. 2010).

The transit depth is directly proportional to the fraction of the host star’s surface that is occulted by the planet. Assuming spherical stars and planets, this can

¹Retrieved from the NASA Exoplanet Archive.

be written as

$$\frac{\delta F}{F} = \frac{R_p^2}{R_s^2} \quad (1.2)$$

where F is the star's flux when the planet is not transiting, δF is the change in flux caused by the transit of the planet, R_p is the radius of the planet and R_s is the radius of the star. This makes it most sensitive to planets around small stars. For this reason, Earth sized planets in their host star's habitable zone have been detected around small M-dwarf stars (Gillon et al. 2017), but not yet around Sun-like stars.

The transit method also favours planets that have small orbital distances because it is more likely that they will transit their host star due to the geometry of the system. This can be written as the approximate relation

$$P_{tr} \approx \frac{R_s}{a} \quad (1.3)$$

where P_{tr} is the probability of the planet of orbital semi-major axis, a , transiting its host star of radius, R_s . Planets that have small orbital semi-major axes also have short orbital periods, allowing more transits to be observed. Transit depths are typically $\frac{\delta F}{F} \lesssim 1\%$ so repeated transits measurements are often necessary to overcome the noise and make robust detections. Also, more than one transit observation is needed to robustly determine the planet's orbital period.

After about four years of operation, the failure of two of Kepler's reaction wheels meant that it could no longer point accurately enough to continue its original mission. An alternative mission, called K2, was devised that uses Solar radiation pressure on the solar panels to assist with the stabilisation along the unguided axis. This involved reorienting the spacecraft so that it now observes fields along the ecliptic, spending approximately 75 days on each field (Howell et al. 2014). As a consequence, planets discovered by K2 are accessible to ground-based telescopes in both the Northern and Southern hemispheres. This enabled Chapter 5 of this thesis, which describes the use of the European Southern Observatory's Very Large Telescope (VLT) in Chile to observe K2-22 b.

1.3 Planet formation

Fig. 1.1 shows all the known exoplanets in planet-mass and orbital-period space, colour coded according to the method used for their discovery. The population has a large diversity in mass and orbital period that spans several orders of magnitude. The hot rocky exoplanets that are the focus of this thesis are in the lower-left corner of this diagram with orbital periods of less than a day and masses less than 0.025 Jupiter masses (8 Earth masses).

Planet formation theory has made much progress towards understanding the formation processes that lead to this diversity, however it is not yet completely understood. In the case of hot rocky exoplanets, key questions that are not yet answered include: Did they form at their current orbital distance (in-situ) or did they migrate there? If they did migrate, what triggered this migration? Could their formation process be related to that of hot-Jupiters? Are they the cores of hot-Jupiters that have lost most of their atmospheres? Or are they ‘failed hot-Jupiters’ that were not able to accrete a large amount of gas?

In general, planets are thought to be formed via two possible mechanisms:

1. The core accretion mechanism: dust and planetesimals in the proto-planetary disk coagulate until they reach a mass large enough to initiate a runaway accretion of gas onto the core that proceeds until the gas is dispersed by stellar winds when the star initiates nuclear fusion. (Pollack et al. 1996)
2. The disk instability mechanism: Instabilities in the disk produce over-dense regions that gravitationally attract the surrounding material, building up a planet (Boss 1997).

However, it is not likely that these mechanisms can operate at the orbital distances of short period planets, so migration is needed (e.g Schlichting 2014; Jackson et al. 2018; Dawson & Johnson 2018; Schlichting 2018). However, for hot super-Earths, the extent of this migration is not well understood and could be from <1 au to several au (Schlichting 2018).

The mechanisms proposed to cause migration are torques from gravitational interactions with the disk (e.g. Lin et al. 1996; Jackson et al. 2018) or gravitational interactions between planets (e.g. Chatterjee et al. 2008; Jackson et al. 2018). Interactions with the disk broadly fall into two categories: Type I migration is relevant for Earth-mass planets, such as those considered in this thesis, and results in migration rates that are proportional to the planet’s mass and the disk’s surface density. Type II migration is relevant for Jupiter-mass planets that have sufficient mass to clear an annular gap in the disk causing the planet’s motion to become linked to the viscous evolution of the gas (Ward 1997; Chambers 2009). Migrations from gravitational interactions between planets (planet-planet scattering) are most effective after the disk has dispersed because the disk can damp the gravitational excitations. Once free of the damping effect of the disk, tightly packed systems can rapidly induce high eccentricities in their orbits. Tidal interactions with the host star then act to circularise and shrink their orbits (e.g. Chatterjee et al. 2008; Jackson et al. 2018).

The atmospheres of hot super-Earths have likely evolved and undergone processing throughout their lifetimes. Even if a super-Earth currently has no atmosphere, it is expected to have gained and then lost a gaseous envelope tens of per-

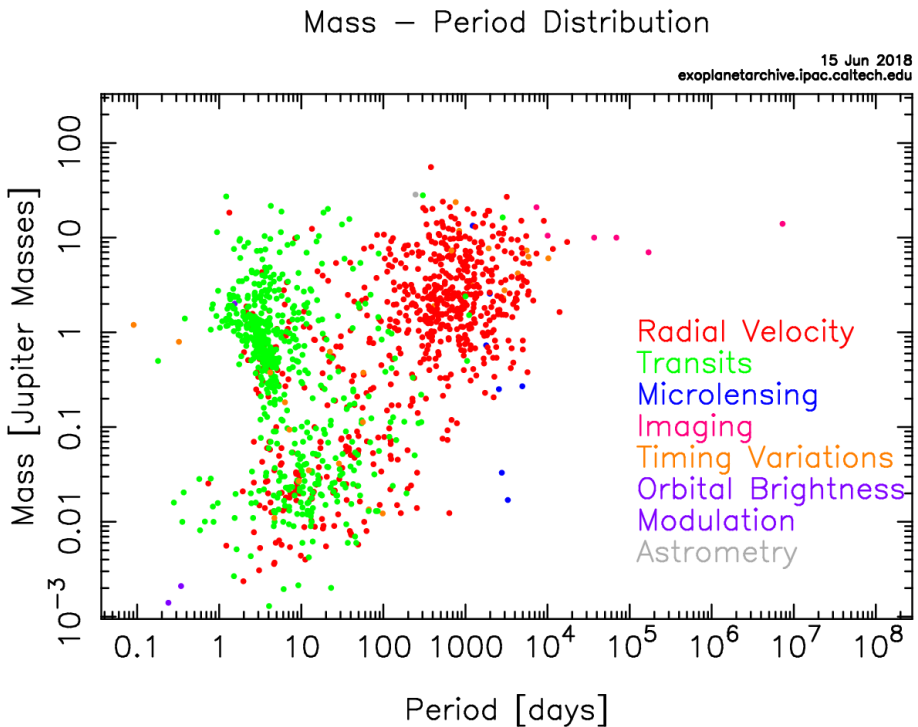


Figure 1.1: The distribution of all known exoplanets in planet-mass and orbital-period space, colour coded according to the method that was used for their discovery. Image credit: NASA Exoplanet Archive.

cent of its core mass, during its formation process (Schlichting 2018). This relates them to the formation of hot-Jupiters, suggesting that they would have become hot-Jupiters if they could have accreted more mass.

1.4 Hot rocky exoplanets

Ultra-short period (< 1 day) rocky exoplanets experience high stellar radiation and potential tidal heating, leading to equilibrium temperatures typically in excess of 2,000 K. Those with masses between a few and $\sim 15 M_{\oplus}$ are often called ‘hot super-Earths’.

Their high temperatures are sufficient to melt surface rocks, potentially leading to atmospheres composed of their vaporised surfaces (e.g Schaefer & Fegley 2009). Alternatively, if they do not have significant atmospheres, exospheres may be produced by sputtering of their surfaces by stellar winds (Mura et al. 2011). If the gas in these atmospheres or exospheres were to be observed, it would con-

strain the composition of the planet’s outer layer, providing valuable information for understanding their formation and evolution. In Chapter 2 of this thesis, we search for sodium and ionized calcium from the atmosphere or exosphere of the hot super-Earth 55 Cancri e.

1.4.1 Sputtering

The Solar System planet Mercury is the closest planet to the Sun, with an orbital semi-major axis of 0.387 au. The orbital distances of short period hot rocky exoplanets are $\gtrsim 25$ times smaller than that of Mercury, so it is intriguing to think of them as being extreme Mercury analogues.

Mercury does not have an atmosphere, but it does have a variable exosphere that is primarily produced by sputtering of its surface. Sputtering is the process of high energy photons or charged particles from the Sun impacting the surface and causing atoms to be ejected. The exosphere of Mercury has been well studied with spacecraft and various telescopes (e.g. Killen et al. 2007), which have robustly detected atoms and ions of elements such as sodium, calcium, potassium and magnesium. The Solar wind and radiation pressure can cause the exosphere to form into a tail, tens of planetary radii long.

Mura et al. (2011) investigated the sputtering induced exospheres of hot rocky exoplanets by simulating the exosphere of CoRoT-7 b and predicted it to be larger than Mercury’s and potentially detectable. Motivated by this, Guenther et al. (2011) searched for Na, Ca and Ca^+ in the hot super-Earth CoRoT-7 b but were only able to derive upper limits.

1.4.2 Possible mineral vapour atmospheres

As a result of their high temperatures, hot rocky exoplanets may also have atmospheres that are produced by the vaporisation of their molten surfaces. Schaefer & Fegley (2009) modelled the atmosphere of CoRoT-7 b, which has a mass of $8 M_{\oplus}$ and an equilibrium temperature between 1800 and 2600 K, and found that it is likely composed primarily of Na, O_2 , O, and SiO gas with lesser amounts of Na and K. They suggest that interactions with the stellar wind may cause large Na and K clouds to surround the planet (similar to those around Mercury and Io), which may potentially be detected with current observing capabilities. Miguel et al. (2011) carried out a similar but more extensive study, considering larger ranges of temperature (1000 – 3500 K), planetary mass ($1 - 10 M_{\oplus}$) and planet radius ($1 - 2.5 R_{\oplus}$). They found that the relative abundances of atmospheric species depend significantly on initial composition and temperature. Ito et al. (2015) performed a similar study and calculated atmospheric opacities over the wavelength region of $0.1 - 100 \mu\text{m}$. Their results suggest that a thermal inversion may occur due to UV

absorption by SiO. They estimate that strong SiO features may be detectable with the Spitzer Space Telescope and that Na and K may also be detectable with large ground based telescopes.

Based on the mean density of the hot super-Earth 55 Cancri e, it was thought to possibly have a hydrogen-helium or water atmosphere (e.g. Gillon et al. 2012). Recent non-detections of hydrogen (Ehrenreich et al. 2012), water (Esteves et al. 2017), and a potential detection of Ca^+ (Chapter 2) disfavour these ideas. However, hints of a HCN atmosphere have also been reported, that actually may support the hydrogen-rich interpretation (Tsiaras et al. 2016).

55 Cancri e is a promising target for detailed atmospheric characterisation with stable, high resolution spectrographs because its host star ($V = 5.95$) is 200 times brighter than CoRoT-7, which only yielded non-detections (Guenther et al. 2011). 55 Cancri e is therefore the subject of Chapter 2 of this thesis.

1.5 Characterisation with spectroscopy

Spectroscopy can constrain the composition of exoplanet atmospheres and exospheres because atoms and molecules absorb and emit light at unique wavelengths that correspond to transitions between quantised energy levels. Spectrographs disperse light and enable the observed flux as a function of wavelength to be measured. The resolving power, R , of a spectrograph determines the smallest difference in wavelength that it can distinguish, $\Delta\lambda$, for a given wavelength λ and is given by

$$R = \frac{\lambda}{\Delta\lambda}. \quad (1.4)$$

The strength of spectral features in an atmosphere generally depend on its scale height, H , which is the vertical distance over which its pressure decreases by a factor of $1/e$, and is given by

$$H = \frac{kT}{\mu_{atm}g'} \quad (1.5)$$

where k is the Boltzmann constant, T is the temperature of the atmosphere, μ_{atm} is the mean molecular weight of the atmosphere and g' is the acceleration due to the planet's gravity (Kaltenegger 2011). This shows that larger scale heights occur for larger temperatures and smaller atmospheric mean molecular weights and gravities.

During transit, star light passes through an annulus of atmosphere around the planet, where it can be absorbed by atmospheric atomic or molecular species.

The level of absorption from such features can be estimated as

$$\delta F_{tr} = \frac{(R_p + nH)^2 - R_p^2}{R_s^2} \quad (1.6)$$

where n is the thickness of the atmospheric annulus in scale heights and is typically 5 – 10. Substituting in typical values gives $\delta F_{tr} = 0.1\%$.

Spectroscopic observations of an exoplanet’s atmosphere are adversely affected by the spectral lines of its host star, which are orders of magnitude stronger. If the observations are carried out from the Earth’s surface, the exoplanet’s spectral lines will also be dominated by telluric (or Earth-atmosphere) absorption lines from molecules such as oxygen and water.

However, these issues can be mitigated if the observations are made at very high spectral resolution ($R \sim 100,000$) because this allows the Doppler shift caused by the exoplanet’s orbital motion to be resolved, providing a way to separate the planet’s spectral lines from those of its host star and the Earth’s atmosphere. This is demonstrated in Fig. 1.2, which shows how the spectral lines (at $R = 100,000$) of a toy model of carbon monoxide in the atmosphere of a transiting hot-Jupiter are Doppler shifted by its orbital motion. It also shows telluric lines, which remain at a constant wavelength over time. It does not show stellar lines because there are no stellar lines in this wavelength range, but if there were, they would appear similar to the telluric lines. During transit, at around 0 orbital phase, the planet’s spectral lines trace a diagonal line as they are blueshifted, then redshifted. The planet’s spectral lines are not visible at the secondary eclipse (phase 0.5) because the planet is behind its host star at that time.

Slit spectrographs, such as those used for this thesis, achieve high spectral resolutions by using narrow entrance slits that reject some star light. Additionally, at high spectral resolutions, the light is more dispersed, which reduces the number of photons landing on a given pixel on the CCD. Therefore, bright sources or long exposure times are needed to reach high signal to noise ratios.

55 Cancri e is one of the few currently known transiting hot super-Earths that orbits a star that is bright enough to be characterised with high-resolution spectroscopy. However, the recently launched Transiting Exoplanet Survey Satellite (TESS) (Ricker et al. 2016) is expected to find several hot super-Earths and disintegrating rocky exoplanets around brighter stars (Barclay et al. 2018).

1.6 Disintegrating rocky exoplanets

Small rocky exoplanets with temperatures on the order of 2,000 K can actively disintegrate and produce ‘comet-like’ dust tails. Since the dust originates from the

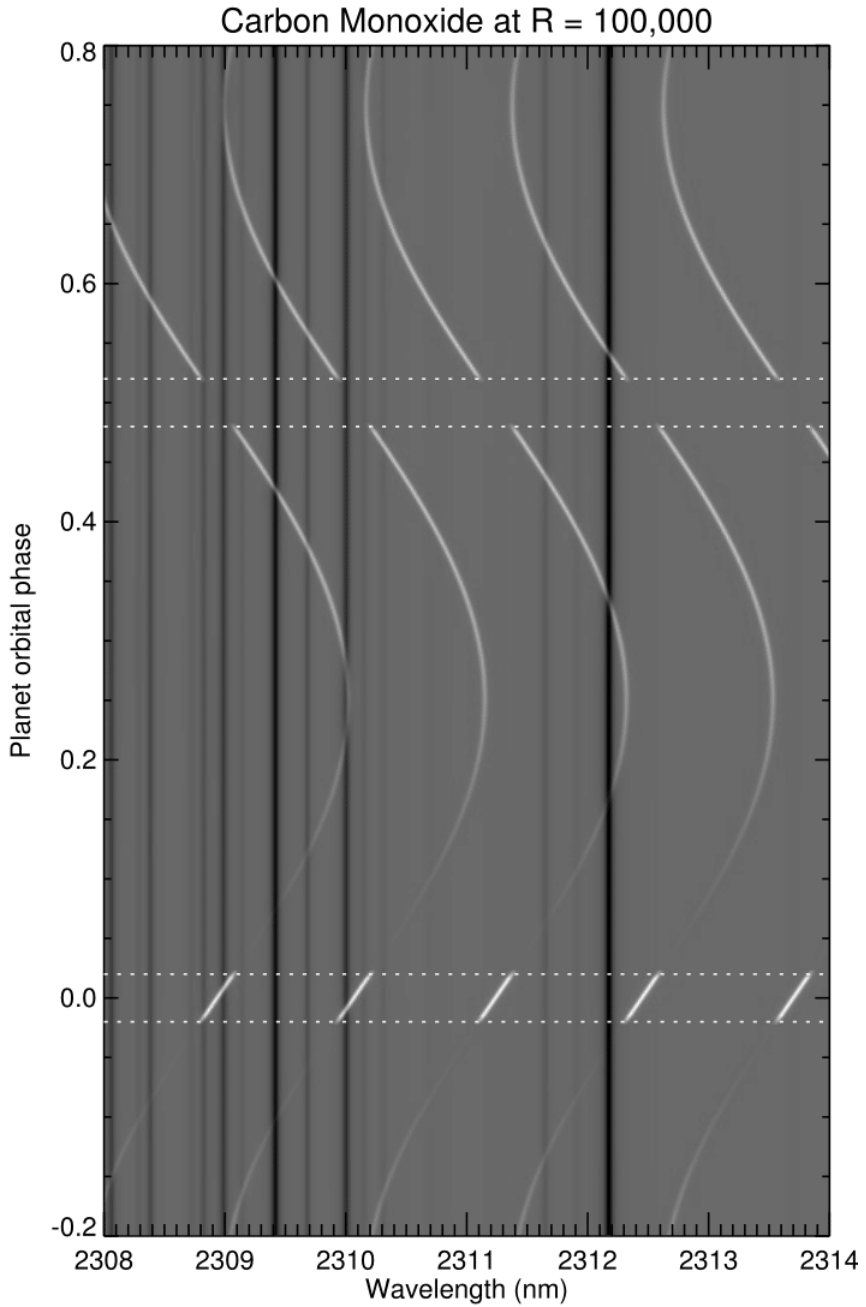


Figure 1.2: A toy model of the spectrum (at $R = 100,000$) of carbon monoxide in the atmosphere of a transiting hot-Jupiter, as a function of orbital phase (vertical axis). Image credit: Matteo Brogi.

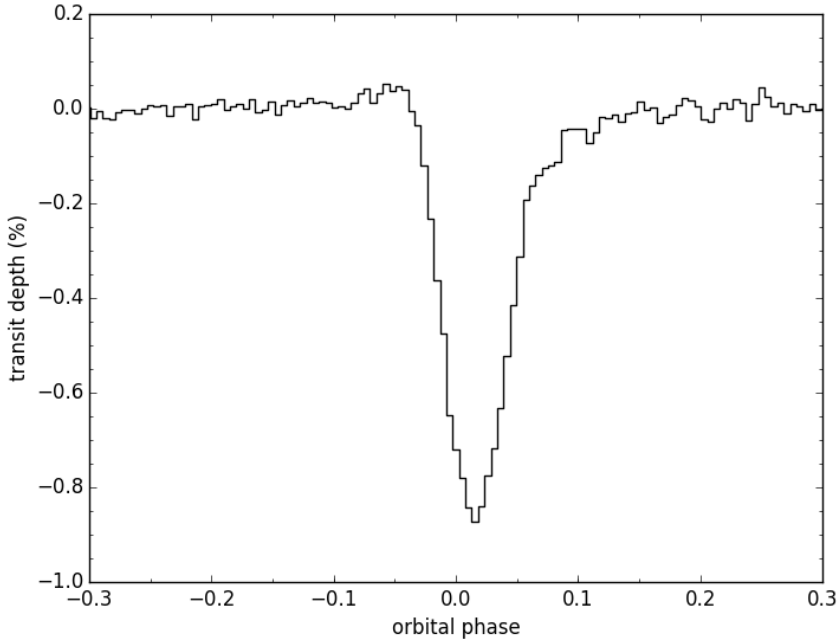


Figure 1.3: The Kepler average long cadence light curve of Kepler-1520 b, produced by the analysis of van Werkhoven et al. (2014).

surface of the planet, these objects offer an unparalleled opportunity to observationally constrain the surface composition of the planet.

To date, three such planets around main-sequence stars and one around a white dwarf have been discovered from Kepler light curves: Kepler-1520 b (also known as KIC 12557548 b) (Rappaport et al. 2012), KOI-2700 b (Rappaport et al. 2014), K2-22 b (Sanchis-Ojeda et al. 2015) and WD 1145+017 (Vanderburg et al. 2015). Their transit light curves are asymmetrical and exhibit dust forward scattering features. They also exhibit transit depths that vary from approximately zero to 1.4%. This variability suggests that the mass-loss rate from the planet also varies over orbital timescales. The average transit light curve of Kepler-1520 b (the first of these planets to be discovered) is shown in Fig. 1.3, where its forward scattering feature at ingress and extended egress are apparent.

1.6.1 Mass-loss mechanism

The leading idea for the mechanism responsible for causing the mass-loss from disintegrating rocky exoplanets is a thermal wind that is launched from the ap-

proximately 2,000 K surface (Perez-Becker & Chiang 2013). As the wind expands and cools, dust grains condense out of a fraction of the gas and are dragged away from the planet by the remaining escaping gas.

This mass-loss could be self-regulating because:

1. An episode of high mass-loss would result in more dust in the planet's atmosphere, which would absorb more stellar flux, reducing the flux received by the surface.
2. The reduced flux will decrease the surface vapour pressure, and hence reduce the outward flow of dust being transported into the upper atmosphere, resulting in a low mass-loss episode.
3. This low mass-loss episode will lead to a clear atmosphere with less dust in the atmosphere to absorb the stellar flux, increasing the vapour pressure and leading back to a period of high mass-loss (Step 1).

This cycle could produce some of the observed variability in transit depth. However, it has also been qualitatively suggested that it may be punctuated with unpredictable outbursts from volcanoes or geysers (Rappaport et al. 2012; Perez-Becker & Chiang 2013), potentially allowing the planet's geophysics to be probed.

Perez-Becker & Chiang (2013) argue that the thermal wind has typical velocities of approximately 1 km s^{-1} . This is comparable to the minimum particle ejection velocity of 1.2 km s^{-1} that was derived in Chapter 3 of this thesis. We search for gas that may have been lost in the thermal wind of K2-22 b (or produced by the sublimation of dust in its tail) in Chapter 5 of this thesis.

1.6.2 Dust particle dynamics

The composition and size of dust particles in the tails of disintegrating hot rocky exoplanets can be observationally constrained (e.g. van Lieshout et al. 2016). Since they originate from the planet, their composition must be related to that of the surface of the planet. However, interpreting how the compositions are connected requires an understanding of the evolution of the dust tails. Their length and morphology are determined by the dynamics of the individual particles in the tail, which is relatively well understood for simple cases.

Their motion is mainly governed by the balance of the stellar radiation pressure force with the stellar gravitational force, which both decrease with the inverse square of the distance from the star (e.g. Rappaport et al. 2012; van Lieshout et al. 2016). This results in the particle effectively experiencing a reduced gravitational field, g_{eff} , given by

$$g_{\text{eff}} = \frac{GM_s(1 - \beta)}{r^2} \quad (1.7)$$

where G is the universal gravitational constant, M_s is the mass of the star, r is the radial distance from the star and β is the ratio of stellar radiation pressure force to stellar gravitational force

$$\beta(s) = \frac{F_{rad}}{F_{grav}} \quad (1.8)$$

where β depends only on the particle size, s , for a given composition. It can be seen that the effective gravity that the particles experience, g_{eff} , is the gravity that the particles would experience if the host star's mass were reduced by a factor of $(1 - \beta)$.

In the ideal case where a particle's ejection velocity from the planet is comparable to the planet's escape velocity, it will go into an elliptical Keplerian orbit with periastron at the point where the particle was released (Rappaport et al. 2014).

For such an orbit, the eccentricity can be calculated as

$$e = \frac{\beta}{1 - \beta} \quad (1.9)$$

the dust particle's orbital semi-major axis, a_d , relative to that of the planet, a_p , is

$$a_d = a_p \frac{1 - \beta}{1 - 2\beta} \quad (1.10)$$

and the dust particle's orbital angular frequency, ω_d , relative to that of the planet, ω_p , is

$$\omega_d = \omega_p \frac{(1 - 2\beta)^{\frac{3}{2}}}{1 - \beta}. \quad (1.11)$$

These equations indicate that a dust particle will be on a bound orbit if $\beta < 0.5$ because if $\beta = 0.5$, $e = 1$, a_d/a_p goes to infinity and $\omega_d/\omega_p = 0$. With increasing β (while $\beta < 0.5$), the dust particle's eccentricity and orbital semi-major axis increase, while its orbital angular velocity decreases. These all result in the dust particle drifting away from the planet.

However, the stellar radiation causes the dust particles to sublimate, which changes their size, s , and corresponding value of $\beta(s)$. Therefore, these orbital elements evolve over the lifetimes of the dust particles.

For spherical dust grains, the value of β is given by

$$\beta(s) = \frac{3}{16\pi cG} \frac{L_s}{M_s} \frac{\bar{Q}_{pr}(s)}{\rho_d s} \quad (1.12)$$

where c is the speed of light, G is the universal gravitational constant, L_s is the luminosity of the host star, M_s is the mass of the host star, ρ_d is the density of

the dust, s is the dust grain's radius and $\bar{Q}_{pr}(s)$ is the radiation pressure efficiency averaged over the stellar spectrum. $\bar{Q}_{pr}(s)$ depends on the dust's refractive index and can be calculated from Mie theory (Mie 1908; Burns et al. 1979).

While $\beta(s)$ varies depending on the dust composition, the profile of β as a function of s , for all compositions, generally have the same shape. Their peak values for $\beta(s)$ generally occur when the grains have sizes, s_p , that are similar to the host star's peak wavelength (Burns et al. 1979). For the spectrum of Kepler-1520, this results in $\beta(s)$ being largest for particles of radii approximately 0.1 – 0.5 μm (van Lieshout et al. 2014).

Going to larger grain sizes, Mie theory converges to the limit of geometric optics, where $\bar{Q}_{pr}(s)$ essentially becomes a constant value. This results in $\beta(s)$ linearly decreasing with increasing particle size (i.e. $\beta(s) \propto s^{-1}$). For particle sizes less than s_p , $\beta(s)$ decreases because the particles are too small to significantly absorb or scatter photons at the peak wavelength of the host star's spectrum (Burns et al. 1979). Therefore, for typical initial particle radii of approximately 1 μm , sublimation will cause $\beta(s)$ to increase then decrease.

The orbital dynamics of the dust particles is not as well understood in more complicated situations like when the tail is optically thick, providing significant self-shielding. This is investigated in Chapter 4 of this thesis.

1.7 This thesis

This thesis deals with observational and numerical simulation techniques to gain insight into hot rocky exoplanets and move towards determining observational constraints on the geophysical properties of these enigmatic worlds.

1.7.1 Chapter 2

We analysed high dispersion ($R \sim 100,000$) spectra of five transits of the hot rocky super-Earth, 55 Cancri e, to search for Na and Ca^+ in its atmosphere or exosphere. One transit was observed with UVES/VLT, two were observed with HARPS/ESO 3.6 m and two were observed with HARPS-N/TNG. We used the fact that the planet's radial velocity changed from -57 to $+57$ km s^{-1} during transit to separate its lines from the stellar spectral lines and used a principal component analysis (PCA) to remove the variable telluric lines. By combining all datasets, we detect a signal potentially associated with sodium in the planet's exosphere to a significance of 3σ . Combining the four HARPS/HARPS-N transits that include the Ca^+ H and K lines, we find a potential signal of Ca^+ to a significance of 4.1σ . However, this signal originates entirely from a single data set, where it has a significance of 4.9σ . We estimate the p-values associated with these signals to be too high to al-

low us to claim definitive detections so we only report them as potential detections worthy of follow-up observations.

1.7.2 Chapter 3

We simulated the dust tail of the disintegrating rocky exoplanet Kepler-1520 b with a dust particle dynamics code and the radiative transfer code, MCMax3D. We found that the transit depth was wavelength independent for optically thick tails. Therefore, a temporal variation in the optical depth of the tail can potentially explain why only some multi-wavelength observations have detected a wavelength dependence in transit depth. We also derived a minimum particle ejection velocity of 1.2 km s^{-1} and found that we required mass-loss rates of $7 - 80 M_{\oplus} \text{ Gyr}^{-1}$ to produce the observed transit depths. However, these mass-loss rates are higher than those derived with other models and may result in planet lifetimes that are inconsistent with the observed sample of planets.

1.7.3 Chapter 4

We extended the model that was developed for Chapter 3 so that it approximated self-shielding within the tail, to investigate the morphology of optically thick tails. The self-shielding reduced the radiation flux received by shielded particles, which reduced the radiation pressure they experienced and their sublimation rates. To reproduce the average transit depth of Kepler-1520 b with the self-shielding model, we required mass-loss rates of $3 - 3.9 M_{\oplus} \text{ Gyr}^{-1}$. However, we also found that unless the intrinsic sublimation rate was assumed to be very high, it was easy for shielded particles to survive for more than one orbit, violating the lack of correlation between consecutive transit depths found by van Werkhoven et al. (2014).

1.7.4 Chapter 5

We observed four transits of the disintegrating rocky exoplanet K2-22 b with X-shooter/VLT to obtain intermediate resolution spectra to search for gas that was directly lost from the planet or produced by the sublimation of dust particles in the tail. We focussed on the sodium D lines and the ionized calcium near-infrared triplet as these produce the strongest absorption lines in comets, despite their low abundances. We did not detect the species and by injecting artificial signals we derived 5σ upper-limits with absorption relative to the stellar spectrum from sodium and ionized calcium of 9% and 1.6%, respectively. These limits indicate low gas-loss limits compared to the estimated average dust mass-loss derived for this system. We suggest that the probed gases are probably accelerated by the stellar wind and radiation pressure, leading to very broad and difficult to detect blueshifted sig-

nals with widths of hundreds of km s^{-1} . We searched for such signals in our data but did not detect them.

1.8 Future outlook

The main limitation on studying hot rocky exoplanets is achieving high signal-to-noise ratios (SNRs) in transit light curves and transmission spectroscopy. This is particularly relevant for disintegrating rocky exoplanets because their individual transit light curves are not of a sufficiently high SNR to reveal features such as forward scattering peaks that can be fit with models, so they are averaged to increase SNR (van Werkhoven et al. 2014). However, their transit light curves are known to be highly variable, so the average light curve, and the physical properties derived from it, may not accurately reflect the individual cases.

One way that higher SNRs can be achieved is by using large telescopes such as the upcoming Extremely Large Telescope (ELT) and Thirty Meter Telescope (TMT), which are planned to start operating in 2024² and 2027³, respectively. However, another potential avenue is opened by TESS, which is expected to discover several hot, potentially disintegrating, rocky exoplanets orbiting bright stars (Barclay et al. 2018) that can be characterised in detail with current facilities.

Once we are able to observe high SNR transit light curves of disintegrating rocky exoplanets in several wavelength bands, more accurate dust-tail models that include higher order effects can be quantitatively compared to the observations. These additional higher order effects could potentially include modelling the effect of gas-pressure on the dust-particle dynamics and coupling the dust-tail dynamics models to physically inspired models of mass-loss from the planet, so that the properties of the mass-loss mechanism can be constrained.

For hot rocky super-Earths, high SNR transmission spectra will allow robust detections of chemical species in their atmospheres, that will likely be strongly linked to their rocky surface compositions (e.g. Schaefer & Fegley 2009). Going beyond this, robust detections of several species will make it possible to meaningfully constrain their formation and migration histories by comparing to models that relate a planet's current atmospheric abundances to the conditions in its protoplanetary disk during its formation (e.g. Madhusudhan et al. 2016; Cridland et al. 2016).

²<http://iopscience.iop.org/article/10.1088/2058-7058/29/8/21>

³<https://www.tmt.org/page/timeline?category=Observatory+Construction>

Bibliography

- Barclay, T., Pepper, J., & Quintana, E. V. 2018, ArXiv e-prints, arXiv:1804.05050
- Borucki, W. J., Koch, D., Basri, G., et al. 2010, *Science*, 327, 977
- Boss, A. P. 1997, *Science*, 276, 1836
- Burns, J. A., Lamy, P. L., & Soter, S. 1979, *Icarus*, 40, 1
- Chambers, J. E. 2009, *Annual Review of Earth and Planetary Sciences*, 37, 321
- Chatterjee, S., Ford, E. B., Matsumura, S., & Rasio, F. A. 2008, *ApJ*, 686, 580
- Cridland, A. J., Pudritz, R. E., & Alessi, M. 2016, *MNRAS*, 461, 3274
- Dawson, R. I. & Johnson, J. A. 2018, ArXiv e-prints, arXiv:1801.06117
- Ehrenreich, D., Bourrier, V., Bonfils, X., et al. 2012, *A&A*, 547, A18
- Esteves, L. J., de Mooij, E. J. W., Jayawardhana, R., Watson, C., & de Kok, R. 2017, *AJ*, 153, 268
- Gillon, M., Demory, B.-O., Benneke, B., et al. 2012, *A&A*, 539, A28
- Gillon, M., Triaud, A. H. M. J., Demory, B.-O., et al. 2017, *Nature*, 542, 456
- Guenther, E. W., Cabrera, J., Erikson, A., et al. 2011, *A&A*, 525, A24
- Howell, S. B., Sobek, C., Haas, M., et al. 2014, *PASP*, 126, 398
- Ito, Y., Ikoma, M., Kawahara, H., et al. 2015, *ApJ*, 801, 144
- Jackson, B., Adams, E., Heller, R., & Endl, M. 2018, ArXiv e-prints
- Kaltenegger, L. 2011, *Scale Height*, ed. M. Gargaud, R. Amils, J. C. Quintanilla, H. J. J. Cleaves, W. M. Irvine, D. L. Pinti, & M. Viso (Berlin, Heidelberg: Springer Berlin Heidelberg), 1492–1492
- Killen, R., Cremonese, G., Lammer, H., et al. 2007, *Space Sci. Rev.*, 132, 433
- Koch, D. G., Borucki, W. J., Basri, G., et al. 2010, *ApJ*, 713, L79
- Lin, D. N. C., Bodenheimer, P., & Richardson, D. C. 1996, *Nature*, 380, 606
- Lin, D. N. C., Woosley, S. E., & Bodenheimer, P. H. 1991, *Nature*, 353, 827
- Madhusudhan, N., Agúndez, M., Moses, J. I., & Hu, Y. 2016, *Space Science Reviews*, 205, 285
- Mie, G. 1908, *Annalen der Physik*, 330, 377

- Miguel, Y., Kaltenegger, L., Fegley, B., & Schaefer, L. 2011, *ApJ*, 742, L19
- Mura, A., Wurz, P., Schneider, J., et al. 2011, *Icarus*, 211, 1
- Perez-Becker, D. & Chiang, E. 2013, *MNRAS*, 433, 2294
- Pollack, J. B., Hubickyj, O., Bodenheimer, P., et al. 1996, *Icarus*, 124, 62
- Rappaport, S., Barclay, T., DeVore, J., et al. 2014, *ApJ*, 784, 40
- Rappaport, S., Levine, A., Chiang, E., et al. 2012, *ApJ*, 752, 1
- Ricker, G. R., Vanderspek, R., Winn, J., et al. 2016, in *Space Telescopes and Instrumentation 2016: Optical, Infrared, and Millimeter Wave*, Vol. 9904, 99042B
- Sanchis-Ojeda, R., Rappaport, S., Pallè, E., et al. 2015, *ApJ*, 812, 112
- Schaefer, L. & Fegley, B. 2009, *ApJ*, 703, L113
- Schlichting, H. E. 2014, *ApJ*, 795, L15
- Schlichting, H. E. 2018, *ArXiv e-prints*
- Tsiaras, A., Rocchetto, M., Waldmann, I. P., et al. 2016, *ApJ*, 820, 99
- van Lieshout, R., Min, M., & Dominik, C. 2014, *A&A*, 572, A76
- van Lieshout, R., Min, M., Dominik, C., et al. 2016, *A&A*, 596, A32
- van Werkhoven, T. I. M., Brogi, M., Snellen, I. A. G., & Keller, C. U. 2014, *A&A*, 561, A3
- Vanderburg, A., Johnson, J. A., Rappaport, S., et al. 2015, *Nature*, 526, 546
- Ward, W. R. 1997, *Icarus*, 126, 261
- Wolszczan, A. & Frail, D. A. 1992, *Nature*, 355, 145
- Wright, J. T. 2017, *Radial Velocities as an Exoplanet Discovery Method*, ed. H. J. Deeg & J. A. Belmonte (Springer Living Reference Work), 4

2 | Search for an exosphere in sodium and calcium in the transmission spectrum of exoplanet 55 Cancri e

Based on:

Ridden-Harper, A. R.; Snellen, I. A. G.; Keller, C. U.; de Kok, R. J.; Di Gloria, E.; Hoeijmakers, H. J.; Brogi, M.; Fridlund, M.; Vermeersen, B. L. A.; van Westrenen, W., A&A 593, A129 (2016)

Context. The atmospheric and surface characterization of rocky planets is a key goal of exoplanet science. Unfortunately, the measurements required for this are generally out of reach of present-day instrumentation. However, the planet Mercury in our own solar system exhibits a large exosphere composed of atomic species that have been ejected from the planetary surface by the process of sputtering. Since the hottest rocky exoplanets known so far are more than an order of magnitude closer to their parent star than Mercury is to the Sun, the sputtering process and the resulting exospheres could be orders of magnitude larger and potentially detectable using transmission spectroscopy, indirectly probing their surface compositions.

Aims. The aim of this work is to search for an absorption signal from exospheric sodium (Na) and singly ionized calcium (Ca^+) in the optical transmission spectrum of the hot rocky super-Earth 55 Cancri e. Although the current best-fitting models to the planet mass and radius require a possible atmospheric component, uncertainties in the radius exist, making it possible that 55 Cancri e could be a hot rocky planet without an atmosphere.

Methods. High resolution ($R \sim 110000$) time-series spectra of five transits of 55 Cancri e, obtained with three different telescopes (UVES/VLT, HARPS/ESO 3.6m & HARPS-N/TNG) were analysed. Targeting the sodium D lines and the calcium H and K lines, the potential planet exospheric signal was filtered out from the much stronger stellar and telluric signals, making use of the change of the radial component of the orbital velocity of the planet over the transit from -57 to $+57 \text{ km s}^{-1}$.

Results. Combining all five transit data sets, we detect a signal potentially associated with sodium in the planet exosphere at a statistical significance level of 3σ . Combining the four HARPS transits that cover the calcium H and K lines, we also find a potential signal from ionized calcium (4.1σ). Interestingly, this latter signal originates from just one of the transit measurements - with a 4.9σ detection at this epoch. Unfortunately, due to the

low significance of the measured sodium signal and the potentially variable Ca^+ signal, we estimate the p-values of these signals to be too high (corresponding to $<4\sigma$) to claim unambiguous exospheric detections. By comparing the observed signals with artificial signals injected early in the analysis, the absorption by Na and Ca^+ are estimated to be at a level of $\sim 2.3 \times 10^{-3}$ and $\sim 7.0 \times 10^{-2}$ respectively, relative to the stellar spectrum.

Conclusions. If confirmed, the 3σ signal would correspond to an optically thick sodium exosphere with a radius of $5 R_{\oplus}$, which is comparable to the Roche lobe radius of the planet. The 4.9σ detection of Ca^+ in a single HARPS data set would correspond to an optically thick Ca^+ exosphere approximately five times larger than the Roche lobe radius. If this were a real detection, it would imply that the exosphere exhibits extreme variability. Although no formal detection has been made, we advocate that probing the exospheres of hot super-Earths in this way has great potential, also knowing that Mercury's exosphere varies significantly over time. It may be a fast route towards the first characterization of the surface properties of this enigmatic class of planets.

2.1 Introduction

Transit and radial velocity surveys have revealed a new class of rocky planets orbiting their parent stars at very short distances (0.014 - 0.017 au¹). Their evolutionary history is unknown. They may be rocky planets formed at significantly larger distances that subsequently migrated inwards, or could originally be gas-rich planets which lost their gaseous envelopes during migration through tidal heating and/or direct stellar irradiation (Raymond et al. 2008). Insights into the composition of these hot rocky planets would help to distinguish between the different scenarios. Although the first secondary eclipse measurements have been presented in the literature (Demory et al. 2012), showing them to be indeed very hot, with observed surface or atmospheric temperatures of 1300 - 3000K, detailed observations that could reveal atmospheric or surface compositions are beyond the reach of current instrumentation.

One physical process that could reveal information of a planet's surface composition, potentially also with current instruments, is that of sputtering. Atomic species are ejected from the planet surface by the intense stellar wind of charged particles, creating an extended exosphere around the planet. This process is well known from planet Mercury in our own solar system. It has an exosphere composed of atomic species including sodium (Na), calcium (Ca) and magnesium (Mg), which are thought to be the results of sputtering, thermal vaporisation, photon-stimulated desorption, and meteoroid impact vaporisation. Since the discovery of an emission spectrum of sodium in the exosphere of Mercury by Potter & Morgan (1985), it has been subsequently detected many times (see Killen et al. 2007, for a review) in emission, and less commonly in absorption during the transit of Mercury in front of the Sun (Potter et al. 2013). These decades of observations have revealed that sodium in the exosphere of Mercury shows a great deal of spatial and temporal variability. Rapid variations at a 50% level on timescales of a day in the ion-sputtering component of the sodium in Mercury's exosphere due to variability in the magnetosphere have been observed, as well as latitudinal and/or longitudinal variations (Potter & Morgan 1990; Killen et al. 2007). In addition, long-term variations on timescales of months to years in photon-stimulated desorption (Lammer et al. 2003; Killen et al. 2007) and radiation pressure acceleration (Smyth & Marconi 1995; Killen et al. 2007) have been observed, as well as variations in meteoritic vaporisation (Morgan et al. 1988; Killen et al. 2007).

Mura et al. (2011) argued for the first time that such exospheres resulting from the sputtering process may be observable for hot rocky exoplanets. Their simulations for CoRoT-7b suggest that it may have a high escape rate of species such as

¹0.014 is the semi-major axis of GJ 1214b, identified from exoplanets.org as the shortest semi-major axis with filter MINSI[mjupiter] < 10M_⊕ and 0.017 comes from the definition of an ultra-short period planet (USP) from Demory et al. (2015) of P < 0.75 days.

Na, Ca⁺, and Mg⁺ which likely form a tail tens of planetary radii long. Guenther et al. (2011) observed a transit of CoRoT-7b with the UVES instrument on the VLT with a focus on Na, Ca, and Ca⁺. While Guenther et al. (2011) express their derived upper limits in units of stellar luminosity ($2-6 \times 10^{-6} L_*$), these limits appear to correspond to an absorption level on the order of approximately 3×10^{-3} smeared out over a 55 km s^{-1} velocity bin due to the change in the radial component of the orbital velocity of the planet during their long exposures. In this chapter we target the exoplanet 55 Cancri e, whose host star has an apparent magnitude of $V = 5.95$, 200 times brighter than CoRoT-7.

In addition, Schaefer & Fegley (2009) argue that a tidally locked hot rocky super-Earth could have a magma ocean that releases vapours to produce a silicate based atmosphere. Their models show that Na is likely the most abundant constituent of such an atmosphere, which they believe could form a large cloud of Na through interaction with the stellar wind.

Considerable progress regarding the detection and study of exospheres of hot gas giant exoplanets has already been made. Hydrogen exospheres extending beyond the Roche lobe have been repeatedly detected around HD 209458b (Vidal-Madjar et al. 2003, 2004) and HD 189733b (Lecavelier des Etangs et al. 2010), where the hydrogen signal from HD 189733b has been claimed to show temporal variation (Lecavelier des Etangs et al. 2012). Heavier atoms and ions have been detected in the exosphere of HD 209458b, including C⁺ (Vidal-Madjar et al. 2004; Linsky et al. 2010) and, more tentatively, O (Vidal-Madjar et al. 2004), Mg (Vidal-Madjar et al. 2013) and Si²⁺ (Linsky et al. 2010). Exospheric studies have recently also been extended to smaller planets with the detection of hydrogen around the warm Neptune GJ 436b (Ehrenreich et al. 2015). We note that no hydrogen exosphere was detected around 55 Cancri e (Ehrenreich et al. 2012), which is the object of this study.

The hot, rocky super-Earth type planet, 55 Cancri e (or ρ^1 Cancri e, 55 Cnc e) orbits a bright ($V=5.95$) $0.905 M_\odot$ star. It has a very short orbital period of 17.7 hours (see Table 2.1 for uncertainties), a radius of $2.173 R_\oplus$ (Gillon et al. 2012), a mass of $8.09 M_\oplus$, and an inferred average density of 5.51 g cm^{-3} (Nelson et al. 2014). Transits of 55 Cnc e have been detected with broadband photometry from space in the visible (Winn et al. 2011) and infra-red (Demory et al. 2011), and recently also from the ground (de Mooij et al. 2014).

There is significant debate in the literature about the chemical composition and interior structure of 55 Cnc e. Using the internal structure model by Valencia et al. (2006, 2010), Gillon et al. (2012) argue that 55 Cnc e is likely a rocky, oxygen-rich planet composed of silicates with a gaseous envelope consisting of either a mixture of hydrogen and helium of approximately 0.1% by mass or a water atmosphere of approximately 20% by mass. However, because such a low

mass H-He atmosphere would escape over a timescale of millions of years, while a water-vapour atmosphere could survive over billions of years, the water-vapour atmosphere interpretation is favoured, where the water-vapour is in a super-critical form due to its high temperature. Furthermore, Ehrenreich et al. (2012) found that 55 Cnc e lacks a H exosphere which could be the result of complete H loss from the atmosphere in the past. In contrast, Madhusudhan et al. (2012) claim that if 55 Cnc e were to be a carbon-rich planet, a different structure is possible where Fe, C (in the form of graphite and diamond), SiC, and silicates of a wide range of mass fractions could explain its density without the need for a gaseous envelope. While the C/O ratio of 55 Cnc was previously thought to be >1 , a subsequent analysis by Teske et al. (2013) found that it more likely has a C/O ratio of 0.8. This value is lower than the value adopted by Madhusudhan et al. (2012) of 1.12 ± 0.19 ; however, it still corresponds to the predicted minimum value of 0.8 necessary for the formation of a carbon-rich condensate under the assumption of equilibrium (Larimer 1975).

Furthermore, Demory et al. (2015) report a 4σ detection of variability in the day-side thermal emission of 55 Cnc e, with the emissions varying by a factor of 3.7 between 2012 to 2013. They also tentatively suggest variations in the transit depth and calculate the planetary radii to range from $1.75 \pm 0.13 R_{\oplus}$ to $2.25 \pm 0.17 R_{\oplus}$ with a mean value of $1.92 \pm 0.08 R_{\oplus}$, which is approximately 2σ smaller than the value published by Gillon et al. (2012) of $2.17 \pm 0.10 R_{\oplus}$ based on Spitzer+MOST data. We believe that this smaller radius implies that the need for a significant atmosphere to explain the planet's radius is significantly reduced.

If 55 Cnc e does not have an atmosphere, its surface would be directly exposed to stellar radiation, making it analogous to Mercury. It is likely that the processes which produce the exosphere of Mercury would be much more pronounced on 55 Cnc e because it receives a bolometric flux from its host star that is approximately 500 times greater than Mercury receives from the Sun. This corresponds to an equilibrium temperature of 55 Cnc e of almost 2000 K. Demory et al. (2015) claim to have detected brightness temperatures which vary from 1300 K to 3000 K; however, the mechanism which causes this variability is not understood.

Demory et al. (2016) report the observation of a complete phase curve of 55 Cnc e in the $4.5\mu\text{m}$ channel of the Spitzer Space Telescope Infrared Array Camera which allowed them to construct a longitudinal thermal brightness map due to 55 Cnc e being tidally locked to its host star. This map revealed that 55 Cnc e has a strong day-night temperature contrast with temperatures of 2700 K and 1380 K on the day and night sides respectively. Furthermore, they found that the day side exhibits highly asymmetric thermal emissions, with a hot spot located 41 degrees east of the substellar point. These observations were interpreted as being either due to an atmosphere with heat recirculation confined to the day side only, or

Table 2.1: Properties of 55 Cancri e

Parameter	Value	Source
Stellar properties		
Distance (pc)	12.34 ± 0.11	van Leeuwen (2007)
Radius (R_{\odot})	0.943 ± 0.010	von Braun et al. (2011)
Luminosity (L_{\odot})	0.582 ± 0.014	von Braun et al. (2011)
T_{EFF} (K)	5196 ± 24	von Braun et al. (2011)
Mass (M_{\odot})	0.905 ± 0.015	von Braun et al. (2011)
$\log g$	4.45 ± 0.01	von Braun et al. (2011)
Radial velocity	27.58 ± 0.07	Nidever et al. (2002)
Planet properties		
Period (days)	0.7365449 ± 0.000005	Gillon et al. (2012)
Orb. radius (AU)	0.0154 ± 0.0001	*
Radius (R_{\oplus})	2.173 ± 0.098	Gillon et al. (2012)
Mass (M_{\oplus})	8.09 ± 0.26	Nelson et al. (2014)
Density (g cm^{-3})	$5.51 \pm_{1.00}^{1.32}$	Nelson et al. (2014)

*Calculated using Kepler's third law.

a planet without an atmosphere with low-viscosity magma flows on the surface. Atmospheric escape rate arguments indicate that it is unlikely that 55 Cnc e has a thick atmosphere, so the magma ocean interpretation is favoured.

In this chapter, we aim to search for an absorption signal from exospheric sodium (Na) and singly ionized calcium (Ca^+) in the optical transmission spectrum of the hot rocky super-Earth 55 Cnc e. This chapter is structured as follows. Section 2.2 describes the data and Section 2.3 explains the methods used in this analysis. Section 2.4 presents the results, and Section 2.5 discusses the interpretation of the results and concludes.

2.2 Observational data

High-dispersion spectral time series of five transits of 55 Cnc e taken with three different telescopes were used for our analysis. The five data sets each cover one transit including observations just before and after the transit. We observed one transit using the Ultraviolet and Visual Echelle Spectrograph (UVES) (Dekker

et al. 2000) installed on the Nasmyth B focus of the Very Large Telescope (VLT) at the Paranal Observatory. Furthermore, we retrieved additional data sets from observatory archives. Two of these were observed with the High Accuracy Radial Velocity Planet Searcher (HARPS) (Mayor et al. 2003) located at the ESO 3.6m Telescope at the La Silla Observatory, and two from its northern-hemisphere copy - HARPS-N (Cosentino et al. 2012) located at the 3.6m Telescopio Nazionale Galileo at the Roque de los Muchachos Observatory. An overview of all observations is shown in Table 2.4.

2.2.1 UVES data

138 UVES spectra were obtained of 55 Cnc. The transit timing, dates, exposure times, observational cadence and phase coverage are presented in Table 2.4. The observations were made using the red arm of UVES, utilizing grating CD#3 with a central wavelength of 580.0 nm, resulting in a wavelength range of 4726.5 – 6835.1 Å. A resolving power of $R \approx 110000$ was achieved using a slit width of 0.3'' and image slicer #3 to minimize the slit losses. Using no charge-coupled device (CCD) binning, the sampling is two pixels per spectral element (D’Odorico et al. 2000).

Unfortunately, cirrus clouds were present during our observations which considerably decreased the signal-to-noise ratio (S/N) in the spectra, ranging from S/N=180 during relatively good spells down to S/N=60 per pixel.

2.2.2 HARPS data

The HARPS data used for our analysis cover two transits and were originally taken for ESO programme 288.C-5010 (PI: A. Triaud) which was used by López-Morales et al. (2014) to investigate the Rossiter-McLaughlin effect in 55 Cnc e. We retrieved the pipeline-reduced data from the ESO Science Archive Facility².

HARPS has a resolving power of $R \approx 115000$ and a wavelength range of 3800 – 6910 Å. It is enclosed in a vacuum vessel, pressure and temperature controlled to a precision of ± 0.01 mbar and ± 0.01 K respectively, resulting in a wavelength precision of $\lesssim 0.5 \text{ m s}^{-1} \text{ night}^{-1}$ (Bonfils et al. 2013). It has two fibres which feed the spectrograph with light from the telescope and calibration lamp. The fibre aperture on the sky is 1''. The CCD has a pixel size of 15 μm and a sampling of 3.2 pixels per spectral element (Mayor et al. 2003). The transit timing, dates, exposure times, observational cadence, and phase coverage are presented in Table 2.4.

²<http://archive.eso.org/cms.html>

2.2.3 HARPS-N data

The HARPS-N observations also cover two transits, and were originally taken in TNG Observing programme CAT13B_33 (PI: F. Rodler), also to investigate the Rossiter McLaughlin effect by the same team (López-Morales et al. 2014). The pipeline-reduced data was retrieved by us from the TNG data archive³.

HARPS-N is a copy of HARPS so its properties are all identical or very similar to HARPS at ESO. It has a slightly different wavelength range of 3830 – 6900 Å and a sampling of 3.3 pixels per FWHM. It also has a greater temperature stability than HARPS of 0.001 K, giving a short-term precision of 0.3 m s⁻¹ and a global long-term precision of better than 0.6 m s⁻¹⁴. The fibre aperture on sky and spectral resolution are identical to those of HARPS. The transit timing, dates, exposure times, observational cadence, and phase coverage are presented in Table 2.4.

We note that an additional five publicly available data sets⁵ of the transit of 55 Cnc e were obtained with HARPS-N by Bourrier et al. (2014) to investigate the Rossiter-McLaughlin effect. The individual spectra of these data sets have exposure times of 360 seconds, which is twice the average exposure time of the data used in this study. Therefore, we chose to not use these data sets because due to the very rapid change in the radial component of the orbital velocity of the planet (114 km s⁻¹ over the transit), any planet signature would be smeared out by ten pixels, significantly decreasing its peak.

2.3 Data analysis

In our analysis we concentrate on the H and K lines of ionized calcium (at 3968.47 Å and 3933.66 Å respectively) and the two sodium D lines (5889.95 Å and 5895.92 Å). While the sodium lines are covered by all data sets, the ionized calcium lines are only present in the HARPS and HARPS-N data and not in the UVES data.

2.3.1 Processing of UVES spectra

The observed spectra are dominated by stellar and possible telluric absorption lines which are orders of magnitude stronger than the expected planet features. Since the stellar and telluric absorption lines are quasi-fixed in wavelength (the stellar lines change in radial velocity by approximately 1.4 m s⁻¹ during the four hour observations (McArthur et al. 2004)) and the radial component of the orbital velocity of the planet changes by tens of km s⁻¹ during the transit, the change in the Doppler shift of the planet lines can be used to separate the planet signal from that

³<http://ia2.oats.inaf.it/archives/tng>

⁴<http://www.tng.iac.es/instruments/harps/>

⁵TNG programme IDs: OPT12B_13, OPT13B_30, OPT14A_34

of the star and the Earth's atmosphere. The procedure we used to carry out this processing is very similar to that used in previous work (eg. Snellen et al. 2010; Hoeijmakers et al. 2015) and the individual steps are summarised below.

1. Extraction of wavelength calibrated 1D spectra. The UVES data were reduced using the standard ESO UVES reduction pipeline (Ballester et al. 2000) which was executed with Gasgano⁶ and EsoRex⁷. The pipeline produced a one-dimensional wavelength calibrated spectrum for each order for each exposure.
2. Normalization of the spectra to a common flux level. Variation in instrumental throughput (for example, due to slit losses) and atmospheric absorption result in the spectra having different baseline fluxes. To normalise the individual spectra to a common flux level, every spectrum was divided through its median value. The median value of a spectrum was used to minimize the influence of cosmic ray hits. This scaling can be performed because this analysis does not depend on the absolute flux, but instead only on the relative changes in flux as a function of wavelength.
3. Alignment of spectra. It is important for our analysis that all of the individual stellar spectra are in the same intrinsic wavelength frame. Since the radial component of the barycentric velocity changes during an observing night, and the absolute wavelength solution of UVES is unstable at the subpixel level, the spectra need to be re-aligned to a common wavelength frame. To do this, Gaussians were fitted to narrow stellar lines close to the sodium D lines in each spectrum to determine the offset relative to a Kurucz model stellar spectrum with atmospheric parameters of $T_{\text{eff}} = 5000 \text{ K}$, $\log(g) = 4.5$ (Castelli & Kurucz 2004) that was Doppler shifted to account for the system velocity of 55 Cnc of $27.58 \pm 0.07 \text{ km s}^{-1}$. These offsets were then used to update the intrinsic wavelength solution for the star. The normalized and aligned spectra are shown in the top panel of Fig. 2.1.
4. Removal of cosmic rays. The standard UVES data reduction recipes do not remove cosmic ray hits for observations made with the image slicer. Therefore, after the UVES spectra were normalized and aligned, cosmic rays were removed by fitting a linear function at each wavelength position through all spectra, so that cosmic rays could be identified as being outliers from the fit. They were then replaced with the interpolated value from the fit. This process was iterated twice with different threshold values so it only identified very strong cosmic rays on the first iteration. This was necessary because

⁶<https://www.eso.org/sci/software/gasgano.html>

⁷<http://www.eso.org/sci/software/cpl/esorex.html>

the presence of very strong cosmic rays could skew the linear fit and cause weaker cosmic rays to be missed.

5. Removal of the stellar absorption features. The stellar spectrum of 55 Cnc was assumed to be constant during a night of observations. This allowed the stellar features to be removed by dividing every observed spectrum from a single night by the median of all of the observed spectra from that night. This only slightly weakened the strength of potential planet absorption lines because they changed wavelength significantly (>100 pixels) during the transit. The resulting spectra are shown in the second panel of Fig. 2.1.
6. Removal of large systematic trends. Significant systematic trends in the residual spectra in the wavelength direction became apparent after the stellar features had been removed. These trends, which differed for different spectra, were fitted with a linear slope, that was subsequently removed at the beginning of Step 2 (see above). Steps 2 to 5 were redone, after which we proceeded with Step 7.
7. Removal of telluric lines with principal component analysis (PCA). Telluric absorption lines change in strength, mainly due to the change in airmass during observations, but also possibly due to variations in the water vapour content of the Earth's atmosphere. We removed the telluric absorptions in the sodium D region using PCA (also known as singular value decomposition) over the time domain. This method relies on the assumption that all of the telluric lines vary in the same way and is discussed in Section 2 of de Kok et al. (2013). Since Step 3 of our data analysis aligned the spectra to the stellar rest frame, the telluric lines show a small shift in position during the night since they are in the rest frame of the observer. However, the PCA algorithm was able to mostly remove the misaligned telluric lines, as shown in the third panel of Fig. 2.1, while the components that were removed are shown in Fig. 2.2. Some weak residual features from the telluric lines remain after the PCA. These are probably caused by the line width of the telluric lines changing slightly during the night. The PCA algorithm is a blind process so if it is allowed to remove a large number of components, it will eventually remove all variation in the data, including the planet signal. However, only four PCA components were required to remove the telluric lines. By injecting artificial planet signals (see Section 2.3.4 and the lower panel of Fig. 2.1) we show that the planet signal is left intact by this procedure.
8. Weighting by noise as a function of wavelength. The values at each wavelength position were subsequently weighted down by the noise, derived from

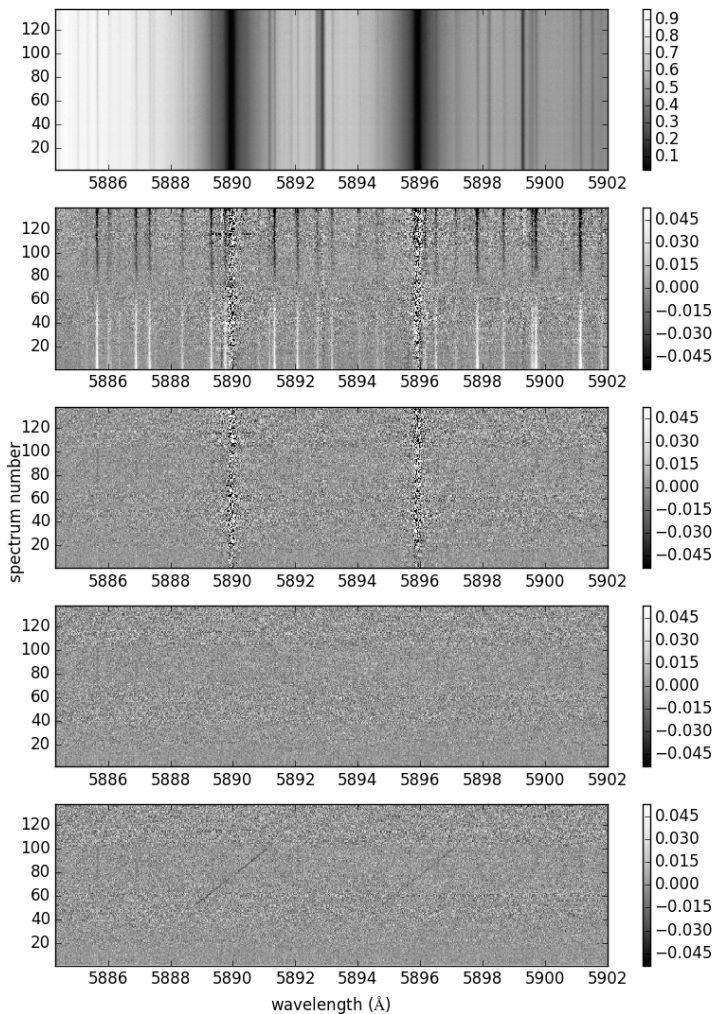


Figure 2.1: Visual representation of the processing steps as described in Section 3. The vertical axis of each matrix represents the sequence number of the observed spectrum. This figure shows the UVES data, but the HARPS and HARPS-N datasets look very similar. The first panel shows the data around the sodium D lines after normalization and alignment in Steps 2 and 3. The second panel shows the residual matrix after dividing through the average star spectrum (Step 5). The third panel shows the residuals after the PCA analysis (Step 7), and the fourth panel shows the same after normalizing each column of the matrix by its standard deviation (Step 8). The bottom panel shows the same data, but after injecting an artificial planet signal before Step 3 - at a level of 3% of the stellar flux. The injected planet signal can be seen as a diagonal trace from spectrum number 53 to 99, resulting from the change in the radial component of the planet orbital velocity during transit.

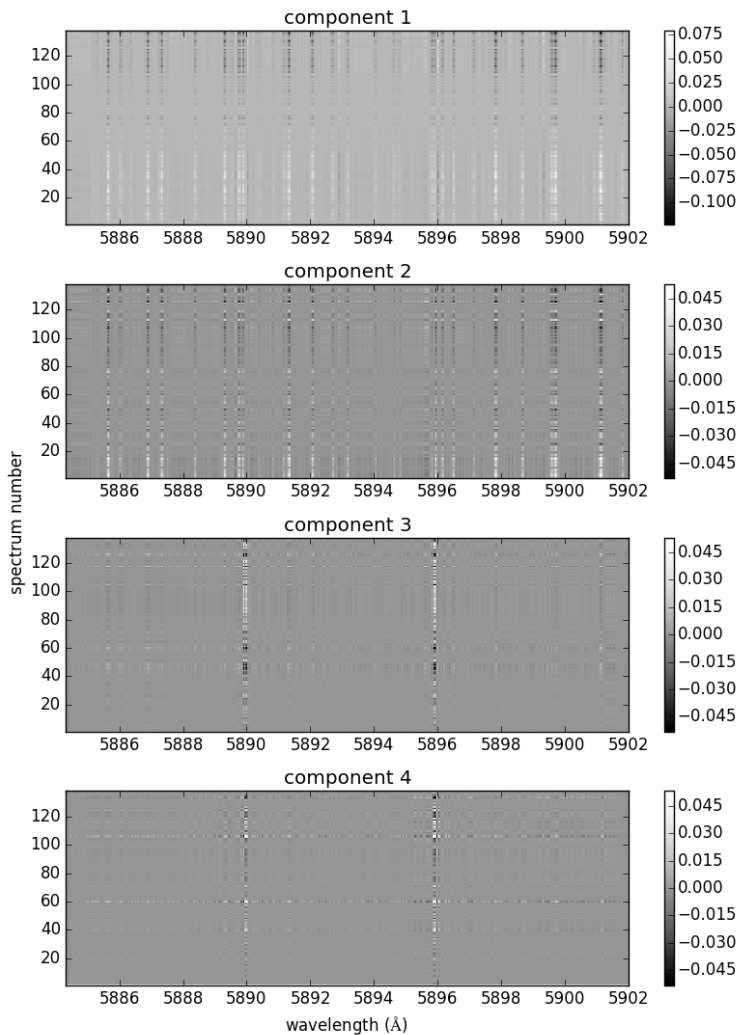


Figure 2.2: Components that were removed by the principle component analysis (PCA) algorithm to remove telluric lines around the Na D lines in the UVES data set. The top panel shows the first component and subsequent panels show the subsequent components, until the fourth component in the bottom panel. The top panel has a different colour scale to the other panels.

the standard deviation of the residuals as function of time at that position. Practically, this only influences the region directly around the cores of the two stellar sodium D lines, as can be seen by comparing panels 3 and 4 of Fig. 2.1. This naturally weighs down the contribution from the spectra during which the planet absorption overlaps with the strong stellar sodium lines. The effect this has on the planet signal is illustrated in panel 5 of Fig. 2.1. An artificial planet signal is injected into the observed spectra (see section 2.3.4) as a 3% absorption relative to the stellar spectrum. This signal is weighted with a box-shaped transit profile which is reasonable for a small planet such as 55 Cnc e. At the mid-transit point when the planet signal is at the same wavelength as the stellar signal (and thus falls in the cores of the Na D lines), the retrieved planet signal is reduced by a factor of approximately 10.

2.3.2 Processing of HARPS and HARPS-N data

Except for small differences, the processing of the HARPS and HARPS-N data was performed in a similar way to that of the UVES data explained above. Since the data retrieved from the data archives of both telescopes is completely reduced and wavelength-calibrated, Step 1 was not needed. In addition, the wavelength calibration of both HARPS and HARPS-N is stable at the 1 m s^{-1} level, and delivered to the user in the restframe of the star. Therefore also step 3 was not needed.

In addition to the sodium D lines (5889.95\AA and 5895.92\AA), the HARPS and HARPS-N spectra also cover the Ca H and K lines (at 3968.47\AA and 3933.66\AA , respectively). While the sodium lines are covered by all data sets, the ionized calcium H and K lines are only present in the HARPS and HARPS-N data and not in the UVES data.

2.3.3 Combining the different data sets

The final step in the analysis is to merge the signal from the two sodium D lines (and calcium H and K lines) and combine the signal from all the in-transit spectra. In addition, we also combine the data sets from the different telescopes.

Two regions of 16 \AA centred on the positions of the Na D₂ and D₁ lines in the residual spectra were averaged with weights proportional to the relative theoretical line strengths. Each spectrum was subsequently shifted to the planet rest frame and added in time over the transit. The signal from the different data sets was subsequently combined using weights proportional to the total in-transit S/N of the data set. The unfavourable observing conditions during the UVES observations caused the UVES observations to have a comparable total S/N to the HARPS and HARPS-N observations (see Table 2.2).

Table 2.2: Signal-to-noise-ratios (S/N) of the data sets.

dataset	average S/N per spectrum	number of spectra during transit	total S/N
UVES	116.3	47	977
HARPS-N B	161.2	18	838
HARPS-N A	223.3	19	1192
HARPS B	109.6	24	658
HARPS A	143.9	24	863

The final data from the calcium H and K lines were produced in the same way using a weighting ratio of Ca K/Ca H = 2 for the two lines.

2.3.4 Injection of artificial planet signals

A useful technique to determine the magnitude of the absorption signal of the planet relative to the stellar spectrum is to inject artificial planet signals early on in the data processing so that the artificial signals are processed in the same way as a real signal would be. This also allows us to check to what level our analysis removes any planet signal. The injection of artificial signals was carried out in a similar way to Snellen et al. (2010) and Hoeijmakers et al. (2015).

The artificial planet signals of the sodium D₁ (5895.92 Å) and D₂ (5889.95 Å) lines were generated using Gaussian line profiles of equal width, and with amplitudes with a ratio of D₂/D₁ = 2. These relative line strengths were calculated according to equation 1 in Sharp & Burrows (2007). We do note that these equations in principle only hold for local thermodynamic equilibrium, while planet exospheres may be better described by radiative transfer algorithms which use a non-Maxwellian velocity distribution function such as in Chaufray & Leblanc (2013). The quantum parameters which describe the Na D line transitions were obtained from the Vienna Atomic Line Database (VALD) (Kupka et al. 2000). The relative strengths of the Na D lines are practically independent of temperature across the range of 1000 to 3000 K. We assumed T = 2000 K.

Using the orbital parameters from Gillon et al. (2012) and assuming a circular orbit (Demory et al. 2012), the radial velocity of the planet can be calculated at the time of each exposure to determine the central wavelengths of the Doppler-shifted sodium lines.

The planet signal was injected into the in-transit data by multiplying the observed spectra with the artificial absorption model according to

$$F(\lambda)_{\text{injected}} = [1 - A \times F_{\text{model}}(\lambda, v_{\text{rad}})]F_{\text{obs}}(\lambda), \quad (2.1)$$

Table 2.3: An estimation of the width of the absorption signal from 55 Cnc e based on the average change of its radial velocity during the exposure of each spectrum in each data set.

Dataset	width (km s ⁻¹)	width (Å)	width (pixels)
UVES	1.3	0.026	1.0
HARPS A	4.0	0.078	4.9
HARPS B	4.0	0.078	4.9
HARPS-N A	5.3	0.105	6.5
HARPS-N B	5.3	0.105	6.5

where $F_{\text{obs}}(\lambda)$ is the observed spectrum, $F_{\text{model}}(\lambda, v_{\text{rad}})$ is the Doppler shifted sodium model spectrum, with A as a scaling parameter that sets the amplitude of the sodium D_2 line, and $F(\lambda)_{\text{injected}}$ is the output spectrum.

During an exposure, the radial component of the orbital velocity of the planet changes significantly. For example, the observations taken with HARPS-N have an exposure time of 240 seconds, during which the planet radial velocity changes by approximately 5 km s⁻¹, corresponding to six resolution elements. Thus, even for an intrinsically narrow planet absorption, the observed signal cannot be narrower than five or six pixels. Therefore, the injected artificial sodium lines have a width equal to this observational broadening, which is different for each data set, as shown in Table 2.3.

The same procedure was used to inject an artificial absorption signal of ionized calcium, using a relative line ratio of Ca K/Ca H = 2 as calculated from Sharp & Burrows (2007).

2.4 Results

2.4.1 Sodium

The results for sodium are shown in Fig. 2.3. The left and right panels show the unbinned data and data binned by five pixels (or 0.05 Å) respectively. From top to bottom the panels show the two HARPS data sets, the two from HARPS-N, the UVES data set, and the signal combined from all telescopes. In these panels, the stellar and telluric signals have been removed so all that remains is residual noise and a possible absorption signal from 55 Cnc e. The noise has an approximately Gaussian distribution, so the statistical significance of the detection can be estimated by comparing the depth of the absorption signal to the standard deviation of the noise. Since any planet signal is expected to be broadened due to the long exposure times, the S/N in the unbinned data, calculated as described above, may

Table 2.4: Observational timing parameters. The orbital phases of 55 Cancri e are based on the orbital parameters derived from the SPITZER + MOST observations used in Gillon et al. (2012).

data set	UVES	HARPS-N B	HARPS-N A	HARPS B	HARPS A
Program Nr.	ESO: 092.C-0178	TNG: CAT13B_33	TNG: CAT13B_33	ESO: 288.C-5010	ESO: 288.C-5010
date (UTC)	2014-01-04	2013-11-29	2013-11-15	2012-03-16	2012-01-28
start	0.871	0.850	0.850	0.944	0.939
phase					
end	0.106	0.108	0.074	0.077	0.093
phase					
cadence (s)	109.0	265.8	264.3	211.4	211.4
exposure					
time (s)	60	240	240	180	180 [†]
observation					
start (UTC)	04:43:03.805	02:10:18.576	02:18:54.502	01:01:25.593	03:56:16.478
transit					
start (UTC)	06:16:30.913	04:05:54.424	04:14:02.316	01:17:26.886	04:16:50.727
mid-transit					
time (UTC)	07:00:13.153	04:49:36.664	04:57:44.556	02:01:09.126	05:00:32.967
transit					
end (UTC)	07:43:55.393	05:33:18.904	05:41:26.797	02:44:51.366	05:44:15.207
observation					
end (UTC)	08:52:37.259	06:44:16.990	06:15:53.853	03:22:45.983	06:39:14.017
NR. spectra	52	26	25	5	6
pre-transit					
NR. spectra	47	18	19	24	24
in transit					
NR. spectra	39	17	9	12	17
post-transit					
total Nr. of spectra	138	61	53	41	47

[†] Except for the first two spectra which have exposure times of 123s

be underestimated.

While there is a hint of planet absorption in the individual UVES data set, this is somewhat more pronounced in the combined (binned) data. This signal has a statistical significance of 3.2σ and 3.3σ in the unbinned and binned data respectively. The binned and unbinned versions of the combined data are also overlaid in Fig. 2.4 for clarity.

By injecting artificial signals at various levels relative to the stellar spectrum we can estimate the strength of the retrieved signal. If real, the planet sodium lines in the combined data are at a level of 2.3×10^{-3} with respect to the star.

2.4.2 Ionized calcium

The results for ionized calcium are shown in Fig. 2.5. The individual panels are the same as in Fig. 2.3, except that UVES is not included because the wavelength range of the UVES data does not cover the calcium H and K lines. In contrast to the sodium data, an interesting signal can be seen in the first HARPS-A data set. It shows a feature that has a statistical significance of 4.9σ , although it is blueshifted with respect to the planet rest frame by approximately 4 km s^{-1} . An overlay of the binned and unbinned data of the HARPS-A data set is shown in Fig. 2.6. The signal does not appear in the other data sets, resulting in a S/N of less than 4 in the combined data.

The contribution to the $4.9\sigma \text{ Ca}^+$ signal from each individual spectrum of the HARPS-A data set is shown in Fig. 2.7. This figure presents the data in the rest-frame of 55 Cnc e so that the features that contribute to the signal lie on a vertical line that is blueshifted by approximately 4 km s^{-1} . The transit duration is indicated in the figure. It can be seen that there are contributions from multiple spectra during transit, indicating that the signal is not caused by a random spurious feature in a single spectrum. If the exosphere is extended beyond the Roche lobe, one would expect it to be distorted and hence possess different velocities relative to the planet and possibly be detectable just before or after transit. However, the S/N in the data is not sufficient to see such distortions or extended absorption signatures.

If real, the planet calcium H and K lines in the HARPS-A data set are at a level of 7.0×10^{-2} with respect to the star.

To assess whether the Ca^+ signal could originate from variability in the stellar Ca^+ H and K lines, we investigated the emission from the cores of the H and K lines in all data sets (Fig. 2.8). We found no evidence for variations in excess of that expected from Poisson noise within each transit data set. Although one dataset (HARPS-N A, hence not corresponding to that showing Ca^+) exhibits stronger Ca H+K emission (55 Cnc has a known 39 day periodicity in its Ca^+ H and K stellar emission lines; Fischer et al. (2008)), it shows no variability during the transit. Also, the radial velocity of 55 Cnc e changes by $\pm 57 \text{ km s}^{-1}$ which causes a

Doppler shift of $\pm 0.75 \text{ \AA}$ relative to the core of the lines. Since the signals across spectra are combined in the planet rest frame, only the spectra taken close to the mid-transit point (where the planet signal is at the same wavelength as the stellar lines) could be influenced by variability in the Ca^+ H and K emission. Therefore, even if there was some variability in emission during a night of observations, its impact on the results would still be limited.

2.5 Discussion and conclusions

In this chapter we carried out a search for neutral sodium (Na) and singly ionized calcium (Ca^+) in the exosphere of the exoplanet 55 Cnc e with transmission spectroscopy. This search yielded a 3.3σ detection of Na after combining five transit data sets and a 4.9σ detection of Ca^+ in only one transit data set.

We estimated the p-value of the Ca^+ detection in one of our four HARPS(-N) data sets. The probability of observing a spurious 4.9σ signal is very low at 4.8×10^{-7} . However, we would have observed such a signal at any velocity between -50 and $+50 \text{ km s}^{-1}$ in the planet rest frame, corresponding to about approximately 20 positions. Multiplying this by the number of transits observed means that we had approximately 80 opportunities to observe a spurious signal, meaning that we can estimate that the false alarm probability is $\sim 80 \times 4.8 \times 10^{-7} \approx 4 \times 10^{-5}$, corresponding to $< 4\sigma$. For this estimate we do not take into account our freedom to use a certain width for the probed signal. In addition, the possible impact of unquantified correlated noise in the data may also increase the p-values. We therefore think these data are as yet insufficient to claim definite detections of the planet exosphere.

As discussed above, the spectral resolution of any potential planet signal is broadened due to the change of the radial component of the planet orbital velocity during an exposure. As shown in Table 2.3, this ‘instrumental’ broadening is five to six pixels for the HARPS and HARPS-N data, and below the intrinsic spectral resolution of the spectrograph for the UVES data, due to the significantly shorter exposure times. In addition, the absorption from sodium and ionized calcium could be intrinsically broadened due to a strong velocity field in the planet exosphere (Mura et al. 2011). If the observed signals from either sodium or ionized calcium are real, they are indeed broad at the five to six pixel (4 km s^{-1}) level, which is much broader than the intrinsic width of the Na D_2 line in the exosphere of Mercury, previously observed by Potter et al. (2013), of approximately 20 m\AA or approximately 1 km s^{-1} .

It is not clear whether to expect the blueshift of approximately 4 km s^{-1} as measured for the potential ionized calcium signal. On the one hand, the photon-ionization lifetime of singly-ionized calcium is estimated to be significantly longer

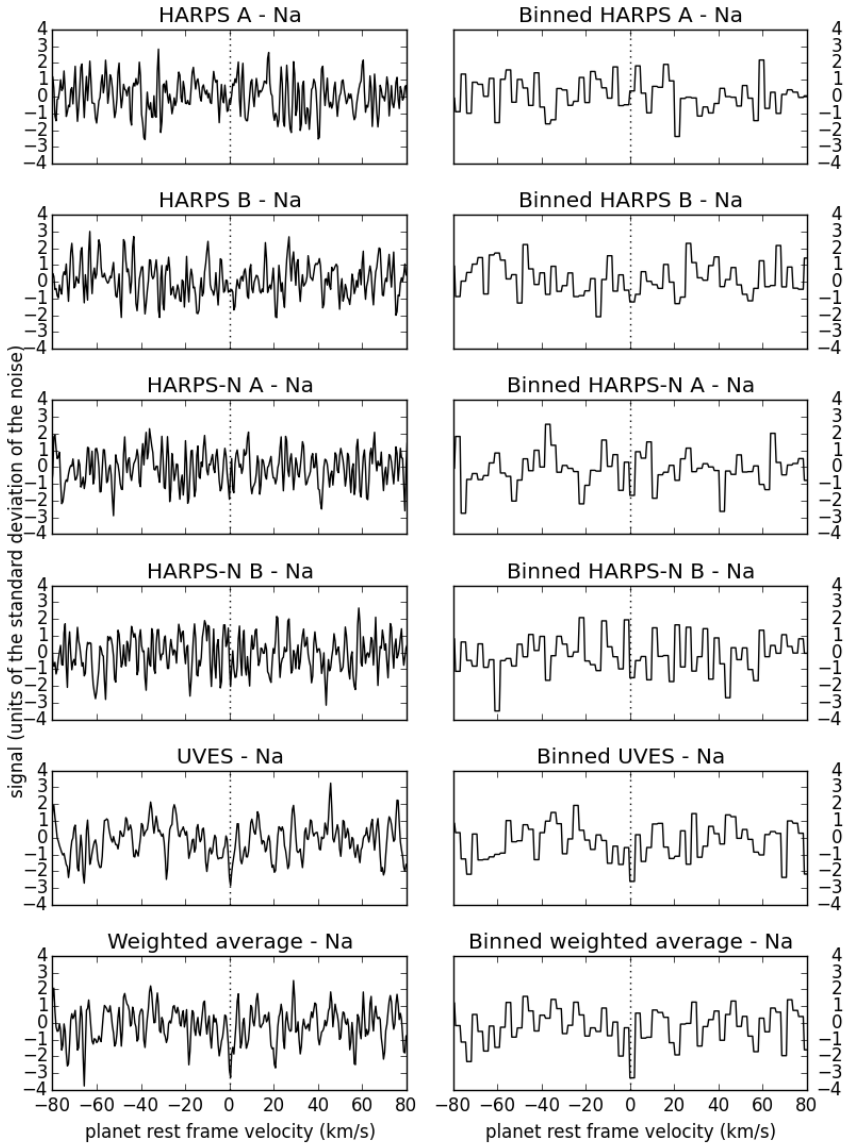


Figure 2.3: Signal of sodium from the individual data sets and from an average of the data sets, weighted according to the S/N of the data set. The signals have been scaled to be in units of the standard deviation of the noise. The left column is not binned while the right column is binned every 0.05 \AA or 3.8 km s^{-1} . The binned average signal has a detection $S/N = 3.3$. The vertical dotted line in all panels indicates a planet rest frame velocity of 0 km s^{-1} .

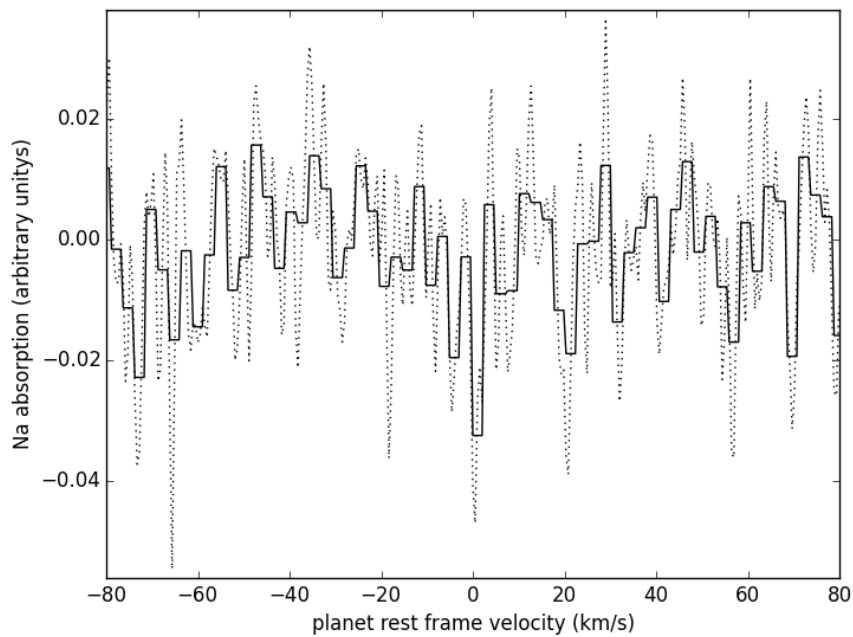


Figure 2.4: Average signal of sodium from all data sets both not binned (dotted line) and binned (solid black line) every 0.05 \AA or 3.8 km s^{-1} (as shown in the bottom panels of Fig. 2.3). This binning regime results in a detection that has a S/N of approximately 3.3σ .

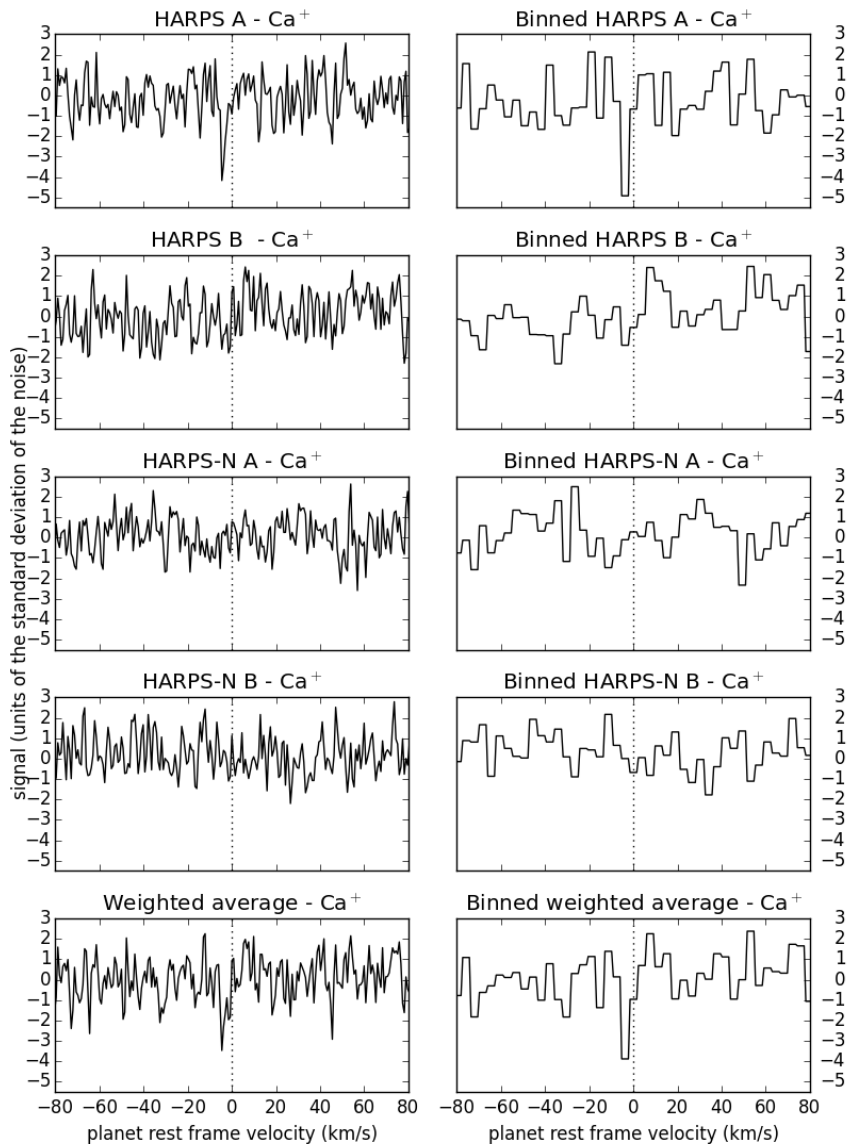


Figure 2.5: Signal of ionized calcium from the individual data sets and from an average of the data sets, weighted according to the S/N of the data set. The signals have been scaled to be in units of the standard deviation of the noise. The left column is not binned while the right column is binned every 0.05 \AA or 3.8 km s^{-1} . The vertical dotted line in all panels indicates a planet rest frame velocity of 0 km s^{-1} . The binned average signal has a detection $S/N = 4.1$; however, this completely originates from the HARPS A data set which individually has a binned detection S/N of 4.9.

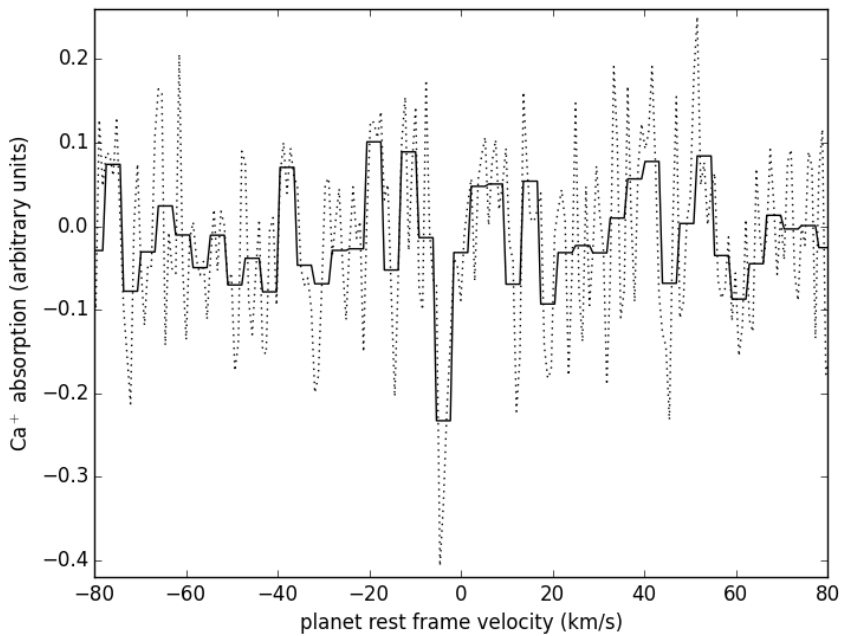


Figure 2.6: Signal of ionized calcium from the HARPS A data set both not binned (dotted line) and binned (solid black line) every 0.05 \AA or 3.8 km s^{-1} (as shown in the bottom panels of Fig. 2.5). This binning regime results in a detection that has a S/N of approximately 4.9σ .

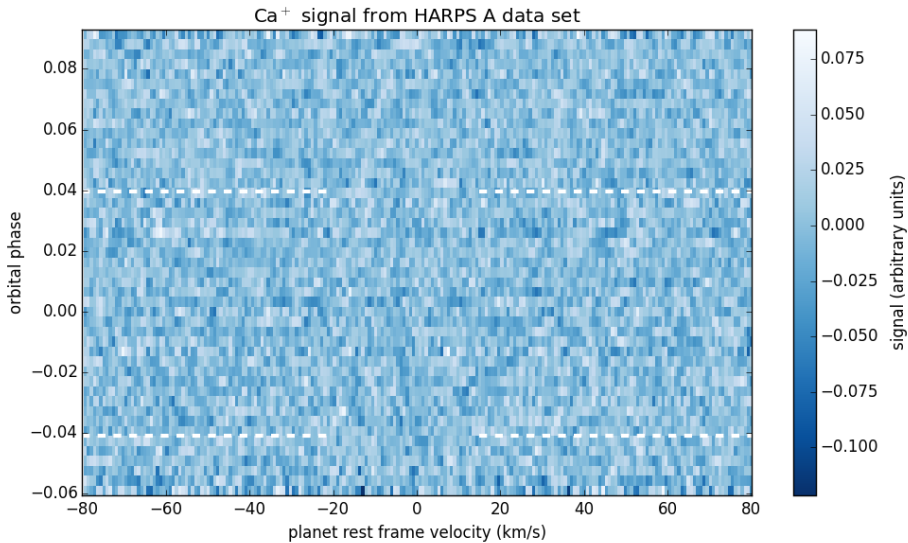


Figure 2.7: Trace of the signal of Ca^+ from the HARPS A data set across the time-series of spectra in the rest frame of 55 Cnc e. In this frame, the planet signal lies on a vertical line, blueshifted by approximately 4 km s^{-1} . Dashed horizontal white lines indicate the transit duration.

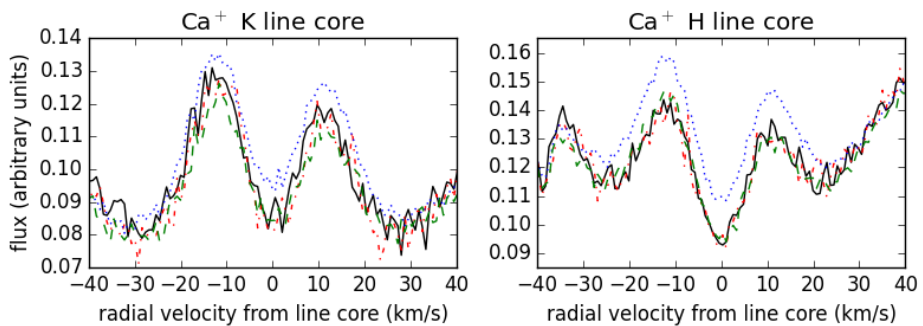


Figure 2.8: Median spectrum of each data set showing the median emission from the cores of the Ca^+ H (right) and K (left) lines. The solid black line is the HARPS A data set, the dotted-dashed red line is the HARPS B data set, the dotted blue line is the HARPS-N A data set and the dashed green line is the HARPS-N B data set. The two panels have different vertical scales.

than that of neutral sodium, which could allow it to accumulate a significant acceleration as it is picked up by the stellar wind and dragged in the anti-stellar direction. On the other hand, if the planet has a significant dipole magnetic field, the ionized calcium may be trapped in the planet's magnetic field (Mura et al. 2011).

If the ionized calcium signal is real, it would imply that this signal is highly variable, since it is only visible in one of the four data sets. As discussed in the introduction, we do know that Mercury's exosphere is highly variable, on a range of timescales from days, to months, to years (Killen et al. 2007). It is not clear at this stage whether we would expect similar behaviour for the exospheres of hot rocky super-Earths. If 55 Cnc e were to have a significant atmosphere, a confirmed detection would be evidence of atmospheric blow-off. On the other hand, if 55 Cnc e does not have a thick atmosphere, as is suggested by Demory et al. (2016) as being a likely interpretation of its longitudinal thermal brightness map, the exosphere would likely be produced by sputtering of the surface.

We modelled the exosphere of 55 Cnc e to first order as an optically thick ring around the planet. Ignoring subtle effects like stellar limb darkening, the fraction of starlight absorbed by sodium and ionized calcium in the exosphere of 55 Cnc e would correspond to an outer radius of the exosphere of $5 R_{\oplus}$ and $25 R_{\oplus}$ respectively - 2.3 and 12 times the radius of the planet. We compare this to the Roche radius of 55 Cnc e, calculated using

$$R_R = \frac{0.49q^{2/3}}{0.6q^{2/3} + \ln(1 + q^{1/3})}, \quad (2.2)$$

where $q = M_{planet}/M_{star}$ (Eggleton 1983), which is found to be $R_R = 5.35 R_{\oplus}$. Hence, the possible sodium signal, if optically thick, would come from a region as large as the planet's Roche lobe, while that of ionized calcium would be significantly larger. If the sodium exosphere were not optically thick, it would also need to be significantly larger than the planet's Roche lobe. If the Ca^+ exosphere really were to have a radius of $25 R_{\oplus}$, it would have an earlier ingress and a delayed egress compared to what would be expected from the radius of the planet as determined by broadband photometry. Using Mandel & Agol (2002), the transit duration for 55 Cnc e with a $25 R_{\oplus}$ exosphere was found to last 26 minutes longer than the broadband transit duration. This corresponds to a range of orbital phases of -0.054 to 0.054 . There may be a hint of this early ingress and delayed egress, as can be seen in Fig. 2.7, however, the S/N is not sufficient to make definite claims.

Although no formal detection has been made, we advocate that probing the exospheres of hot super-Earths in this way has great potential, also knowing that Mercury's exosphere varies significantly over time. It may be a fast route towards the first characterization of the surface properties of this enigmatic class of planets. Our team is pursuing a transit monitoring programme with UVES to further

investigate the possible variable signal from ionized calcium.

Acknowledgements

A. R. R.-H. is grateful to the Planetary and Exoplanetary Science (PEPSci) programme of the Netherlands Organisation for Scientific Research (NWO) for support. I. A. G. S. acknowledges support from an NWO VICI grant (639.043.107). M. B. acknowledges support by NASA, through Hubble Fellowship grant HST-HF2-51336 awarded by the Space Telescope Science Institute. We thank the anonymous referee for their constructive comments.

Bibliography

- Ballester, P., Modigliani, A., Boitquin, O., et al. 2000, *The Messenger*, 101, 31
- Bonfils, X., Delfosse, X., Udry, S., et al. 2013, *A&A*, 549, A109
- Bourrier, V., Lecavelier des Etangs, A., & Vidal-Madjar, A. 2014, *A&A*, 565, A105
- Castelli, F. & Kurucz, R. L. 2004, *ArXiv Astrophysics e-prints*
- Chaufray, J.-Y. & Leblanc, F. 2013, *Icarus*, 223, 975
- Cosentino, R., Lovis, C., Pepe, F., et al. 2012, in *Society of Photo-Optical Instrumentation Engineers (SPIE) Conference Series*, Vol. 8446, *Society of Photo-Optical Instrumentation Engineers (SPIE) Conference Series*, 1
- de Kok, R. J., Brogi, M., Snellen, I. A. G., et al. 2013, *A&A*, 554, A82
- de Mooij, E. J. W., López-Morales, M., Karjalainen, R., Hrudkova, M., & Jayawardhana, R. 2014, *ApJ*, 797, L21
- Dekker, H., D’Odorico, S., Kaufer, A., Delabre, B., & Kotzłowski, H. 2000, in *Society of Photo-Optical Instrumentation Engineers (SPIE) Conference Series*, Vol. 4008, *Optical and IR Telescope Instrumentation and Detectors*, ed. M. Iye & A. F. Moorwood, 534–545
- Demory, B.-O., Gillon, M., de Wit, J., et al. 2016, *Nature*, 532, 207
- Demory, B.-O., Gillon, M., Deming, D., et al. 2011, *A&A*, 533, A114
- Demory, B.-O., Gillon, M., Madhusudhan, N., & Queloz, D. 2015, *ArXiv e-prints*
- Demory, B.-O., Gillon, M., Seager, S., et al. 2012, *ApJ*, 751, L28
- D’Odorico, S., Cristiani, S., Dekker, H., et al. 2000, in *Society of Photo-Optical Instrumentation Engineers (SPIE) Conference Series*, Vol. 4005, *Discoveries and Research Prospects from 8- to 10-Meter-Class Telescopes*, ed. J. Bergeron, 121–130
- Eggleton, P. P. 1983, *ApJ*, 268, 368
- Ehrenreich, D., Bourrier, V., Bonfils, X., et al. 2012, *A&A*, 547, A18
- Ehrenreich, D., Bourrier, V., Wheatley, P. J., et al. 2015, *Nature*, 522, 459
- Fischer, D. A., Marcy, G. W., Butler, R. P., et al. 2008, *ApJ*, 675, 790
- Gillon, M., Demory, B.-O., Benneke, B., et al. 2012, *A&A*, 539, A28
- Guenther, E. W., Cabrera, J., Erikson, A., et al. 2011, *A&A*, 525, A24
- Hoeijmakers, H. J., de Kok, R. J., Snellen, I. A. G., et al. 2015, *A&A*, 575, A20

- Killen, R., Cremonese, G., Lammer, H., et al. 2007, *Space Sci. Rev.*, 132, 433
- Kupka, F., Ryabchikova, T., Piskunov, N., Stempels, H., & Weiss, W. 2000, *Baltic Astronomy*, 9, 590
- Lammer, H., Wurz, P., Patel, M. R., et al. 2003, *Icarus*, 166, 238
- Larimer, J. W. 1975, *Geochim. Cosmochim. Acta*, 39, 389
- Lecavelier des Etangs, A., Bourrier, V., Wheatley, P. J., et al. 2012, *A&A*, 543, L4
- Lecavelier des Etangs, A., Ehrenreich, D., Vidal-Madjar, A., et al. 2010, *A&A*, 514, A72
- Linsky, J. L., Yang, H., France, K., et al. 2010, *The Astrophysical Journal*, 717, 1291
- López-Morales, M., Triaud, A. H. M. J., Rodler, F., et al. 2014, *ApJ*, 792, L31
- Madhusudhan, N., Lee, K. K. M., & Mousis, O. 2012, *ApJ*, 759, L40
- Mandel, K. & Agol, E. 2002, *ApJ*, 580, L171
- Mayor, M., Pepe, F., Queloz, D., et al. 2003, *The ESO Messenger*, 114, 20
- McArthur, B. E., Endl, M., Cochran, W. D., et al. 2004, *ApJ*, 614, L81
- Morgan, T. H., Zook, H. A., & Potter, A. E. 1988, *Icarus*, 75, 156
- Mura, A., Wurz, P., Schneider, J., et al. 2011, *Icarus*, 211, 1
- Nelson, B. E., Ford, E. B., Wright, J. T., et al. 2014, *MNRAS*, 441, 442
- Nidever, D. L., Marcy, G. W., Butler, R. P., Fischer, D. A., & Vogt, S. S. 2002, *ApJS*, 141, 503
- Potter, A. & Morgan, T. 1985, *Science*, 229, 651
- Potter, A. E., Killen, R. M., Reardon, K. P., & Bida, T. A. 2013, *Icarus*, 226, 172
- Potter, A. E. & Morgan, T. H. 1990, *Science*, 248, 835
- Raymond, S. N., Barnes, R., & Mandell, A. M. 2008, *MNRAS*, 384, 663
- Schaefer, L. & Fegley, B. 2009, *ApJ*, 703, L113
- Sharp, C. M. & Burrows, A. 2007, *ApJS*, 168, 140
- Smyth, W. H. & Marconi, M. L. 1995, *ApJ*, 441, 839
- Snellen, I. A. G., de Kok, R. J., de Mooij, E. J. W., & Albrecht, S. 2010, *Nature*, 465, 1049
- Teske, J. K., Cunha, K., Schuler, S. C., Griffith, C. A., & Smith, V. V. 2013, *The Astrophysical Journal*, 778, 132

Valencia, D., Ikoma, M., Guillot, T., & Nettelmann, N. 2010, *A&A*, 516, A20

Valencia, D., O'Connell, R. J., & Sasselov, D. 2006, *Icarus*, 181, 545

van Leeuwen, F. 2007, *A&A*, 474, 653

Vidal-Madjar, A., Désert, J.-M., Lecavelier des Etangs, A., et al. 2004, *ApJ*, 604, L69

Vidal-Madjar, A., Huitson, C. M., Bourrier, V., et al. 2013, *A&A*, 560, A54

Vidal-Madjar, A., Lecavelier des Etangs, A., Désert, J.-M., et al. 2003, *Nature*, 422, 143

von Braun, K., Boyajian, T. S., ten Brummelaar, T. A., et al. 2011, *ApJ*, 740, 49

Winn, J. N., Matthews, J. M., Dawson, R. I., et al. 2011, *ApJ*, 737, L18

3 | Chromatic transit light curves of disintegrating rocky planets

Based on:

Ridden-Harper, A. R.; Keller, C. U.; M. Min; R. van Lieshout; Snellen, I. A. G., A&A (2018), in press.

Context. Kepler observations have revealed a class of short period exoplanets, of which Kepler-1520 b is the prototype, which have comet-like dust tails thought to be the result of small, rocky planets losing mass. The shape and chromaticity of the transits constrain the properties of the dust particles originating from the planet's surface, offering a unique opportunity to probe the composition and geophysics of rocky exoplanets.

Aims. We aim to approximate the average Kepler long-cadence light curve of Kepler-1520 b and investigate how the optical thickness and transit cross-section of a general dust tail can affect the observed wavelength dependence and depth of transit light curves.

Methods. We developed a new 3D model that ejects sublimating particles from the planet surface to build up a dust tail, assuming it to be optically thin, and used 3D radiative transfer computations that fully treat scattering using the distribution of hollow spheres (DHS) method, to generate transit light curves between 0.45 and 2.5 μm .

Results. We show that the transit depth is wavelength independent for optically thick tails, potentially explaining why only some observations indicate a wavelength dependence. From the 3D nature of our simulated tails, we show that their transit cross-sections are related to the component of particle ejection velocity perpendicular to the planet's orbital plane and use this to derive a minimum ejection velocity of 1.2 km s^{-1} . To fit the average transit depth of Kepler-1520 b of 0.87%, we require a high dust mas-loss rate of 7 – 80 $M_{\oplus} \text{Gyr}^{-1}$ which implies planet lifetimes that may be inconsistent with the observed sample. Therefore, these mass-loss rates should be considered to be upper limits.

3.1 Introduction

Exoplanetary systems are found to exhibit a large diversity in system architecture, planet size, composition and temperature. An intriguing recent addition to this diversity is the class of close-in, rocky exoplanets that have large comet-like tails, consisting of dust particles that are thought to originate from the rocky planet as a result of the rocky planet losing mass.

The term comet-like tail was first used in an explanatory context by Vidal-Madjar et al. (2003) to describe their discovery of a stream of hydrogen atoms escaping from the evaporating atmosphere of the hot-Jupiter type exoplanet HD 209458 b and has subsequently been used to describe three other similar planets. A similarity between the gas- and dust-tails is that they are both shaped by radiation pressure¹.

The transit light curves produced by dust tails from disintegrating rocky exoplanets are asymmetrical due to the extended tails decreasing in density along the tail, away from the planet. They also feature forward-scattering peaks at ingress, and in some cases, egress (e.g. Rappaport et al. 2012, 2014; Brogi et al. 2012; van Lieshout et al. 2014; Sanchis-Ojeda et al. 2015; van Lieshout et al. 2016). To date, three such planets around main-sequence stars and one around a white dwarf have been discovered from Kepler light curves: Kepler-1520 b (also known as KIC 12557548 b) (Rappaport et al. 2012), KOI-2700 b (Rappaport et al. 2014), K2-22 b (Sanchis-Ojeda et al. 2015) and WD 1145+017 (Vanderburg et al. 2015). These planets all have orbital periods of less than one day and exhibit variable transit depths, with WD 1145+017 exhibiting transit depths of up to 40%. The dust in the tails of disintegrating rocky exoplanets originates from the outer parts of the planet. Therefore, these objects present the exciting opportunity to observationally probe the outer composition of rocky exoplanets, which would be very valuable information for constraining models of their structure and geophysics.

Kepler-1520 b has been relatively well studied, and constraints on its mean particle size, mass-loss rate (assuming an optically thin tail) and particle composition have been determined by fitting models to the Kepler light curves, and by searching for a wavelength dependence in the transit depth with spectrophotometric observations. The first constraints on the particle size and mass-loss rate for Kepler-1520 b were derived by Rappaport et al. (2012) in their discovery paper. Assuming an optically thin tail, they derived a mass loss rate of $1 M_{\oplus} \text{Gyr}^{-1}$. This was further refined by Perez-Becker & Chiang (2013) who show with improved models that for possibly porous grains with radius $>0.1 \mu\text{m}$, the mass loss

¹Although, the tail of HD 189733 b has a large blue shift that is best explained by charge exchange interaction with the stellar wind. (Vidal-Madjar et al. 2003; Ehrenreich et al. 2012; Rappaport et al. 2012; Bourrier et al. 2014; Ehrenreich et al. 2015; Holmström et al. 2008; Ekenbäck et al. 2010; Bourrier et al. 2013; Bourrier & Lecavelier des Etangs 2013).

rate can have a lower value of $\gtrsim 0.1 M_{\oplus} \text{Gyr}^{-1}$. Brogi et al. (2012) develop a one-dimensional model of the dust tail with an exponentially decaying angular dust density away from the planet and derived a typical particle size of $0.1 \mu\text{m}$. A complementary study carried out by Budaj (2013) modelled the dust tail as a complete or partial ring where the density varied as a power law or an exponential as a function of angular distance from the planet. One of their main results is that the system was found to be best modelled with at least two components, one consisting of the transit core and the other producing the tail. This is validated by van Werkhoven et al. (2014) with their implementation of a two-dimensional, two component model consisting of an exponential tail and an opaque core, which gave an improved fit to the Kepler short-cadence light curves.

Some interesting constraints have been applied to the composition of the dust particles in the tail of Kepler-1520 b. van Lieshout et al. (2014) find the grains to be consistent with being composed of corundum (Al_2O_3) or iron-rich silicate materials. This work is extended by van Lieshout et al. (2016) in which a self-consistent numerical model was developed to calculate the dynamics of the sublimating dust particles and generate synthetic light curves. They find that good fits to the observed light curves can be obtained with initial particle sizes between 0.2 and $5.6 \mu\text{m}$ and mass-loss rates of 0.6 to $15.6 M_{\oplus} \text{Gyr}^{-1}$. Furthermore, they find the dust composition to be consistent with corundum (Al_2O_3) but not with several carbonaceous, silicate or iron compositions.

In addition to fitting the average Kepler light curves, information about the particle composition and size can be derived from spectrophotometric observations. Croll et al. (2014) observe transits of Kepler-1520 b at $2.15 \mu\text{m}$, $0.53 \mu\text{m}$ – $0.77 \mu\text{m}$ and utilise the Kepler light curve at $0.6 \mu\text{m}$ and found no wavelength dependence in transit depth. They report that if the observed scattering was due to particles of a single size, the particles would have to be at least $0.5 \mu\text{m}$ in radius. Murgas (2013) observed three transits and one secondary eclipse of Kepler-1520 b with OSIRIS on the GTC and also found no evidence for a wavelength dependence in transit depth.

Schlawin et al. (2016) carried out a complementary search for a wavelength dependence in the transit depth of Kepler-1520 b to constrain the particle size. They observe eight transits with the SpeX spectrograph and the MORIS imager on the Infrared Telescope Facility, with a wavelength coverage of $0.6 - 2.4 \mu\text{m}$, and one night in H band ($1.63 \mu\text{m}$). They report a flat transmission spectrum, consistent with the particles being $\gtrsim 0.5 \mu\text{m}$ for pyroxene and olivine or $\gtrsim 0.2 \mu\text{m}$ for iron and corundum.

Bochinski et al. (2015) observe five transits with ULTRACAM on the 4.2 m William Herschel Telescope. In contrast to the previously discussed results which indicate a wavelength independent transit depth, Bochinski et al. (2015) report a

wavelength dependence to a confidence of 3.2σ . These transit depths are consistent with absorption by interstellar medium (ISM) like material with grain sizes corresponding to the largest found in the ISM of $0.25 - 1 \mu\text{m}$.

The exoplanet K2-22 b was discovered and characterised by Sanchis-Ojeda et al. (2015). They observe transits with several ground based 1m class telescopes and the Gran Telescopio Canarias (GTC). Their observations reveal it to have highly variable transit depths from 0 to 1.3%, variable transit shapes, and on one occasion, a significant wavelength dependence. They infer that the distribution of dust particle sizes (a) must be a non-steep power-law, $dN/da \propto a^{-\Gamma}$ with $\Gamma \simeq 1 - 3$ with maximum sizes in the range of $0.4 - 0.7 \mu\text{m}$. They also determine its tail to be leading (instead of trailing) the planet. The leading tail requires the dust to be transported to a distance of about twice the planetary radius towards the host star where it effectively overflows the planet's Roche lobe and goes into a faster orbit than that of the planet, allowing it to move in front of the planet. This can be accomplished with particles that have β (the ratio to radiation pressure force to gravitational force) $\lesssim 0.02$ which is possible for a very low luminosity host star with very small ($\lesssim 0.1 \mu\text{m}$) or very large ($\gtrsim 1 \mu\text{m}$) dust particles. Alonso et al. (2016) observe several transits of disintegrating planetesimals around the white dwarf WD 1145+017 with the Gran Telescopio Canarias (GTC) and found no wavelength dependence in transit depth in bands centred on 0.53, 0.62, 0.71 and $0.84 \mu\text{m}$.

We have developed a new 3D model to investigate how the optical thickness and transit cross-section of a general dust tail can affect the wavelength dependence and depth of transit light curves. Our model builds up a tail by ejecting particles from the surface of the planet with a velocity relative to the planet and tracks them until they vanish due to sublimation, in contrast to the models of Brogi et al. (2012), Budaj (2013), van Werkhoven et al. (2014), Rappaport et al. (2014) and Sanchis-Ojeda et al. (2015) who assume a density profile in the tail.

van Lieshout et al. (2016) release particles from the centre of the planet with zero velocity relative to the planet and without considering the effect of the planet's gravity. To generate synthetic light curves, they calculated the individual contribution of each particle, taking into account its scattering cross-section and phase function, its extinction cross-section, and the local intensity of the stellar disk. They then scaled these contributions by the mass-loss rate of the planet. This limited them to only generating light curves for optically thin tails. However, they also showed that in reality, the tail would likely have an optically thick component near the planet.

This chapter is structured as follows: in Section 3.2 we describe our new model and Section 3.3 shows the results of some instructive tail simulations. Section 3.4 explores how the wavelength dependence in transit depth depends on the optical

depth of the tail, while in Section 3.5 we discuss how a lower limit on particle ejection velocity can be determined from the transit depth. Finally, Section 3.6 discusses the limitations and implications of the presented results and Section 3.7 summarises the main results.

3.2 Method: The model

3.2.1 Dust dynamics code

Our model builds up a 3D tail by ejecting tens of thousands of meta-particles from the surface of the rocky planet, where each meta-particle represents a large number of particles. The meta-particles can be launched in variable directions with variable speeds, allowing different launch mechanisms to be modelled. Each individual dust meta-particle experiences a radiation pressure force away from the star, a gravitational force towards the star, and the gravitational force towards the planet. The inclusion of the gravitational attraction of the planet means that meta-particles with low launch velocities will follow ballistic trajectories and return to the surface of the planet.

The ratio of radiation pressure force and gravitational force towards the star, β , is independent of distance from the star and only depends on the particle's scattering properties which are determined by its composition, radius and shape (e.g. Burns et al. 1979). Our values of β were computed as in van Lieshout et al. (2014) by integrating the radiation pressure over the spectrum of the star for a particle composition of corundum which was found by van Lieshout et al. (2016) to be consistent with the observations, however, other compositions such as iron-rich silicates are also possible. Our simulated dust meta-particles become smaller with time due to sublimation and β changes correspondingly.

In reality, additional forces act on these particles, however they were neglected in this work because they produce much smaller effects. Poynting-Robertson drag only becomes significant over many orbits (van Lieshout et al. 2016) and can therefore be neglected because the lack of any correlation between transit depths implies that on average particles do not live longer than one orbit (van Werkhoven et al. 2014). Rappaport et al. (2014) show in their Appendix A that the stellar wind ram pressure is expected to be one to two orders of magnitude less significant than the radiation pressure so it was also ignored in this work.

This model was implemented in a rotating coordinate system that was centred on the star and rotated with the planet's orbital velocity so that the planet remained at the same coordinates throughout its orbit. In this reference frame the meta-particles do not move very far over the grid in a single time step. The equa-

tion of motion in this co-rotating reference frame is

$$\frac{d^2\vec{r}}{dt^2} = - \underbrace{\frac{GM_*(1 - \beta(a))}{|\vec{r}|^3}}_{\text{stellar gravity and radiation pressure}} \vec{r} - \underbrace{2\boldsymbol{\omega} \times \frac{d\vec{r}}{dt}}_{\text{Coriolis}} - \underbrace{\boldsymbol{\omega} \times (\boldsymbol{\omega} \times \vec{r})}_{\text{centrifugal}} - \underbrace{\frac{Gm_p}{|\vec{d}|^3} \vec{d}}_{\text{planetary gravity}} \quad (3.1)$$

where $\boldsymbol{\omega}$ is the angular velocity vector of the planet, \vec{r} is the vector from the star to the dust particle, \vec{d} is the vector from the planet to the dust particle, M_* is the mass of the star, and m_p is the mass of the planet. This equation of motion was integrated using Python's `odeint`², which uses `Isoda` from the FORTRAN library `odepack`. This equation of motion changes from having relatively stable solutions (non-stiff) to having potentially unstable solutions (stiff) throughout the motion of a dust particle. The `odeint` package automatically determines whether an equation is non-stiff, allowing it to be accurately integrated with the fast Adams' method or stiff, requiring it to be integrated with the slower but more accurate backward-differentiation formula (BDF).

This model allows for meta-particles to be ejected with arbitrary spatial and temporal distributions so that a variety of possible ejection scenarios can be investigated, such as a spherically symmetric continuous outflow, or directed outbursts from a volcano. However, in this work we have focussed on a simple, spherically symmetric outflow, where the meta-particle ejection direction is uniformly randomly distributed over a sphere because as was pointed out by Rappaport et al. (2012), if the planet is tidally locked the particles might be expected to stream off the hot day-side, but if there are horizontal winds on the planet, the material could be redistributed around the planet.

There are several important free parameters that have an impact on the tail morphology and resulting light curves. All of these parameters are shown in Table 3.1, along with their typical values.

After the meta-particles are ejected from the planet, they sublime until they reach a radius of 1 nm and are removed from the simulation. We assumed a simple sublimation rate that was constant for all meta-particles and over all meta-particle radii. In reality, the sublimation rate would be more complex and would depend on the compositions, shapes and temperatures of the particles which was partially exploited by van Lieshout et al. (2014, 2016) to constrain the particle composition. However, for this work our focus was on investigating how the transit depth varied as a function of wavelength and meta-particle ejection velocity for a general tail, so our only requirements on the sublimation rate were that it produced a tail of

²<https://docs.scipy.org/doc/scipy-0.18.1/reference/generated/scipy.integrate.odeint.html#scipy.integrate.odeint>

Table 3.1: Fiducial model input parameters.

Parameter	Value
composition	corundum (Al_2O_3) ⁽¹⁾
grain density	4.02 g cm^{-3}
Initial meta-particle radius	$1 \mu\text{m}$
Sublimation radius	1 nm
Particle launch direction	spherically symmetric ⁽²⁾
Total number of meta-particles	5×10^4 ⁽³⁾
Number of orbits	1
Time steps per orbit	500
Sublimation rate	$-1.77 \times 10^{-11} \text{ m s}^{-1}$
Planet density	5427 kg m^{-3} ⁽⁴⁾
Semi-major axis	0.0131 au ⁽⁵⁾
Planet radius #1	$0.0204 R_{\oplus}$ ⁽⁶⁾
Planet mass #1	$8.36 \times 10^{-6} M_{\oplus}$
Planet radius #2	$0.277 R_{\oplus}$
Planet mass #2	$0.020 M_{\oplus}$
Grid parameters	
Radial grid	
Inner radius	0.0130 au
Outer radius	0.0150 au
Bin size	1.50×10^6
Elevation grid ($0^\circ - 180^\circ$)	
Lower elevation	89° ⁽⁷⁾
Upper elevation	91° ⁽⁸⁾
Bin size	0.0526°
Azimuthal grid ($0^\circ - 360^\circ$)	
Bin size	0.5°

⁽¹⁾ From van Lieshout et al. (2016).⁽²⁾ Since the dust may be subject to horizontal winds on the planet that can distribute material from the substellar point to the night side (Rappaport et al. 2012).⁽³⁾ The number of particles that each meta-particle represented was scaled to set the planet's mass-loss rate to the desired value.⁽⁴⁾ Equal to the bulk density of Mercury.⁽⁵⁾ See footnote 4.⁽⁶⁾ The upper-limit determined by van Werkhoven et al. (2014) is $0.7 R_{\oplus}$.⁽⁷⁾ With an additional large bin containing $0^\circ - 89^\circ$.⁽⁸⁾ With an additional large bin containing $91^\circ - 180^\circ$.

reasonable length and that meta-particles did not survive for longer than one orbit (since there is no correlation between consecutive transit depths (van Werkhoven et al. 2014)), making our simple approximation reasonable.

Our model continuously ejects a stream of meta-particles so that at every time step of the simulation, there are several thousand spatially separated meta-particles populating the tail. This enables us to investigate whether the optical depth in the radial direction through the tail can reduce the flux (and radiation pressure) on shielded dust meta-particles enough to affect the tail’s morphology. However, that is beyond the scope of this chapter and will be presented in Chapter 4.

Our planet properties were chosen in the following way. The trialled planet mass of $8.36 \times 10^{-6} M_{\oplus}$ (#1) was chosen by trial-and-error so that the planet’s gravity would have a very small effect on the meta-particles’ motion and the trialled planet mass of $0.02 M_{\oplus}$ (#2) was chosen because it was found by Perez-Becker & Chiang (2013) to be its most likely current mass. The planet’s bulk density was chosen to be equal to that of Mercury because that assumption has been previously made (e.g. Perez-Becker & Chiang 2013). This density was used to calculate the radii corresponding to the trialled masses, assuming a spherical planet.

In all of our tail simulations, we used a constant initial meta-particle size instead of a distribution. This was primarily for simplicity because the radiative transfer component of our model (see Section 3.2.3) is too slow to allow the model parameters to be constrained in a Markov-chain Monte-Carlo (MCMC) manner. We chose an initial meta-particle size of $1 \mu\text{m}$ as this was generally consistent with the findings of previous studies (see Section 3.1) and also with dynamical constraints discussed in Section 3.3.5.

3.2.2 Particle dynamics simulations

To validate our code, we studied the tracks of non-sublimating particles, which have a constant β , that were released from the planet centre with zero velocity relative to the planet. The values of β were such that the particles stayed in bound orbits, which is true for $\beta < 0.5$ (Rappaport et al. 2014). Such bound particles should form rosette-like shapes in the co-rotating frame over many orbits, as is shown in Fig. 2 of van Lieshout et al. (2016) and Fig. 7 of Rappaport et al. (2014). We reproduce Fig. 7 of Rappaport et al. (2014) in our Fig. 3.1, showing perfect agreement and hence confirming that the numerical accuracy of our dynamics code was sufficient to reliably solve the equation of motion describing the motion of the particles.

If the particles are ejected from the surface of the planet with some velocity relative to the planet, the track of each particle differs from the track produced by releasing the particles from the centre of the planet. This is shown in Fig. 3.2

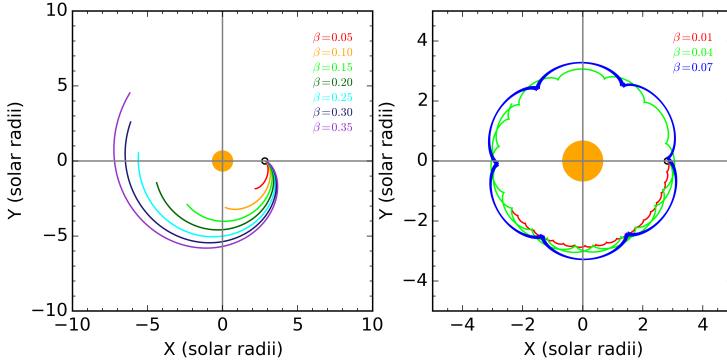


Figure 3.1: Reproduction of the particle tracks shown in Fig. 7 of Rappaport et al. (2014) to validate the accuracy of our particle dynamics code. Both panels show the tracks of non-sublimating particles in the corotating frame of the planet. Left: Tracks of particles after one planetary orbit for radiation pressure force to gravitational force ratios, β , that vary from 0.05 to 0.35. Right: Same as left but for 20 planetary orbits, with $\beta = 0.01, 0.04$ and 0.07 . The cusps are the periastron passages of the dust particles. The orange circle represents the approximate size of the host star, Kepler-1520.

which shows the tracks of spherical particles of corundum of radius $1 \mu\text{m}$, with $\beta = 0.038$. It can be seen in Fig. 3.1 that when all the particles are released from the centre of the planet with no relative velocity, the perihelion point forms a cusp for all particles. However, when the particles are ejected from the surface of a planet of mass $8.4 \times 10^{-6} M_{\oplus}$ and radius $0.020 R_{\oplus}$ with a velocity of 1.2 times the surface escape velocity (272 m s^{-1}) the perihelion point is not the same for all particles and depends on the ejection velocity. This causes the local enhancement in density at the perihelion cusp to be spread slightly along the planet’s orbit.

To ensure that our constant time steps were small enough to enable Eq. 3.1 to be accurately solved, we doubled the number of time steps, which changed the average displacement between individual meta-particles by less than 0.5 planetary radii (assuming a planet radius of $0.28 R_{\oplus}$). This is negligible compared to the size of the tail, which has a maximum extent perpendicular to the planet’s orbital plane of 10 – 20 planetary radii and typical length of 1000 planetary radii.

3.2.3 Ray tracing with MCMMax3D

The code described in Section 3.2.1 simulates the dynamics of the dust meta-particles in the tail but does not generate light curves. To generate light curves, we employed the radiative transfer code MCMMax3D³ (Min et al. 2009). MCMMax3D

³<http://www.michielmin.nl/codes/mcmax3D/>

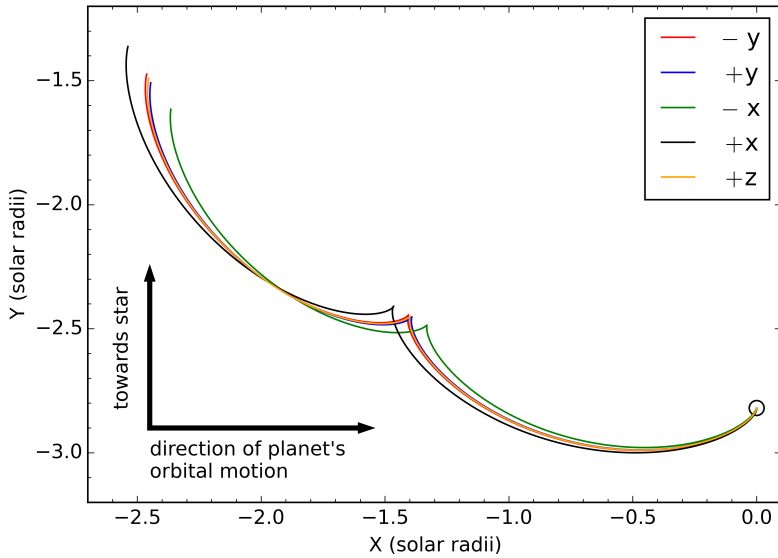


Figure 3.2: Trajectories after one planetary orbit of non-sublimating particles of corundum of radius $1 \mu\text{m}$ with $\beta = 0.038$ after being ejected in different directions from the surface of a planet of radius $0.020 R_{\oplus}$ and mass $8.4 \times 10^{-6} M_{\oplus}$. The particles were ejected with a velocity of 1.2 times the surface escape velocity (272 m s^{-1}) towards the star at the top of the page (+y), in the anti-stellar direction towards the bottom of the page (-y), in the direction of the planet's orbital motion to the right of the page (+x), in the anti-orbital motion direction to the left of the page (-x) and perpendicular to the orbital plane, out of the page (+z). This coordinate system is rotating around the z axis so the track for -z is the same as for +z. The planet is indicated by the circle (not to scale).

was originally designed to generate circumstellar disk density distributions and carry out Monte Carlo radiative transfer. We modified MCMa3D, to take an arbitrary mass density distribution file as an input. The code described in Section 3.2.1 converts the distribution of individual meta-particles to a continuous mass density distribution for MCMa3D. The density is calculated on a spherical grid surrounding the star that has cell dimensions that were chosen so that there were always several meta-particles per cell and that the distribution was always continuous, without unpopulated cells between populated cells. This density grid was also used for the radiative transfer, and consisted of 200 evenly spaced bins in the radial direction ranging from 0.0130 – 0.0150 au from the centre of the star (with the fiducial semi-major axis of Kepler-1520 b being 0.0131 au⁴), 720 evenly spaced bins in the azimuthal direction, ranging from 0 to 360°, and 40 bins of elevation angle ranging from 0 to 180° (where the planet’s orbital plane is at 90°), with the first bin containing 0–89°, the last bin containing 91–180° and the remaining 2° close to the orbital plane being covered by 38 evenly spaced bins. The grid boundaries were set such that the planet fell on an intersection of grid lines so that meta-particles released from different sides of the planet would be in different grid cells. Since the 3D spherical grid completely surrounded the star, most of the grid cells were empty, however some cells contained mass, distributed in the same way as the tail produced by the code in Section 3.2.1.

The MCMa3D code was then used to carry out a full 3D radiative transfer through this grid by propagating 1×10^6 photons through the mass density distribution in a Monte Carlo fashion with photons being emitted from the star at all angles. We used a full treatment of scattering that includes extinction due to scattering by using the distribution of hollow spheres (DHS) method from Min et al. (2005), which is analogous to Mie scattering but is more general as it can be applied to non-spherical particles. To produce images, the simulated photons were detected by a virtual camera situated such that photons would propagate from the star, through the dust, before being detected and producing an image composed of photons from all angles from the stellar disk.

We assumed that the dust particles in the tail were composed of corundum (Al_2O_3) as this was determined by van Lieshout et al. (2016) to be consistent with the observations of Kepler-1520 b (although other compositions are possible). We took the optical properties of corundum from Koike et al. (1995) and constructed the opacities by assuming irregularly shaped particles, using the DHS method. The opacity as a function of grain size, integrated over the spectrum of Kepler-1520 is shown in Fig. 2 of van Lieshout et al. (2014).

⁴ This value differs from the value given by van Werkhoven et al. (2014) of 0.0129(4) au because our value was derived by solving Kepler’s third law with an orbital period of 15.685 hours (Rappaport et al. 2012) and assuming a stellar mass of $0.704 M_\odot$ which is only approximately the value found by Huber et al. (2014) of $0.666 M_\odot$.

The virtual camera was elevated relative to the orbital plane to approximate the transit's impact parameter. This was only an approximation because there is a slight mismatch between the effective impact parameter derived for Kepler-1520 b in previous research (see Section 3.1) and the viewing elevation used here because different parts of the tail are at slightly different radial distances from the host star. Light curves were generated by rotating the virtual camera around the system to mimic the effect of having a stationary observer observing a transiting dust tail.

Examples of these simulated images are shown in Figs. 3.3 and 3.4. Figure 3.3 shows a series of images at different orbital phases from a viewing elevation of 81.52° from the pole of the orbital plane (approximating the impact parameter), while Fig. 3.4 shows an image at a single orbital phase as viewed from the pole of the orbital plane, with elevation 180° .

Images (and hence transit light curves) can be generated in different wavelengths, which allows the wavelength dependence of the transit depth to be studied. MCMMax3D is also capable of modelling polarisation, allowing us to predict the degree of polarisation, $\sqrt{Q^2 + U^2}/I$, induced by the dust in the tail.

The ray-tracing carried out by MCMMax3D is computationally very intensive and takes about 15 minutes to generate a single image at a single wavelength on a standard desktop workstation. To generate a light curve of sufficiently high temporal resolution, images for a large number of viewing angles need to be generated (e.g. 360 viewing angles for a 1° orbital phase resolution, corresponding to a temporal resolution of 157 s), so the time required to generate a full phase light curve for a single wavelength is typically 80 hours. For this reason, when simulating full light curves, we consider only the wavelengths $0.65 \mu\text{m}$ (Kepler bandpass), $0.85 \mu\text{m}$ and $2.5 \mu\text{m}$. When only the transit depth from a single viewing angle was needed, we considered the wavelengths of $0.45 \mu\text{m}$, $0.65 \mu\text{m}$, $0.85 \mu\text{m}$, $1.5 \mu\text{m}$, and $2.5 \mu\text{m}$.

3.3 Results of simulations

3.3.1 Modelling the light curve of Kepler-1520 b with a low planet mass

By keeping most of the parameters fixed (see Section 3.2.1), we were able to vary the meta-particle ejection velocity and dust tail mass in a trial-and-error way to produce a reasonable match to the observed average Kepler long cadence (LC) light curve of Kepler-1520 b (although this may not be the best match that this model can produce). The meta-particle ejection velocity set the tail's maximum extent perpendicular to the planet's orbital plane (which is proportional to its transit cross-section) and its mass determined its opacity.

To produce this tail, we used a planet mass of $8.36 \times 10^{-6} M_\oplus$ and radius $0.0204 R_\oplus$ (mass and radius #1 in Table 3.1), which is much smaller than the

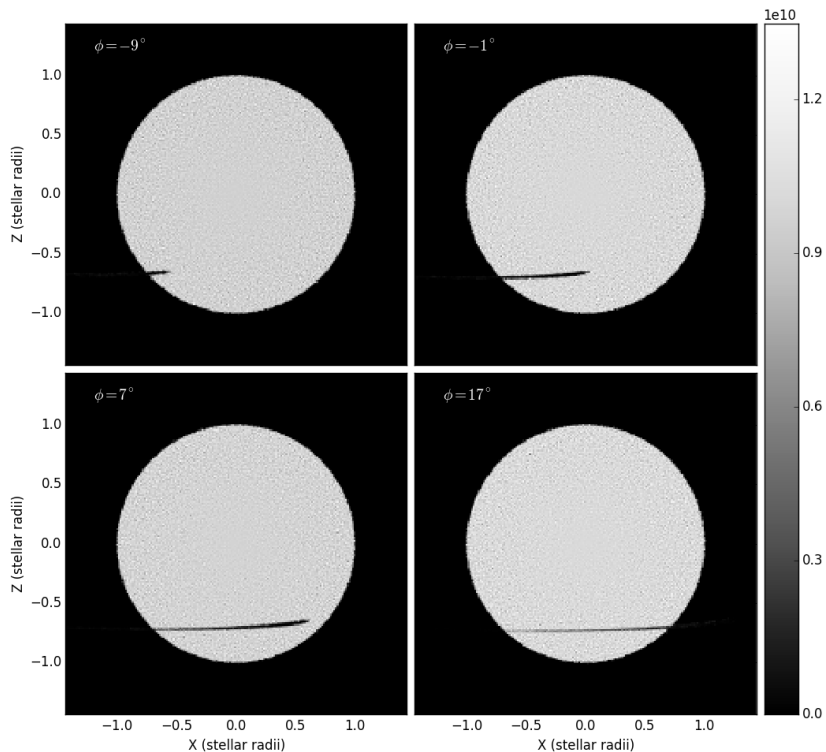


Figure 3.3: Images generated by MCMaX3D for the tail configuration presented in Section 3.3.1 at $\lambda = 650$ nm for different azimuthal viewing angles corresponding to orbital phases $\phi = -9^\circ$, -1° , 7° and 17° , with an elevation viewing angle of 81.52° as measured from the pole of the orbital plane. Integrating the flux of images such as these for different azimuthal viewing angles produces a transit light curve.

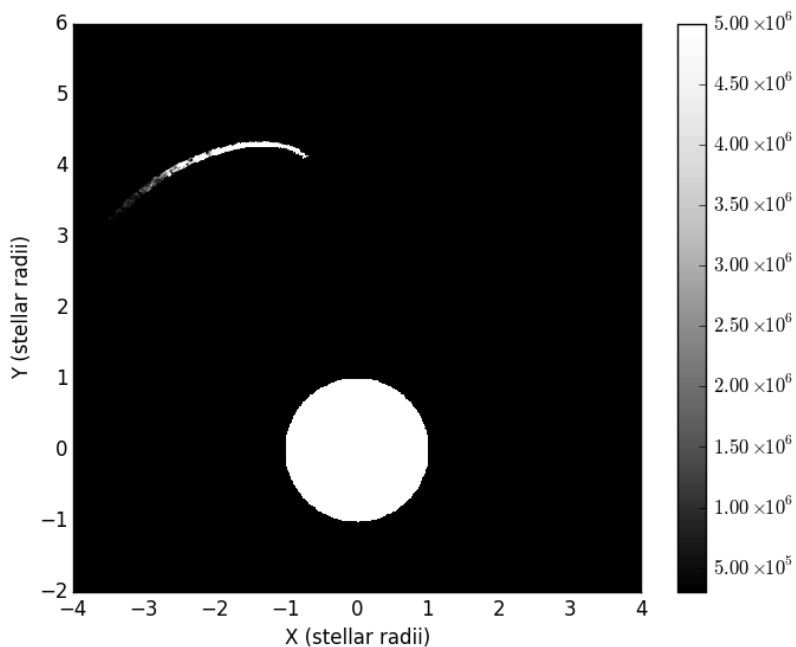


Figure 3.4: Same as Fig. 3.3, for an elevation viewing angle of 90° , looking down on the orbital plane of the planet. The tail scatters little light vertically out of the orbital plane so the dynamic range has been restricted to the fluxes from the brightest and faintest parts of the tail so the star is actually three orders of magnitude brighter than indicated by the upper limit of this colour scale.

limit of $0.7 R_{\oplus}$ determined by van Werkhoven et al. (2014) and would give a transit depth of $8 \times 10^{-6}\%$. Meta-particles were ejected with a velocity of 680 m s^{-1} (three times faster than the surface escape velocity). This resulted in a maximum tail height above the orbital plane of $1.3 \times 10^7 \text{ m}$. This tail was mostly optically thin, however, it was moderately optically thick at the head of the tail, close to the planet. For this transit cross-section, we found that a dust tail mass of $4.8 \times 10^{13} \text{ kg}$ was required to produce a relatively good match to the Kepler average long-cadence light curve. This corresponds to a mass-loss rate of $18.8 M_{\oplus} \text{ Gyr}^{-1}$.

Visualisations of this tail are shown in Figs. 3.5 and 3.6 which show the tail with meta-particles colour coded according to meta-particle radius and the square root of the density, respectively. This tail has a smooth morphology and the perihelion point where all of the meta-particles on inclined orbits cross back through the orbital plane of the planet can be clearly seen as a waist in the ‘bow-tie’ plot of Figs. 3.5 and 3.6. The points in Fig. 3.6 are colour coded according to the square root of the density (to increase the dynamic range) and clearly show a local density enhancement at this perihelion point. This enhancement has interesting implications for tails with a high optical depth, as shown in Section 3.3.2.

Even though we ejected dust meta-particles with a constant radius of $1 \mu\text{m}$, a distribution of meta-particle sizes in the tail is produced by the meta-particles sublimating. We used a constant sublimation rate which leads to the distribution in the tail as a whole being described by a power-law of the form $dN/da \propto a^{-\Gamma}$ where a is the meta-particle radius and $\Gamma = 1$. This value of Γ is different to the value used in Brogi et al. (2012) of $\Gamma = 3.5$, however, it is broadly consistent with the range of values derived by Sanchis-Ojeda et al. (2015) for the dust tail of K2-22 b of $\Gamma = 1 - 3$.

To consider the meta-particle size distribution in more detail, the distribution of meta-particle sizes as a function of phase along the tail is shown in Fig. 3.7. The top panel shows the number of meta-particles in each size bin and the bottom panel shows the probability of finding a meta-particle of a given size. This shows the details of how the number and size of meta-particles decreases with increasing angular distance away from the planet.

Therefore, the distribution of meta-particles contributing to the transit light curve changes as a function of orbital phase. Fig. 3.8 shows the average size of meta-particles crossing the stellar disk as a function of orbital phase during transit. These meta-particles make the most significant contribution to the transit light curve, however they are not the only contribution to the light curve because meta-particles not in front of the stellar disk can also contribute to the light curve by forward-scattering light. However, it is clear that even if the meta-particles are ejected with a constant initial meta-particle size, the combination of the meta-particles sublimating and having different ejection velocities will result in a dis-

tribution of meta-particle sizes as a function of orbital phase.

The transit light curve for wavelengths of 0.65, 0.85 and 2.5 μm that this tail produced are shown in Figure 3.9. We compare these simulated light curves to the Kepler LC light curve of Kepler-1520 b that resulted from the de-correlation and de-trending of 15 quarters of Kepler data by van Werkhoven et al. (2014).

The 0.65 μm light curve (Kepler bandpass) is very similar to the Kepler LC light curve, with the pre-ingress forward-scattering peak, ingress and egress slopes and transit width matching the Kepler LC data reasonably well. It can be seen that at this dust mass-loss rate, the transit light curve depends significantly on wavelength with a large difference in transit depth and shape from the visible to the near infrared. This difference may even be able to constrain the mass loss rate, as will be discussed in Section 3.4.

We computed the light curve at 0.65 μm over the entire orbital phase to search for signs of a secondary eclipse but no secondary eclipse was apparent. This is consistent with the Kepler LC observations (van Werkhoven et al. 2014).

3.3.2 Optically thick tail

To investigate the properties of a hypothetical optically thick tail, we produced a tail of dust that had 600 times more mass than the tail presented in Section 3.3.1, giving a dust mass of 1.2×10^{16} kg, or a dust mass-loss rate of $4.8 \times 10^3 M_{\oplus} \text{Gyr}^{-1}$. This planet dust mass-loss rate is unrealistically high because the planet would not survive for long enough to have a reasonable chance of being observed. However, it produces interesting light curves, so we present it here as a hypothetical illustrative example. We see four major differences when comparing its light curves shown in Fig. 3.10 to those shown in Fig. 3.9. The first difference is that the transit duration has become longer because the small meta-particles in the low density region at the end of the tail now have enough mass to make an appreciable effect on the light curve. The second difference is that the wavelength dependence in transit depth has become much less significant, while the third difference is that the pre-ingress forward-scattering feature is no longer present. The fourth difference is the ‘double dip’ transit shape which results from the tail being bow-tie shaped (bottom panel of Fig. 3.5) and optically thick. As was previously discussed by van Lieshout et al. (2016), this occurs because when the particles on inclined orbits pass through the planet’s orbital plane (the narrow part of the bow-tie), they leave gaps above and below the orbital plane, reducing the tail’s cross-section. The absorption of an optically thick tail only depends on the tail cross-section so this reduces the absorption at the mid-transit point. Therefore, if such a feature were ever observed in the light curve of a disintegrating planet, it would indicate that the tail was optically thick and that the particles were necessarily surviving for at least half of an orbit to reach this point of tail cross-section reduction.

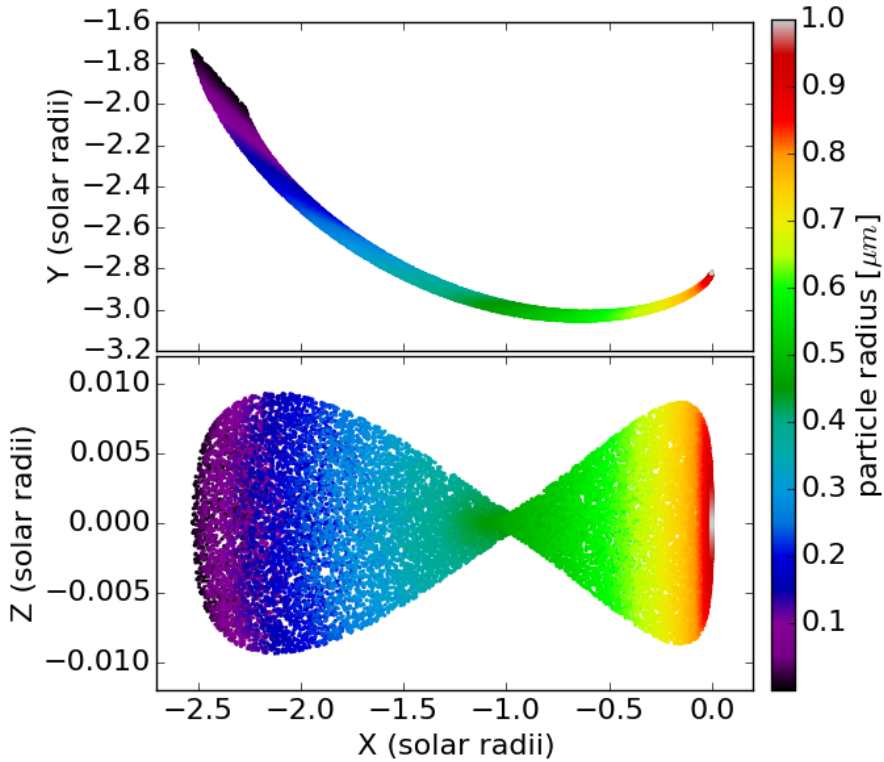


Figure 3.5: Simulated tail of corundum meta-particles viewed from above the orbital plane (top) and in the orbital plane (bottom) with meta-particles colour coded according to meta-particle radius. The top panel's axes have the same scale, however the bottom panel's vertical axis is stretched by a factor of ~ 1000 relative to the horizontal axis because the tail is much longer than it is high. These meta-particles have an initial radius of $1 \mu\text{m}$ and were ejected with a spherically symmetric distribution from a planet of mass $8.4 \times 10^{-6} M_{\oplus}$ and radius of $0.020 R_{\oplus}$ at a velocity of 3.0 times the planet's surface escape velocity (or 674 m s^{-1}). The meta-particles were tracked as they sublimated until they were removed when they reached a radius of 1 nm. The sublimation rate of the meta-particles was set so that they reached a radius of 1 nm after one planetary orbit.

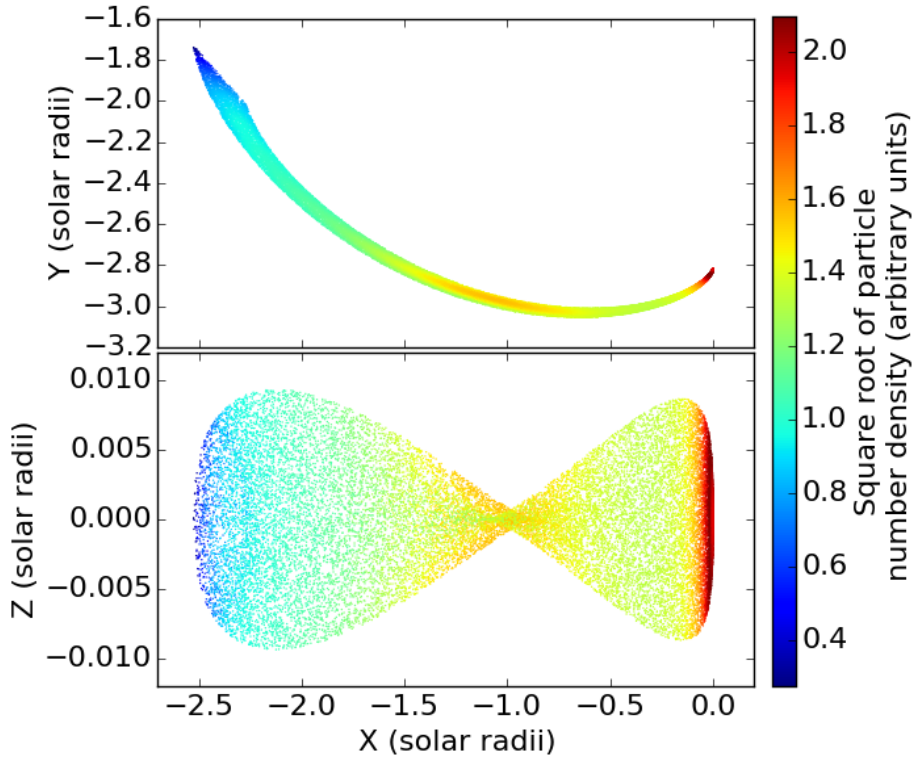


Figure 3.6: Same as Fig. 3.5 but colour coded proportionally to the square root of density to increase the dynamic range.

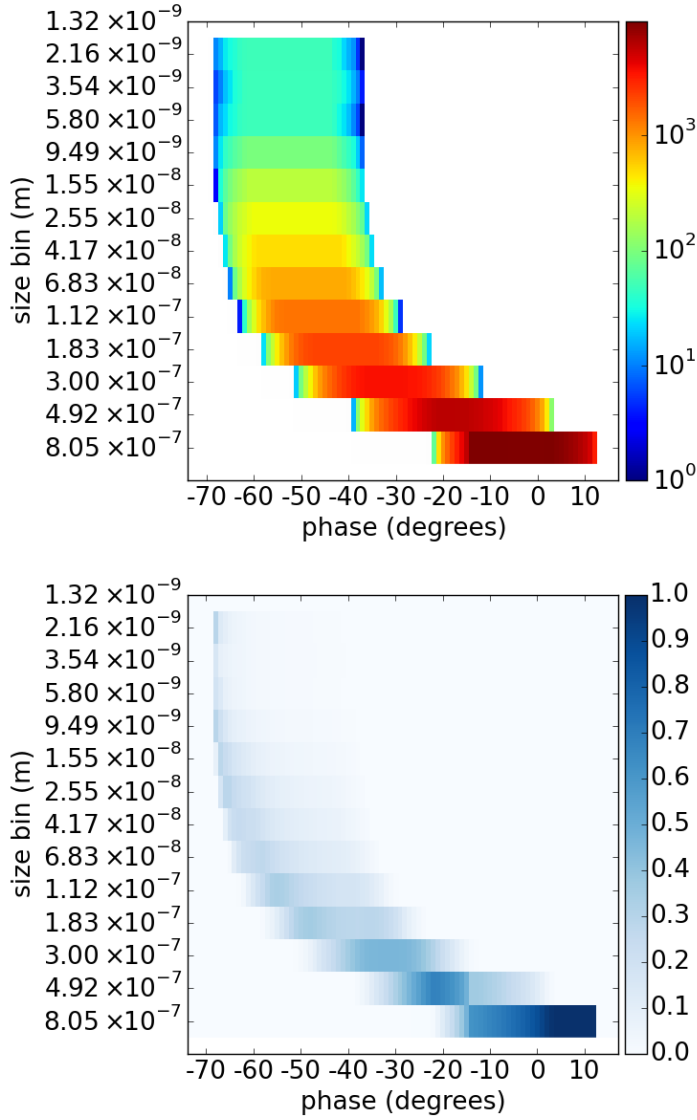


Figure 3.7: Distribution of meta-particle sizes in the tail produced by ejecting meta-particles with a spherically symmetric distribution from a planet of mass $8.4 \times 10^{-6} M_{\oplus}$ and radius of $0.020 R_{\oplus}$ at a velocity of 3.0 times the planet’s surface escape velocity (or 674 m s^{-1}). Top: Number of meta-particles in each size bin (vertical axis) as a function of angular displacement along the tail with positive phases being ahead of the planet (horizontal axis). Bottom: Same as top but instead of showing the absolute number of meta-particles, it shows the probability of finding a meta-particle within a given size bin at that angular displacement along the tail, so that the sum over all meta-particle sizes for a given angular phase (column) is one.

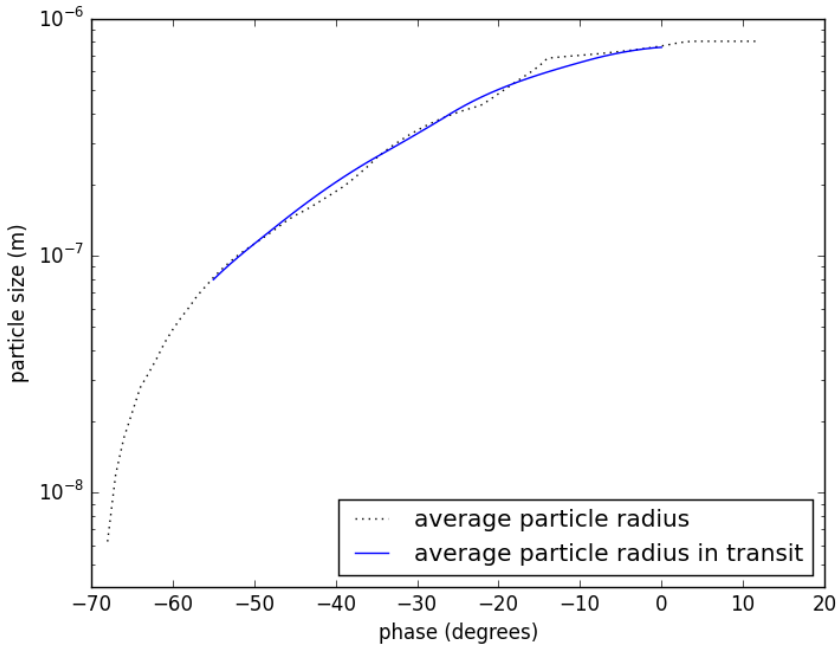


Figure 3.8: Average meta-particle size in transit for the tail produced by ejecting meta-particles with a spherically symmetric distribution from a planet of mass $8.4 \times 10^{-6} M_{\oplus}$ and radius of $0.020 R_{\oplus}$ at a velocity of 3.0 times the planet's surface escape velocity (or 674 m s^{-1}). The black dotted line shows the average meta-particle size as a function of phase in transit in intervals of 1° while the solid blue line is convolved by the angular size of Kepler-1520 as seen from Kepler-1520 b, of 26° , to show that at different times during the transit, different meta-particle sizes dominate the contribution to the light curve. This excludes the meta-particles external to the stellar disk that contribute with scattered starlight.

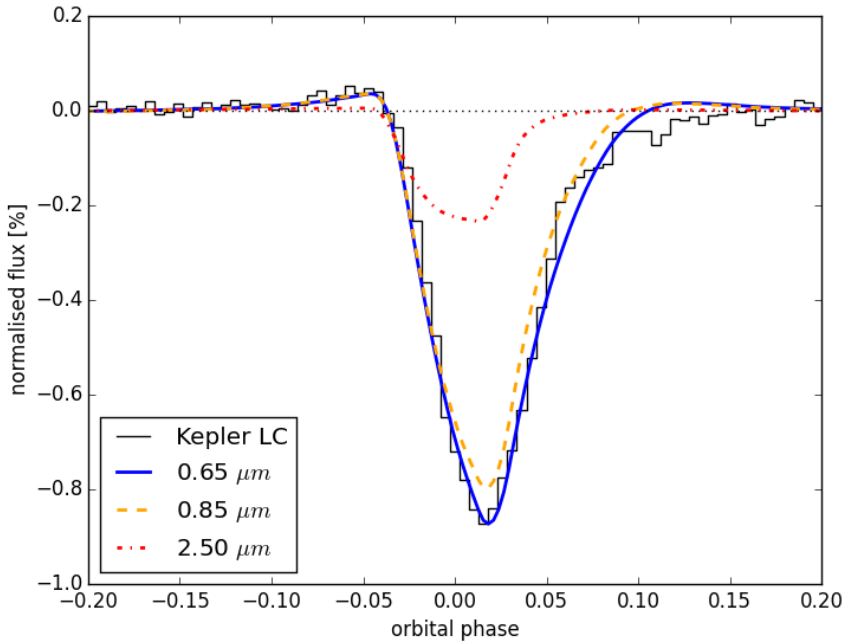


Figure 3.9: Model light curves produced by the tail shown in Fig. 3.5 at wavelengths of $0.65 \mu\text{m}$ (solid blue), $0.85 \mu\text{m}$ (dashed orange) and $2.5 \mu\text{m}$ (dot-dashed red) compared with the Kepler long-cadence light curve of Kepler-1520 b (black). The model light curves are convolved to the Kepler long-cadence of 30 minutes. To produce this light curve, meta-particles were ejected with a spherically symmetric distribution from a planet of radius $0.020 R_{\oplus}$ and mass $8.4 \times 10^{-6} M_{\oplus}$ with a velocity of 3.0 times the planet's surface escape velocity (or 674 m s^{-1}) at a mass loss rate of $18.8 M_{\oplus} \text{ Gyr}^{-1}$.

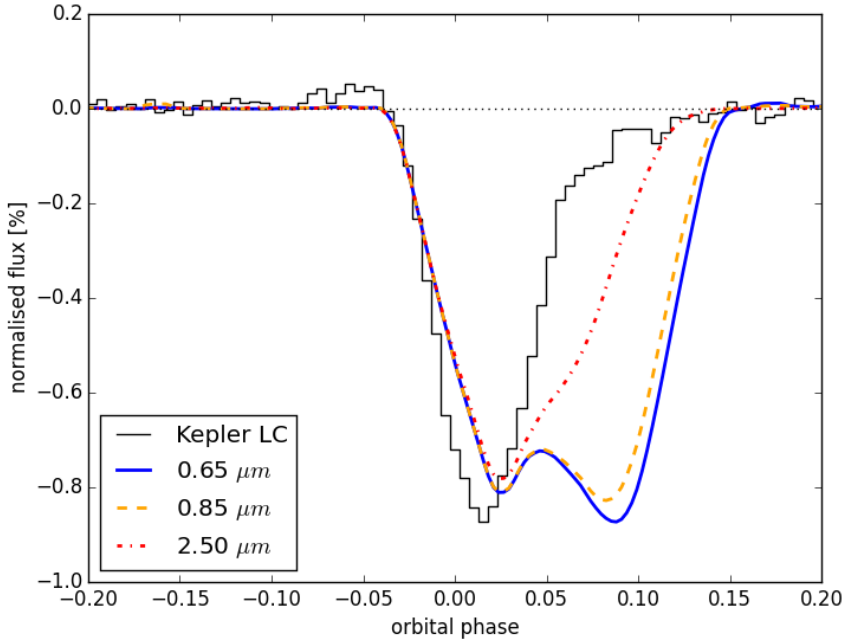


Figure 3.10: Model light curves produced by the optically thick tail described in Section 3.3.2 at wavelengths of $0.65 \mu\text{m}$ (solid blue), $0.85 \mu\text{m}$ (dashed orange) and $2.5 \mu\text{m}$ (dot-dashed red) compared with the Kepler long-cadence light curve of Kepler-1520 b (black). The model light curves are convolved to the Kepler long-cadence of 30 minutes. This tail was produced by ejecting particles with a spherically symmetric distribution from a planet of mass $8.4 \times 10^{-6} M_{\oplus}$ and radius of $0.020 R_{\oplus}$ at a velocity of 413 m s^{-1} (1.8 times the planetary surface escape velocity) and scaling its final dust mass to $1.2 \times 10^{16} \text{ kg}$, or a dust mass-loss rate of $4.8 \times 10^3 M_{\oplus} \text{ Gyr}^{-1}$ (600 times higher than the tail mass that that produced Fig. 3.9) to make it completely optically thick.

By exploiting the fact that the mid-transit depth depends linearly on maximum tail height for an optically thick tail, this transit depth was made to be comparable to the depth of the average Kepler LC light curve of Kepler-1520 b by setting the meta-particle ejection velocity to be 413 m s^{-1} (1.82 times the surface escape velocity) which resulted in a maximum tail height from the orbital plane of $7.38 \times 10^6 \text{ m}$. The relation between meta-particle ejection velocity and maximum tail height is further discussed in Section 3.5.

We checked for a secondary eclipse at $0.65 \mu\text{m}$ with this tail mass by computing the full orbit phase curve. However, as with the optically thin tail, we did not see a secondary eclipse. While this is an interesting illustrative example, this scenario is unlikely.

3.3.3 Modelling the light curve of Kepler-1520 b with a planet mass of $0.02 M_{\oplus}$

Since the planet of mass $8.36 \times 10^{-6} M_{\oplus}$ that was used in Section 3.3.1 would disintegrate too quickly, we simulated a tail using a planet mass of $0.02 M_{\oplus}$ (mass #2 in Table 3.1) and a meta-particle ejection velocity of 1.21 km s^{-1} or 0.40 times the surface escape velocity. This resulted in a maximum height from the orbital plane of $1.5 \times 10^7 \text{ m}$, which is similar to the maximum height of the tail presented in 3.3.1, however the maximum height is just an approximate comparison between these tails because they have different vertical meta-particle distributions. Ejecting the meta-particles at such a low velocity resulted in 84% of the meta-particles falling back onto the planet in ballistic trajectories before they could form a tail. To compensate for this large number of lost meta-particles, we increased the number of ejected meta-particles so that the final number of meta-particles was the same as the tail shown in Section 3.3.1. The surviving 16% of meta-particles have an interesting distribution of initial velocities which is shown in Fig. 3.11 where the upper panels show the distribution of initial velocities of all ejected meta-particles and the lower panels show the initial velocity distribution of only the meta-particles that do not collide with the planet and ultimately form a tail. The directional components are: in the direction of the planet's orbital motion (\vec{X}), directed towards the star (\vec{Y}), and directed perpendicular to orbital plane (\vec{Z}). There is a strong preference for tail forming meta-particles to have been ejected in the anti-orbital direction, the anti-stellar direction and at small angles from the planet's orbital plane.

Meta-particles that are ejected in the anti-orbital direction are more likely to avoid colliding with the planet than meta-particles that are ejected in the orbital direction because the radiation pressure and centrifugal force act to move the meta-particles radially away from the star, slowing their orbital velocity and allowing them to be overtaken by the planet. In the co-rotating reference frame, the meta-particles drift away from the stationary planet in the anti-orbital direction. Therefore meta-particles ejected in the orbital direction have to pass over the planetary surface, increasing their chances of falling back onto the planet, while meta-particles ejected in the anti-orbital direction drift away from the planet without having to pass over its surface.

Meta-particles are more likely to form a tail after being ejected in the anti-stellar direction because on that side of the planet, the radiation pressure and centrifugal forces counteracts the planet's gravity. Conversely, on the stellar side they act in the same direction as the planet's gravity to accelerate meta-particles back towards the planet. This model does not account for the possibility of the planet shielding meta-particles from the radiation pressure, however we expect that this would only make the preference slightly less pronounced because it would only

affect meta-particles that were ejected almost exactly in the anti-stellar direction.

The preference for small ejection angles from the orbital plane (\vec{Z} component close to zero) is mostly because a larger initial velocity component in the \vec{Z} direction reduces the velocity component in the anti-stellar direction. This means that meta-particles ejected with a large velocity in the \vec{Z} direction require a larger radiation acceleration to escape the planet. Furthermore, considering the co-rotating reference frame, a larger initial velocity component in the \vec{Z} direction will result in a smaller Coriolis acceleration that can potentially work with the radiation pressure and centrifugal force to help overcome the planet's gravity. Despite it being more likely that meta-particles that are ejected with a large component of their velocity in the \vec{Z} direction will collide with the planet, those that do not collide with the planet set the maximum height of the tail.

This may have interesting implications for understanding the geophysical processes occurring on the planet. It shows that if the planet were relatively massive, even if the particle ejection mechanism acts uniformly over the entire planet's surface, we would only detect the fraction of the total population that was ejected in the particular direction that can form a tail.

This tail is presented in Figs. 3.12 and 3.13 which show the tail meta-particles colour coded according to meta-particle size and local density. Despite having a maximum height that is similar to the tail presented in Sect. 3.3.1, this tail has a more rectangular shape, which would diminish the prospect of detecting the double-dip light curve feature (as in Fig. 3.10) caused by the dust density enhancement from meta-particles crossing the planet's orbital plane.

The light curve that this tail produces is shown in Fig 3.14. To make the simulated light curve have a similar depth to the Kepler average long-cadence light curve for Kepler-1520 b, we scaled the tail dust mass to 3.0×10^{14} kg, which corresponds to a dust mass-loss rate of $80 M_{\oplus} \text{ Gyr}^{-1}$, only considering the 16% of meta-particles that actually escape to form a tail. This implies a lifetime of 0.25 Myr which is also much smaller than the expected lifetimes calculated by (Perez-Becker & Chiang 2013) of 40 – 400 Myr.

3.3.4 Modelling the light curve of Kepler-1520 b with a planet mass of $0.02 M_{\oplus}$ and larger maximum height

For comparison to the simulated tail presented in Section 3.3.3 that used a planet mass of $0.02 M_{\oplus}$ with a meta-particle ejection velocity of 0.40 times the surface escape velocity, we also simulated a tail with the same planet mass but with the larger meta-particle ejection velocity of 1.034 times the surface escape velocity (or 3.13 km s^{-1}). The simulated tail is presented in Figs 3.15 and 3.16 and the resulting light curve is presented in Fig. 3.17. Since the meta-particle ejection velocity is higher than the escape velocity, most of the meta-particles can escape from the

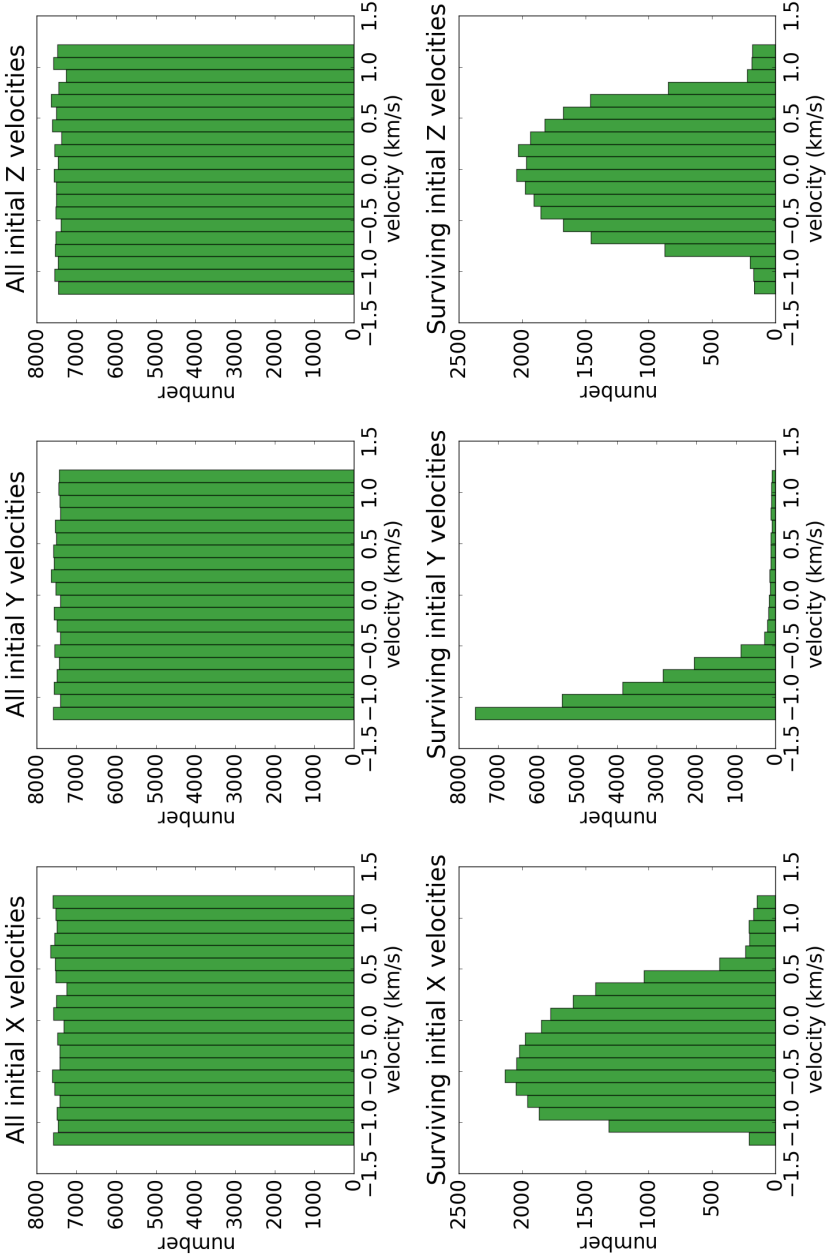


Figure 3.11: Initial velocity components of all meta-particles after being ejected from a planet of mass $0.02 M_{\oplus}$ in a continuous and spherically symmetric distribution with a velocity of 0.40 times the surface escape velocity (or 1.21 km s^{-1}) (top) and only the particles that do not collide with the planet and ultimately form a tail (bottom). The components are: in the orbital direction, \hat{X} (left), in the stellar direction, \hat{Y} (middle), and normal to the orbital plane, \hat{Z} (right).

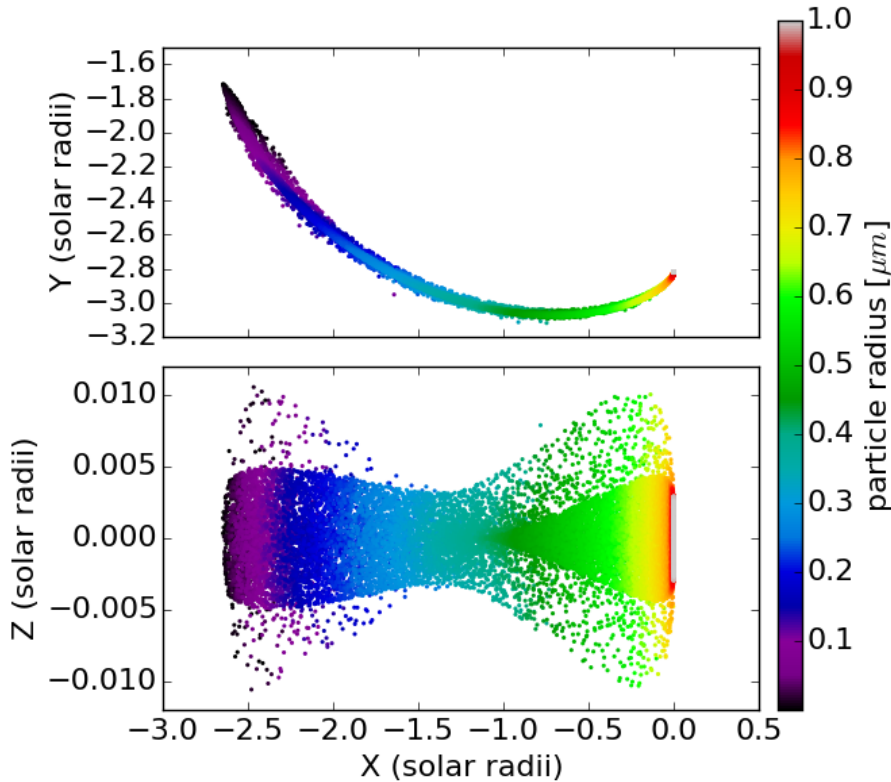


Figure 3.12: Simulated tail of corundum meta-particles viewed from above the orbital plane (top) and in the orbital plane (bottom) with meta-particles colour coded according to meta-particle radius. The top panel's axes have the same scale, however the bottom panel's vertical axis is stretched by a factor of ~ 1000 relative to the horizontal axis because the tail is much longer than it is high. These meta-particles have an initial radius of $1 \mu\text{m}$ and were ejected from a planet of mass $0.02 M_{\oplus}$ in a continuous and spherically symmetric distribution with a velocity of 0.40 times the surface escape (or 1.21 km s^{-1}). The meta-particles were tracked as they sublimated until they were removed when they reached a radius of 1 nm. The sublimation rate of the meta-particles was set so that they reached a radius of 1 nm after one planetary orbit. Although there appear to be gaps at high Z positions between individual meta-particles, the grid used for radiative transfer contains at least a few meta-particles per cell and results in a continuous distribution.

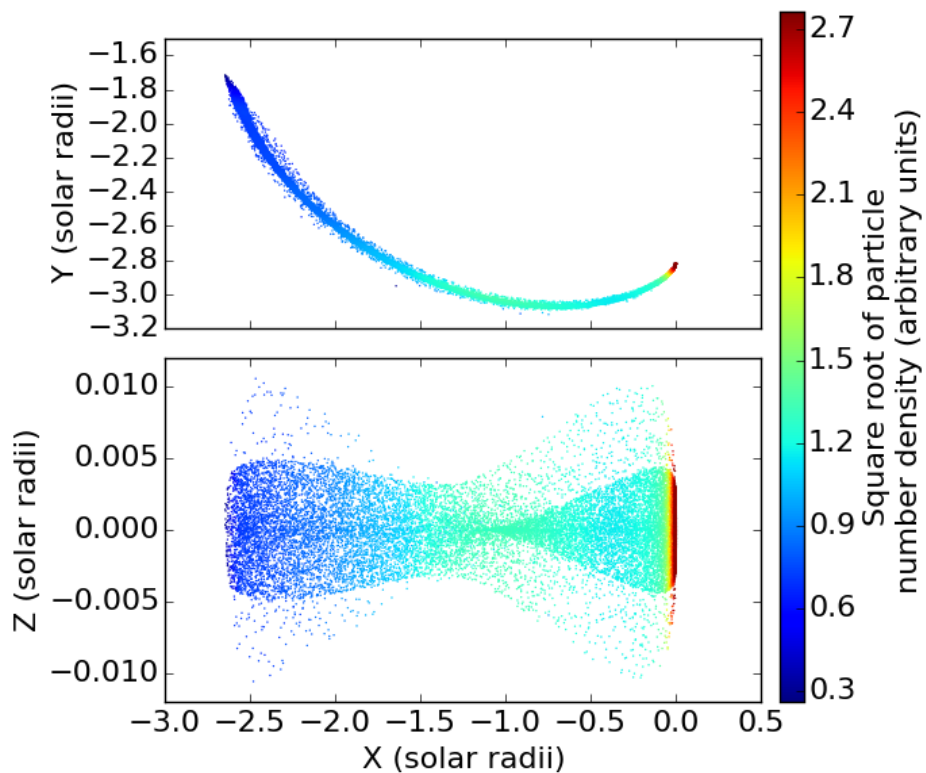


Figure 3.13: Same as Fig. 3.12, but colour coded proportionally to the square root of density to increase the dynamic range.

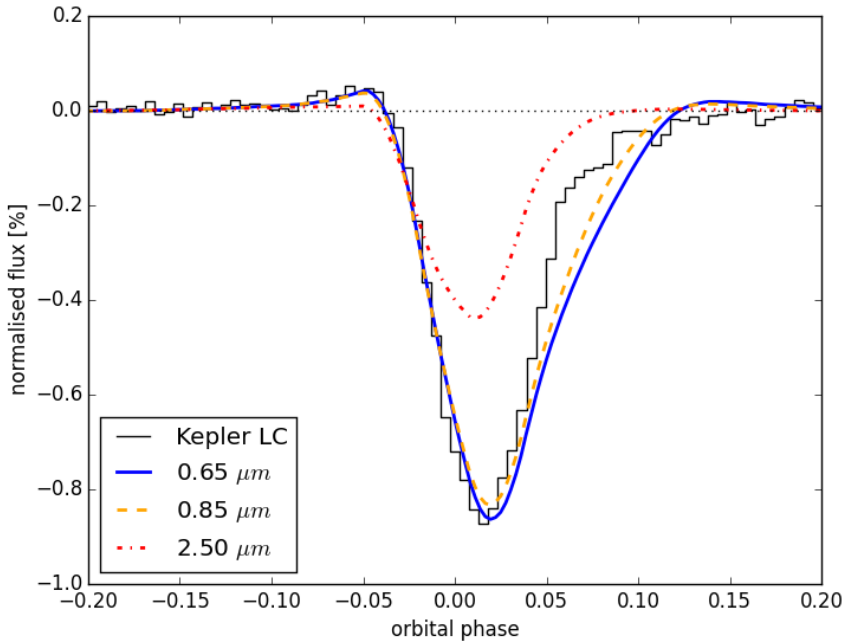


Figure 3.14: Light curve produced by the tail shown in Figs. 3.12 and 3.13 at wavelengths of $0.65 \mu\text{m}$ (solid blue), $0.85 \mu\text{m}$ (dashed orange) and $2.5 \mu\text{m}$ (dot-dashed red) compared with the Kepler long-cadence light curve of Kepler-1520 b (black). The model light curves are convolved to the Kepler long-cadence of 30 minutes. This tail was produced by a planet mass of $0.02 M_{\oplus}$ and a meta-particle ejection velocity of 0.40 times the surface escape velocity (or 1.21 km s^{-1}).

planet and form a tail. Compared to the tail in Section 3.3.3, this tail has more of a bow-tie shape, however it is less well defined than the tail presented in Section 3.3.1 due to the planet's larger gravity smearing out the point where the meta-particles' orbital trajectories cross the planet's orbital plane. After simulating the tail by calculating the meta-particle dynamics (without accounting for radiation shielding through the tail) we scaled the dust mass of the tail to make it produce the same transit depth as the average long-cadence light curve of Kepler-1520 b of 0.87%. The required tail dust mass was 1.92×10^{13} kg which corresponds to a dust mass-loss rate of $7 M_{\oplus} \text{ Gyr}^{-1}$. This dust mass-loss rate would result in the planet of mass $0.02 M_{\oplus}$ having a lifetime of 2.7 Myr which is more reasonable than the tails presented in the previous sections but still less than the 40 – 400 Myr found by Perez-Becker & Chiang (2013). However, the light curve produced by this more vertically extended tail also over-estimates the pre-ingress forward-scattering peak which prevents us from further decreasing the required dust mass-loss rate by further increasing the tail's height.

3.3.5 Behaviour of large particles

The motion of a dust particle in the tail is controlled by the ratio of the radiation pressure force to the gravitational force, β which is a quantity that only depends on radius for a given particle composition and host star spectrum (e.g. Fig. 3 of van Lieshout et al. 2014). In general, β becomes very small for large particles of radii $\gtrsim 10 \mu\text{m}$ which results in large particles not being sculpted into a long tail by the radiation pressure. Therefore, large particles tend to remain around the planet and can drift in front of the planet if they are ejected with some velocity relative to the planet.

To illustrate that this can place an upper limit on the allowed particle sizes in the tail, we simulated a tail with an initial meta-particle size of $50 \mu\text{m}$ and correspondingly increased the sublimation rate so that the meta-particles completely sublimated after one orbit. As the large meta-particles sublimate, β increases, allowing a small tail to form. The morphology of this tail is shown in Figs. 3.18 and 3.19, which show the tail meta-particles colour coded according to the meta-particle radius and square root of meta-particle density, respectively.

The transit light curve that this tail produces is shown in Fig. 3.20, in which the light curves have been scaled by a factor of 14 to compensate for the reduced cross-section of the shorter tail. When comparing to the model light curves shown in Fig. 3.9, these light curves have an earlier transit time caused by the large number of meta-particles ahead of the planet. They also have a more symmetric shape due to not having a long tail to produce the gradual increase of flux at egress. Therefore, this implies from a dust particle dynamics perspective that in order to form a tail long enough to produce an asymmetric transit light curve similar to the Kepler

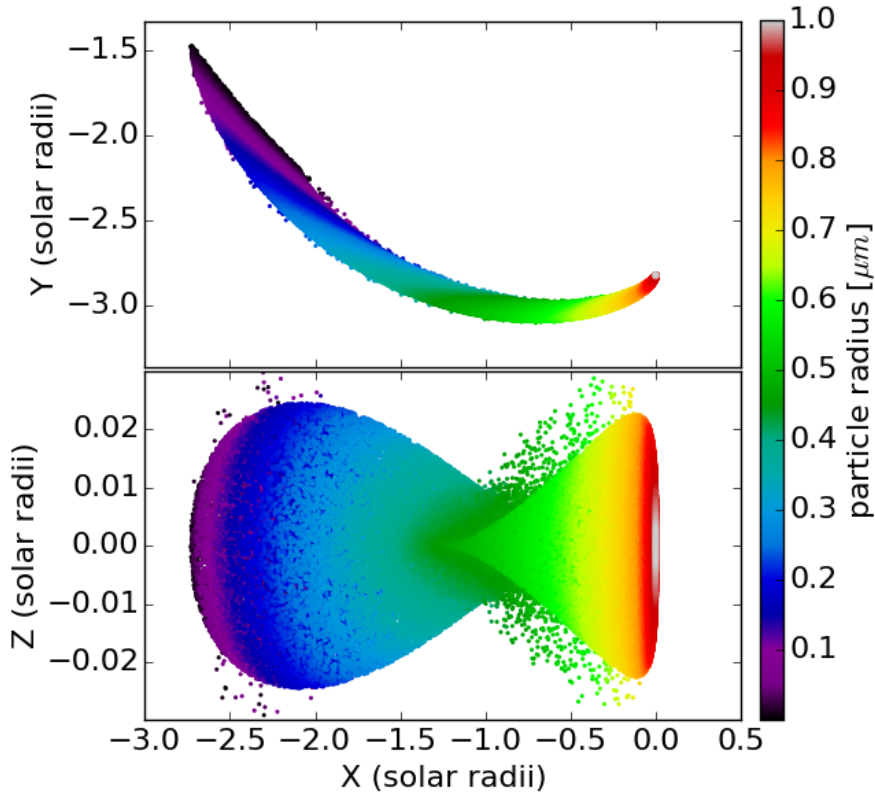


Figure 3.15: Simulated tail of corundum meta-particles viewed from above the orbital plane (top) and in the orbital plane (bottom) with meta-particles colour coded according to meta-particle radius. The top panel's axes have the same scale, however the bottom panel's vertical axis is stretched by a factor of ~ 1000 relative to the horizontal axis because the tail is much longer than it is high. These meta-particles have an initial radius of $1 \mu\text{m}$ and were ejected from a planet of mass $0.02 M_{\oplus}$ and radius $0.28 R_{\oplus}$ in a continuous and spherically symmetric distribution with a velocity of 1.034 surface escape velocities (or 3.13 km s^{-1}). The meta-particles were tracked as they sublimated until they were removed when they reached a radius of 1 nm . The sublimation rate of the meta-particles was set so that they reached a radius of 1 nm after one planetary orbit.

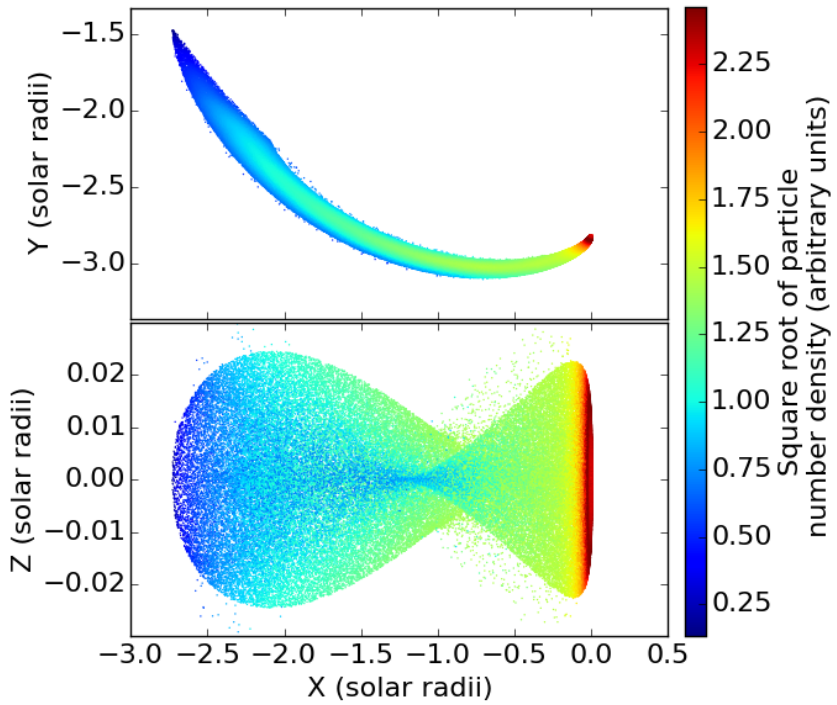


Figure 3.16: Same as Fig. 3.15, but colour coded proportionally to the square root of density to increase the dynamic range.

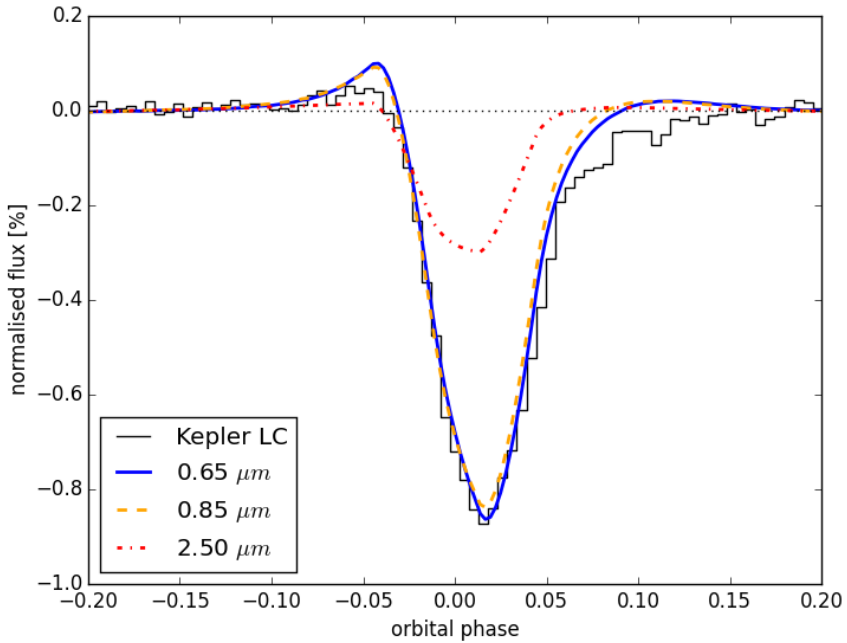


Figure 3.17: Light curve produced by the tails shown in Figs. 3.15 and 3.16 at wavelengths of $0.65 \mu\text{m}$ (solid blue), $0.85 \mu\text{m}$ (dashed orange) and $2.5 \mu\text{m}$ (dot-dashed red) compared with the Kepler long-cadence light curve of Kepler-1520 b (black). The model light curves are convolved to the Kepler long-cadence of 30 minutes. This tail was produced by a planet mass of $0.02 M_{\oplus}$ and radius $0.28 R_{\oplus}$ and an ejection velocity of 1.034 surface escape velocities (or 3.13 km s^{-1}).

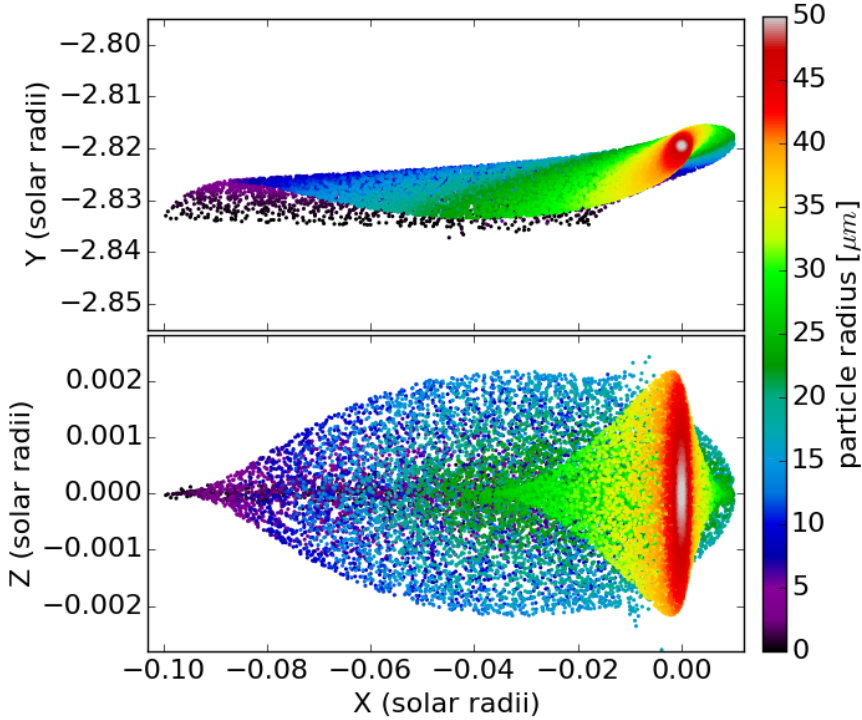


Figure 3.18: Same as Fig. 3.5, except this tail was simulated with an initial meta-particle size of $50 \mu\text{m}$ so the meta-particles do not experience a strong enough radiation pressure to push them into a long tail.

long-cadence light curve of Kepler-1520 b, the particles in the tail must have radii $\lesssim 50 \mu\text{m}$.

3.4 Wavelength dependence

To investigate how an optically thick tail can influence the wavelength dependence of the transit depth, we calculated the transit depth in several wavelengths as a function of tail dust mass (or mass-loss rate). We did this by taking the tail configuration presented in Section 3.3.1 with a planet mass of $8.35 \times 10^{-6} M_{\oplus}$, as well as a similar tail but with a reduced meta-particle ejection velocity of 272 m s^{-1} (1.2 times the surface escape velocity) and scaling the mass in the tail over three orders of magnitude. Since we were mainly interested in the transit depth and not the overall shape of the light curve, we saved time by not computing the full light curve to find the transit depth, and instead only carried out the ray-tracing for the viewing angles of phase 0 (mid-transit point) and phase 0.5 to allow the

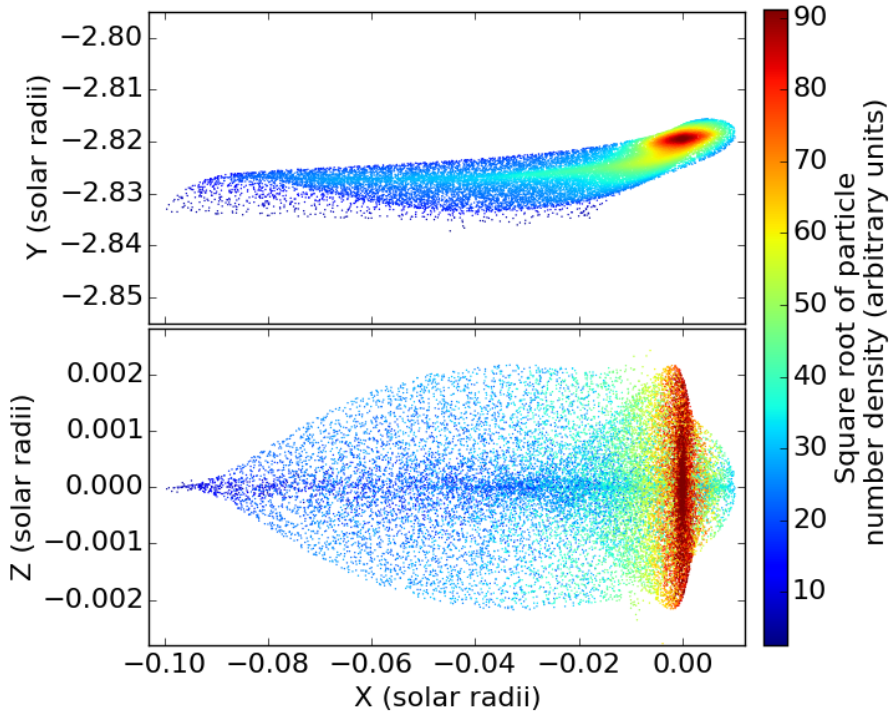


Figure 3.19: Same as Fig. 3.18, except the meta-particles are colour coded proportionally to the square root of the density in the tail.

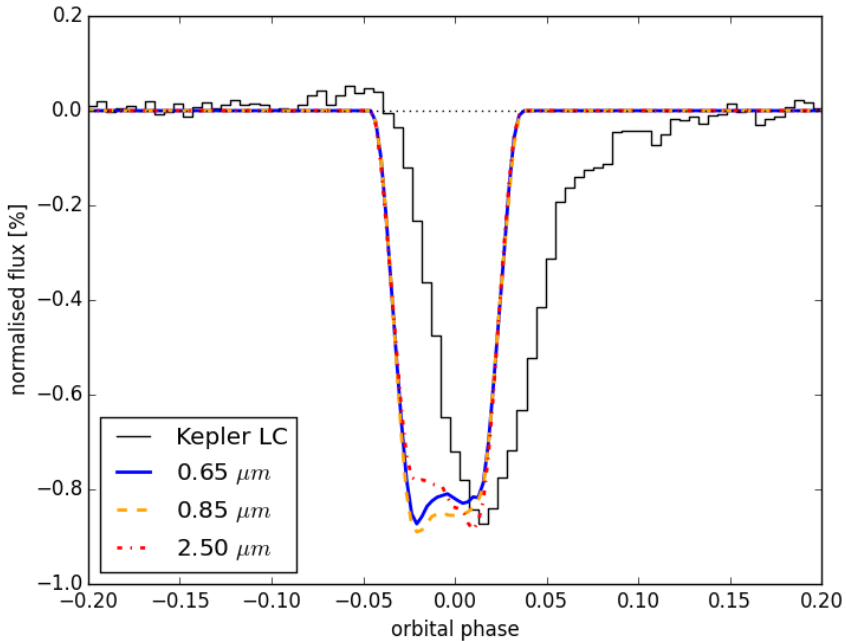


Figure 3.20: Model light curves for the tail morphology shown in Fig. 3.18 at wavelengths of $0.65\mu\text{m}$ (solid blue), $0.85\mu\text{m}$ (dashed orange) and $2.5\mu\text{m}$ (dot-dashed red) compared with the Kepler long-cadence light curve of Kepler-1520 b (black). The model light curves are convolved to the Kepler long-cadence of 30 minutes. To simulate these light curves, the dust meta-particles were ejected with an initial radius of $50\mu\text{m}$. Due to $50\mu\text{m}$ sized meta-particles not experiencing a significant radiation pressure, they do not form a long tail and drift in front of the planet. This results in a shallow transit depth and early ingress. To compensate for the reduced absorption resulting from the short tail, these light curves were scaled by a factor of 14 to make them comparable to the Kepler light curve.

normalised transit depth to be derived. For the highest tail masses, there is a small signature from the secondary eclipse spanning the orbital phase range of approximately $\phi = [0.3, -0.3]$, which may affect the absolute transit depth of the highest tail masses by $\sim 0.01\%$, however the overall trend will be unaffected.

These results are presented in Fig. 3.21 which comprises four panels. The left panels are for a meta-particle ejection velocity of 272 m s^{-1} and the right panels are for meta-particle ejection velocities of 679 m s^{-1} . The first row shows the absolute transit depth as a function of tail dust mass and indicates a trend of increasing transit depth with tail dust mass, until the tail becomes optically thick, so that there is no additional absorption from additional mass.

The lower panels present the same data as the upper panels, however all light curves were normalised to the light curve of $2.5 \mu\text{m}$ and were scaled so that every tail dust mass had the same transit depth. This re-scaling shows that the most wavelength dependence in transit depth occurs for very low-mass tails which are mostly optically thin. These tails produce very shallow transits, which will be inherently difficult to detect. Conversely, very high mass tails are optically thick and have almost no wavelength dependence in transit depth. However, we also predict a range of tail masses from approximately $2 \times 10^{12} - 2 \times 10^{14} \text{ kg}$ that have moderately deep transit depths but still exhibit a significant wavelength dependence. This suggests the tantalising possibility that if multi-wavelength transit depth observations were to be carried out to an accuracy of about 0.1% , they could be compared to models such as these and allow another way for the tail dust mass (and mass-loss rate) to be estimated. However, these results are tailored for Kepler-1520 b under the assumption that its dust composition is corundum. Therefore, performing this study for a different planet with a different composition and different stellar irradiation may give different results.

3.5 Constraints on particle ejection velocity

As mentioned in Section 3.3.2, the maximum height of an optically thick tail has a large effect on the transit depth. If the tail has sufficient mass to be optically thick, the transit will not depend on the amount of mass in the tail, and instead will only depend on the transiting cross-section of the tail, which is limited by the size of the star and depends on the maximum height and length of the tail.

The length of the tail depends on the lifetime of the particles while the maximum height of the tail depends on the projected height of the tail as seen from the observer, h , which is related to the maximum height perpendicular to the orbital plane, H , by the orbital inclination, i as $h = H \cos(i)$. H depends on the component of particle ejection velocity perpendicular to the planet's orbital plane and the mass of the planet due to the planet's gravitational attraction of the ejected

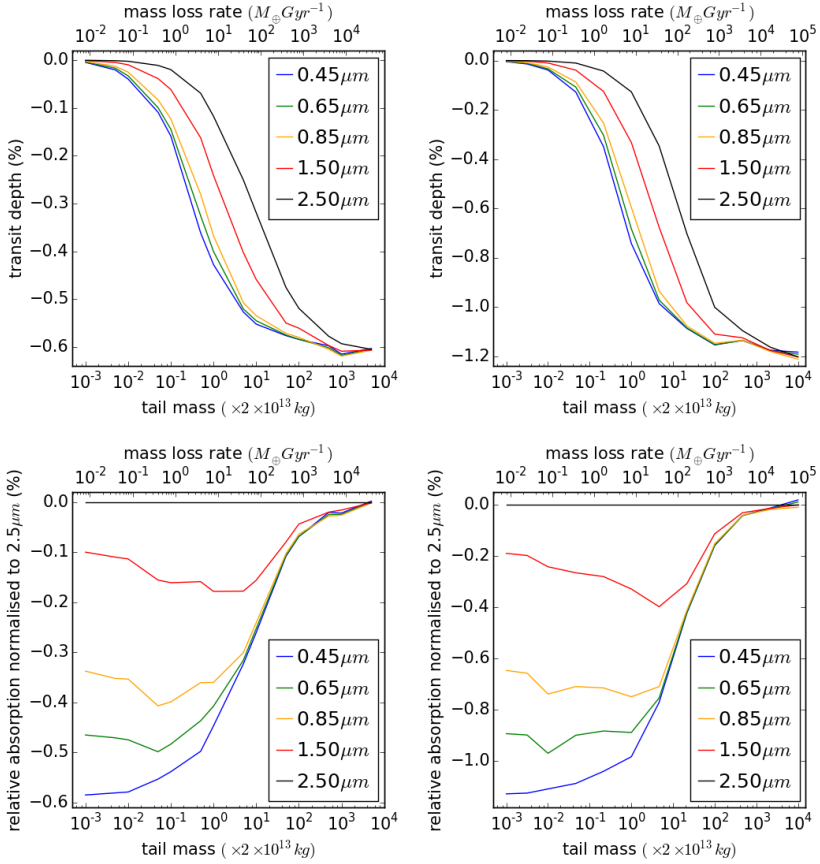


Figure 3.21: Transit depth in different wavelengths as a function of dust mass in the tail on the bottom horizontal axis or dust mass-loss rate, assuming an initial meta-particle size of $1 \mu\text{m}$ and a meta-particle density of 4.02 g cm^{-3} , corresponding to the density of corundum, on the top horizontal axis. The left panels are for a meta-particle ejection velocity of 272 m s^{-1} and the right panels are for meta-particle ejection velocities of 679 m s^{-1} . The first row shows the absolute transit depth as a function of tail mass. The lower row presents the same data as the upper panels, however all wavelength light curves were normalised to the light curve of $2.5 \mu\text{m}$ and were scaled so that every tail dust mass had the same transit depth to highlight the wavelength dependence.

particles. For a spherically symmetric particle outflow from the planet, the tail forms part of a torus with diameter, H , which results in h always being equal to H for all viewing inclinations. However, if the particle outflow were not spherically symmetric, the correcting factor $\cos(i)$ would need to be considered.

Without considering the planet's gravitational attraction, the maximum height of the tail, H , can be shown to depend linearly on the vertical component of the particle ejection velocity. This derivation is given in detail in Appendix 3.8. A particle that is ejected from a parent body will also follow a Keplerian orbit that is inclined relative to the orbit of the parent body. This inclination relative to the parent body's orbit can give a maximum height perpendicular to the orbital plane from trigonometry, which when combined with the inclination formula simplifies to a linear relationship. The planet's gravity acts to decelerate the ejected particles, but their maximum heights will still depend on their velocity perpendicular to the orbital plane, after deceleration. This can lead to an apparent non-linear relationship between particle ejection velocity and resulting maximum tail height.

3.5.1 Particle trajectories

To demonstrate this relationship we simulated tails with a fixed planet mass of $0.02 M_{\oplus}$ and ejected meta-particles with a spherically symmetric spatial distribution, while varying the ejection velocity magnitude. Since we ejected a spherically symmetric stream of meta-particles from the surface of the planet, only meta-particles that have a large component of their velocity perpendicular to the planet's orbital plane attain the maximum height. However, because of the large number of meta-particles used in these simulations, the tail is optically thick over the entire height of the tail. In reality, situations could arise where there is an optically thick central band through the tail where it is most dense and optically thin upper and lower edges where it is less dense.

We calculated the transit depths with MCMa3D as in Section 3.4. The resulting transit depths and corresponding maximum tail heights are shown in the top and bottom panels of Fig. 3.22 respectively. After simulating the tails without accounting for self-shielding affecting the radiation pressure, we scaled the resulting tail dust masses to the arbitrary large value of 1.2×10^{16} kg to ensure that the tail was optically thick so that there would be a constant correspondence between the tail's transit cross-section (set by its maximum height) and transit depth. However, such a high-mass tail may be unrealistic. We also examined the maximum tail height and transit depth profile of a mostly optically thin tail of dust mass 2×10^{13} kg. This tail produced transit depths that ranged from 0.2 – 1.2%, but it only approximately had a constant correspondence between transit depth and maximum tail height. The maximum tail height profile has an interesting and non-intuitive shape for meta-particle ejection velocities less than the planet's surface escape ve-

locity because of the interplay between the acceleration terms in Equation 3.1.

For velocities of $1.4 - 2.2 \text{ km s}^{-1}$, the meta-particles almost reach the maximum possible height allowed by inclining their orbits, as though the gravitational field of the planet were not present. This occurs because some meta-particles that are ejected in particular directions (in the co-rotating reference frame) experience sufficient Coriolis and centrifugal accelerations to increase their velocity in the direction perpendicular to the planet's gravitational acceleration enough to allow them to achieve a partial orbit around the planet. The Coriolis and centrifugal accelerations then act during the time of the partial orbit to quickly move these meta-particles radially away from the planet, rapidly decreasing the acceleration due to the planet, and allowing their orbits to incline without having to work against the planet's gravity in the direction perpendicular to the planet's orbit.

For ejection velocities greater than 3.2 km s^{-1} , the Coriolis and centrifugal accelerations can not change the increased meta-particle ejection velocities fast enough to allow them to enter partial orbits around the planet. As a result, they initially work against the gravitational field of the planet until the Coriolis and centrifugal accelerations radially move them beyond the planet's Hill sphere where the acceleration from its gravity is negligible. The time interval that the planet's gravity is relevant for can be well approximated as the time that a meta-particle with all of its initial velocity perpendicular to the planet's orbital plane (and zero velocity in the radial direction) takes to be accelerated beyond the planet's Hill sphere in the radial direction by the centrifugal acceleration. The Coriolis acceleration can be neglected for this approximation as it is roughly two orders of magnitude weaker than the centrifugal acceleration. With an initial centrifugal acceleration of 24 m s^{-2} , it takes approximately 700 seconds to cross the planet's Hill sphere. As a first order approximation, we calculated the resulting vertical velocity of a meta-particle that was decelerated by the planet's surface gravity of approximately 2 m s^{-2} for 700 seconds and found good agreement with the maximum tail height for ejection velocities higher than the surface escape velocity shown in Fig. 3.22.

In the middle region spanning approximately $2.2 - 3.2 \text{ km s}^{-1}$, the trajectories of the highest inclination meta-particles transition between the two previously described scenarios. This involves them being initially decelerated in the radial direction by the planet's gravity enough to allow them to enter a partial orbit around the planet, as was described for the $1.4 - 2.2 \text{ km s}^{-1}$ region. Interestingly, since the meta-particles decelerate until the threshold at which they can enter a partial orbit, this results in the maximum tail height being relatively constant with increasing velocity over this region. This is in contrast to what we see in the region of ejection velocities greater than 3.2 km s^{-1} where the planet's acceleration is not able to reduce the meta-particles' velocities fast enough for them to enter partial orbits.

3.5.2 Constraint from the transit depth

The deepest transit depth of Kepler-1520 b as observed by Kepler is approximately 1.4%. From Fig. 3.22 it can be seen that this transit depth results from an optically thick tail of maximum height from the orbital plane of 1×10^7 m, produced by a meta-particle ejection velocity of 1.2 km s^{-1} . Since this is for an optically thick tail that is longer than the stellar diameter, this corresponds to a lower limit on the particle ejection velocity required to produce any given transit depth. The reason for this being a lower limit can be understood by considering an idealised example of a rectangular tail of length l and height h transiting a spherical star of radius R . The transmission through this rectangular tail can be approximated as $T = (1 - f)$ where f is the fractional absorption of the tail, with $f = 1$ representing complete absorption of an optically thick tail and $f < 1$ representing the absorption of an optically thin tail.

If the tail were optically thick and much longer than the stellar diameter ($f = 1$, $l \gg 2R$), the transiting cross-section and hence transit depth will only depend on the projected tail height, which is proportional to the vertical component of the particle ejection velocity. However, this represents a situation where l and f contribute maximally to the absorption of the tail so if this were not the case and l and f decreased, h would need to increase to compensate for their reduced effect on the total absorption of the tail. Therefore, the ejection velocity inferred by assuming the tail to be long and optically thick is a lower limit. The minimum particle ejection velocity of 1.2 km s^{-1} for a planet mass of $0.02 M_{\oplus}$ is broadly consistent with the results of Perez-Becker & Chiang (2013) who found $0.02 M_{\oplus}$ to be its most likely mass and typical outflow velocities of $\sim 1 \text{ km s}^{-1}$. However, since Perez-Becker & Chiang (2013) model a gaseous outflow that gradually accelerates the escaping dust particles, their study is not directly comparable to ours, which ejects meta-particles from the surface of the planet into a vacuum.

Since the transit depth depends on the tail length, projected tail height (or particle ejection velocity) and optical depth of the dust tail, it will be challenging to disentangle their contributions and determine their individual values. However, the lower limit on the projected tail height can be used to narrow the allowed parameter space, allowing a more detailed physical interpretation of the tail to be derived.

3.5.3 Polarimetry

Starlight that reflects off disks and planets will become polarised due to being scattered by gas molecules or aerosols. Therefore, searches for polarimetric signatures can provide valuable information about the structure of disks (e.g. de Boer et al. 2017) and cometary coma (e.g. Stinson et al. 2016). Since the tails of disintegrat-

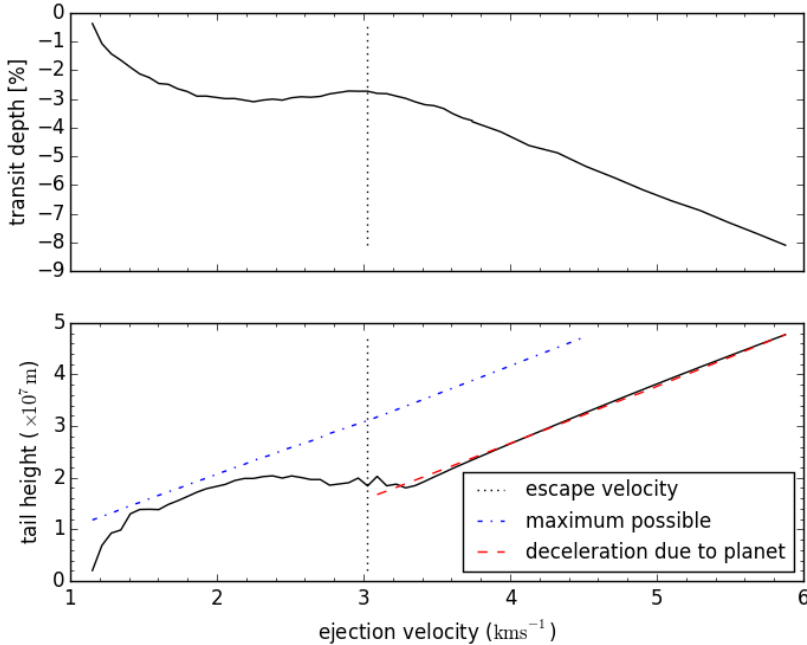


Figure 3.22: Transit depth (top) and maximum tail height (extent from the planet’s orbital plane) (bottom) as a function of meta-particle ejection velocity. The meta-particles were ejected with a spherically symmetric distribution from a planet of mass $0.02 M_{\oplus}$ and radius of $0.3 R_{\oplus}$. After the tail was simulated, the dust mass was scaled to the arbitrary large value of $1.2 \times 10^{16} \text{ kg}$ to ensure that the tail was optically thick. The vertical dotted line is the surface escape velocity. The blue dash-dotted line is the maximum height that tail meta-particles could attain if they were not decelerated in the vertical direction (perpendicular to the planet’s orbital plane) by the planet’s gravity. The dashed red line is the maximum height that tail meta-particles could attain if their vertical velocity were decelerated by the planet’s gravity for the time it takes the meta-particles to radially move beyond the planet’s Hill sphere, after being accelerated by the centrifugal acceleration (considering the co-rotating reference frame).

ing rocky exoplanets are composed of small dust particles, they would similarly be expected to induce a polarisation signal. MCMMax3D treats polarisation in its radiative transfer computations so in addition to generating images in non-polarised light, it also generates images in the Stokes Q and U parameters. This has allowed us to investigate the plausibility of observing the polarisation signal induced by the dust tails of disintegrating rocky exoplanets. For all of the simulated tails presented in this chapter, we examined the normalised polarisation intensity $\sqrt{Q^2 + U^2}/I$ (where I is the total intensity) and found that it was generally comparable to the noise from the star, but a weak signal was apparent at the 10^{-5} level.

3.6 Discussion

3.6.1 Observational implications

It is plausible that high-mass tails would be optically thick, while low-mass tails would be optically thin. This may be a partial explanation for why Croll et al. (2014), Murgas (2013) and Schlawin et al. (2016) found no evidence for a wavelength dependence in transit depth for transits of comparable depth to the Kepler light curves, while Bochinski et al. (2015) did detect a wavelength dependence in transit depth for similar transit depths. This scenario would be possible if the material were ejected with variable mass-loss rates and with variable ejection velocities, as is illustrated in Fig. 3.21 which shows, that for a given transit depth, the tail can be optically thick or thin depending on the maximum tail height. Therefore, additional multi-wavelength transit observations, including the K band ($2.2 \mu\text{m}$) in particular, would be very valuable for better constraining the models.

3.6.2 Limitations of the model

Our model takes about 15 hours to generate a dust tail, tracking 5×10^4 meta-particles and about 80 hours per wavelength to generate a corresponding full phase light curve for that tail model, so it was not feasible to carry out a rigorous parameter space study in an MCMC fashion because the model realisation times are orders of magnitude too long. However, this may be plausible in the future. Nevertheless, we caution against fitting the average light curve in great detail because of the non-linear relation between the transit light curve and the tail model: a model that explains the average light curve may not correspond to the average of models that would explain the individual transits.

The long light-curve simulation times in our model are in contrast to previously used models (see Section 3.1), which made approximations to generate transit light curves in a fast way to enable the parameter space to be explored with a

MCMC analysis. This drawback was compensated by MCMMax3D offering the advantage of being able to robustly generate transit light curves with part or all of the tail being optically thick. This enabled us to investigate whether having an optically thick tail could explain why only some multi-wavelength observations show a wavelength dependence in transit depth. Although we could not determine a best fit, by assuming reasonable values for most parameters and varying other important parameters in a trial-and-error way, we were able to generate light curves that were a reasonable match to the observed Kepler long-cadence light curve.

All of the simulated tails presented here were produced by ejecting meta-particles with an initial size of $1 \mu\text{m}$, while in reality, particles are probably ejected with a distribution of particle sizes. This may be related to the discrepancy at egress between the simulated and observed light curve shown in Fig. 3.9. Ejecting meta-particles with a distribution of initial sizes would result in the tail being radially wider because meta-particles of different radii would experience different values of β and have different trajectories, as illustrated in Fig. 3.1. However, for meta-particles of corundum in the tail of Kepler-1520 b, they have a maximum value of $\beta = 0.087$ (Fig. 3. of van Lieshout et al. 2014) which is comparable to the range of β shown in the right panel of Fig. 3.1, indicating that this only has a small effect on the tail's radial width. Therefore, we do not expect that ejecting meta-particles with a distribution of sizes would significantly change the results of our simulations. However, this will be further investigated in the forthcoming work, which includes the optical depth in the particle dynamics simulations.

3.6.3 High mass-loss rates

The mass-loss rates that we derive are orders of magnitude higher than those determined by previous studies, which are $0.1 - 1 M_{\oplus} \text{Gyr}^{-1}$ (e.g. Perez-Becker & Chiang 2013). Our higher mass-loss rates are likely related to the optically thick region at the head of the tail (near the planet) that is present in even our mostly optically thin tails. However, our model neglects extinction caused by gas that could possibly be present after being directly lost from the planet or by being produced by the sublimation of the dust in the tail. If our model were to include extinction by gas, we would not require as much extinction by dust which would allow a lower dust tail mass or mass-loss rate. However, estimating the extinction by such gas would rely on many additional assumptions and we simply caution that all of the tail dust masses presented throughout this chapter should only be considered as upper limits.

While our derived planet lifetimes appear to be too short to be consistent with the observed occurrence rate of disintegrating rocky exoplanets, this would not be the case if many of these short-lived objects were produced. However, the occurrence rates for ultra-short period planets derived by Sanchis-Ojeda et al. (2014)

suggest that longer lifetimes are required.

3.6.4 Constraints from dynamics

In Section 3.3.5 we show from a dynamical perspective that the particles must be less than approximately $50 \mu\text{m}$ to form a tail. While this is based on different physics, it is compatible with the radiative hydrodynamical simulations of Perez-Becker & Chiang (2013) which showed that large particles are less likely to be present in the tail because they are more difficult to lift out of the planet atmosphere. It is also consistent with previous observational studies, which all found constraints that varied from $0.1 - 5.6 \mu\text{m}$ (Brogi et al. 2012; Croll et al. 2014; Bochinski et al. 2015; van Lieshout et al. 2016; Schlawin et al. 2016).

In addition to the spherically symmetric meta-particle ejection distribution that was used for the tails presented in the preceding sections, we also trialled ejecting meta-particles uniformly from only the day-side and from a 30° cone directed towards the star. We find that the resulting tails had the same overall morphology as the tails produced by a spherically symmetric distribution, but that there were also some differences. The day-side only ejection distribution results in a tail that was narrower in the radial direction, while the 30° cone distribution directed towards the star resulted in a tail that was both narrower in the radial direction and the vertical direction (perpendicular to the planet's orbital plane). Both the reduced radial and vertical extents reduced the extinction from the tail so higher tail masses (or planet mass-loss rates) were required to result in the same transit depths as the tails produced from a spherically symmetric meta-particle ejection distribution.

3.6.5 Plausibility of volcanic particle ejection mechanism

The transit light curves of Kepler-1520 b show that it has transit depths that vary from approximately 0 to 1.4% and that there is no correlation between consecutive transits (van Werkhoven et al. 2014). This could likely be explained by the mass-loss rates varying significantly over time scales comparable to the planet's orbital period. The simulations of Perez-Becker & Chiang (2013) show that a limit-cycle can plausibly result in the required variation in mass-loss rates on the required time scales. The limit-cycle would form as a result of the mass-loss rate being driven by the stellar flux incident on the planetary surface after passing through the planet's atmosphere of variable opacity. The maximum mass-loss rate would occur when the atmosphere is clear of dust, which would lead to a dusty atmosphere obscuring the surface and lowering the mass-loss rate until the atmosphere clears. Rappaport et al. (2012) and Perez-Becker & Chiang (2013) also qualitatively suggest that the variability may also be partly caused by the limit-cycle being punctuated with unpredictable outbursts from volcanoes or geysers. However, it is not clear whether

this body could sustain sufficient geological activity for this to be a reasonable explanation due to its small size of $<0.7 R_{\oplus}$ (van Werkhoven et al. 2014).

The volcanic activity of Io (Lainey et al. 2009) and the geyser activity of Enceladus (Hedman et al. 2013) both result from tidal interactions with their host planets (Jupiter and Saturn, respectively) and interactions with the other moons in their systems. Kepler-1520 b is the only known planet in its system so it is unlikely that it will have tidal interactions with other bodies.

Furthermore, the models of Perez-Becker & Chiang (2013) indicate that bodies with masses $<0.1 M_{\oplus}$ can completely disintegrate in time scales of $\lesssim 10$ Gyr, and that Kepler-1520 b is likely in the final few percent of its lifetime so it has probably been at its current small orbital distance for long enough for tidal forces to have circularised its orbit. A circular orbit is also consistent with the transit timing observations. Therefore, tidal heating is probably not sufficient to drive any substantial geological activity.

The simulations of Perez-Becker & Chiang (2013) showed that small changes in the planet's atmospheric optical depth can lead to large changes in mass-loss rate. For example, if the optical depth to the surface increased from 0.1 to 0.4, the mass-loss rate would decrease by more than a factor of ten. Therefore, for a geological process to affect the variability of the transit depth, it would only need to increase the optical depth to the surface by adding more material to the planet's atmosphere, and not need to be energetic enough to eject particles completely from the planet. If geological activity were to be influencing the transit depth in this way, periods of high geological activity would result in higher optical depths and hence lower mass-loss rates. This is the opposite scenario to what would be expected for very extreme geological activity directly ejecting particles from the planet, leading to high mass-loss rates during periods of high geological activity.

Typical volcanic eruption velocities on bodies throughout the Solar System are generally consistent with the ejection velocities derived here for Kepler-1520 b. For example, typical ejection velocities on Earth are of the order of 300 m s^{-1} , while on Mars they are predicted to have been of the order of 500 m s^{-1} and on Venus they are predicted to be about 100 m s^{-1} (Wilson & Head 1983). Furthermore, on Io, due to its high level of geological activity driven by tidal interactions with Jupiter and other moons, the volcanic eruptions have been observed to be $0.5 - 1 \text{ km s}^{-1}$ (McEwen & Soderblom 1983). However, Ip (1996) found for Io that only dust particles of radii $\leq 0.01 \mu\text{m}$, that are electrically charged, can escape from the volcanic plume and form a dust coma by being accelerated by Jupiter's magnetic field. Therefore, even assuming that a volcanic eruption on Kepler-1520 b was capable of ejecting particles at these high velocities, it is not clear whether it could enable micron sized particles to escape the planet and form a dust tail.

It is not clear from a geological perspective, whether it is reasonable to expect

that volcanic outbursts could occur on a body as small as Kepler-1520 b. However, based solely on the lower limit on particle ejection velocity for Kepler-1520 b that we derived being comparable to the ejection velocities from solar system volcanoes, it could be plausible

3.7 Summary

We have developed a new 3D model of the dust tails of disintegrating rocky exoplanets that ejects sublimating meta-particles from the planet surface to build-up a dust tail, instead of assuming a tail density profile like previous 1D and 2D models. We generated transit light curves of our simulated tails using the Monte-Carlo radiative transfer code MCMaX3D (Min et al. 2009), which accounts for scattering and absorption in a robust way, allowing us to generate transit light curves for optically thick tails. We used this model to investigate how the optical thickness and extent perpendicular to the planet’s orbital plane (height) of a general dust tail can affect the observed wavelength dependence and depth of transit light curves.

We show that there is a decreasing wavelength dependence in transit depth as a function of tail optical depth, potentially explaining why only some multi-wavelength transit observations show a wavelength dependence. We also find that if the tail is optically thick, the transit depth is not indicative of the amount of mass in the tail, and only depends on the transiting cross-section of the tail.

Furthermore, we derive that the maximum tail height depends linearly on the vertical (perpendicular to the orbital plane of the planet) component of the particle ejection velocity and derived a lower limit on the particle ejection velocity required to produce a given transit depth. By applying this to the maximum transit depth of Kepler-1520 b of 1.4%, we find the required minimum particle ejection velocity to be approximately 1.2 km s^{-1} . We also show from a dynamical perspective that for low ejection velocities, only particles that are ejected in particular directions can escape from the planet and form a tail, and that the particles in the tail must be of radius $\lesssim 50 \mu\text{m}$.

To fit the average transit depth of Kepler-1520 b of 0.87%, we derived dust mass-loss rates of $7 - 80 M_{\oplus} \text{ Gyr}^{-1}$ which are approximately 10 – 100 times larger than those found by previous studies. Assuming a likely planet mass of $0.02 M_{\oplus}$, our dust mass-loss rates imply a planet lifetime up to approximately 3 Myr. It is unlikely that several objects with such relatively short lifetimes would have been observed so our derived dust mass-loss rates are unrealistic. The cause of our high dust mass-loss rates is not completely understood but it is likely related to our consideration of optically thick tails that can ‘hide’ mass, while previous studies only considered optically thin tails. We also did not consider the potential extinction from gas that may be lost from the planet or produced by the sublimation of

dust in the tail. If it were considered, we may require less dust to produce the required extinction, so our high dust mass-loss rates should only be considered as upper limits. While our large mass-loss rates indicate that more work is required, we believe that these results may help to explain why only some transit observations of Kepler-1520 b show a wavelength dependence and that our constraints on particle ejection velocity give us a more accurate physical interpretation of this intriguing object.

3.8 Appendix: Derivation of linear relationship between maximum tail height and vertical velocity

If a particle is ejected from a parent body that is on a Keplerian orbit, the ejected particle will follow a Keplerian orbit that is inclined relative to the orbit of the parent body. This inclination, i , is given by (e.g. Fulle 1989)

$$\sin(i) = \frac{v_z}{\sqrt{v_\theta^2 + v_z^2}}, \quad (3.2)$$

where v_z is the component of the particle's velocity perpendicular to the orbital plane of the parent body and v_θ is the component of the particle's velocity in the direction of the parent body's orbital velocity. For particles ejected in the direction of the parent body's orbital angular momentum vector (i.e. out of the parent body's north pole), the particle's ejection velocity is equal to v_z and v_θ is equal to the parent body's orbital velocity.

If the maximum height of the tail from its lowest to highest particle is H , then from trigonometry the maximum height above the orbital plane, $H/2$, that the particles can reach on an orbit with inclination i relative to the parent body's orbital plane is

$$\frac{H}{2} = d \tan(i), \quad (3.3)$$

where d is the radial distance to the particle, projected onto the ejecting body's orbital plane.

Substituting equation 3.2 into 3.3 gives

$$\frac{H}{2} = d \tan \left(\sin^{-1} \left(\frac{v_z}{\sqrt{v_\theta^2 + v_z^2}} \right) \right), \quad (3.4)$$

which can be simplified by using the identity

$$\tan(\sin^{-1}(x)) = \frac{x}{\sqrt{1-x^2}} \quad (3.5)$$

where $x = \frac{v_z}{\sqrt{v_\theta^2 + v_z^2}}$ to give

$$H = \frac{2d}{v_\theta} v_z, \quad (3.6)$$

which shows that H is a linear function of v_z .

Furthermore, if the orbital plane is inclined with an angle θ relative to the observer, the projected height h will be related to H according to $h = H \cos(\theta)$. However, if the particle outflow from the planet is spherically symmetric, the tail will approximate part of a torus of diameter, H , which will have the same apparent height for all viewing inclinations, i .

Acknowledgements

A. R. R.-H. is grateful to the Planetary and Exoplanetary Science (PEPSci) programme of the Netherlands Organisation for Scientific Research (NWO) for support. I. A. G. S. acknowledges support from an NWO VICI grant (639.043.107). This work has been supported by the DISCSIM project, grant agreement 341137 funded by the European Research Council under ERC-2013-ADG. We thank the anonymous referees for their constructive comments.

Bibliography

- Alonso, R., Rappaport, S., Deeg, H. J., & Palle, E. 2016, *A&A*, 589, L6
- Bochinski, J. J., Haswell, C. A., Marsh, T. R., Dhillon, V. S., & Littlefair, S. P. 2015, *ApJ*, 800, L21
- Bourrier, V. & Lecavelier des Etangs, A. 2013, *A&A*, 557, A124
- Bourrier, V., Lecavelier des Etangs, A., Dupuy, H., et al. 2013, *A&A*, 551, A63
- Bourrier, V., Lecavelier des Etangs, A., & Vidal-Madjar, A. 2014, *A&A*, 565, A105
- Broggi, M., Keller, C. U., de Juan Ovelar, M., et al. 2012, *A&A*, 545, L5
- Budaj, J. 2013, *A&A*, 557, A72
- Burns, J. A., Lamy, P. L., & Soter, S. 1979, *Icarus*, 40, 1
- Croll, B., Rappaport, S., DeVore, J., et al. 2014, *ApJ*, 786, 100
- de Boer, J., Girard, J. H., Canovas, H., et al. 2017, *MNRAS*, 466, L7
- Ehrenreich, D., Bourrier, V., Bonfils, X., et al. 2012, *A&A*, 547, A18
- Ehrenreich, D., Bourrier, V., Wheatley, P. J., et al. 2015, *Nature*, 522, 459
- Ekenbäck, A., Holmström, M., Wurz, P., et al. 2010, *ApJ*, 709, 670
- Fulle, M. 1989, *A&A*, 217, 283
- Hedman, M. M., Gosmeyer, C. M., Nicholson, P. D., et al. 2013, *Nature*, 500, 182
- Holmström, M., Ekenbäck, A., Selsis, F., et al. 2008, *Nature*, 451, 970
- Huber, D., Silva Aguirre, V., Matthews, J. M., et al. 2014, *ApJS*, 211, 2
- Ip, W. H. 1996, *Geophys. Res. Lett.*, 23, 3671
- Koike, C., Kaito, C., Yamamoto, T., et al. 1995, *Icarus*, 114, 203
- Lainey, V., Arlot, J.-E., Karatekin, Ö., & van Hoolst, T. 2009, *Nature*, 459, 957
- McEwen, A. S. & Soderblom, L. A. 1983, *Icarus*, 55, 191
- Min, M., Dullemond, C. P., Dominik, C., de Koter, A., & Hovenier, J. W. 2009, *A&A*, 497, 155
- Min, M., Hovenier, J. W., & de Koter, A. 2005, *A&A*, 432, 909
- Murgas, F. 2013, PhD thesis, Departamento de astrofísica, unisersidad de La Laguna

- Perez-Becker, D. & Chiang, E. 2013, MNRAS, 433, 2294
- Rappaport, S., Barclay, T., DeVore, J., et al. 2014, ApJ, 784, 40
- Rappaport, S., Levine, A., Chiang, E., et al. 2012, ApJ, 752, 1
- Sanchis-Ojeda, R., Rappaport, S., Pallè, E., et al. 2015, ApJ, 812, 112
- Sanchis-Ojeda, R., Rappaport, S., Winn, J. N., et al. 2014, ApJ, 787, 47
- Schlawin, E., Herter, T., Zhao, M., Teske, J. K., & Chen, H. 2016, ApJ, 826, 156
- Stinson, A., Bagnulo, S., Tozzi, G. P., et al. 2016, A&A, 594, A110
- van Lieshout, R., Min, M., & Dominik, C. 2014, A&A, 572, A76
- van Lieshout, R., Min, M., Dominik, C., et al. 2016, A&A, 596, A32
- van Werkhoven, T. I. M., Brogi, M., Snellen, I. A. G., & Keller, C. U. 2014, A&A, 561, A3
- Vanderburg, A., Johnson, J. A., Rappaport, S., et al. 2015, Nature, 526, 546
- Vidal-Madjar, A., Lecavelier des Etangs, A., Désert, J.-M., et al. 2003, Nature, 422, 143
- Wilson, L. & Head, J. W. 1983, Nature, 302, 663

4 | Self-shielding in dust tails of disintegrating rocky exoplanets

Context. Chapter 3 presents a new 3D model to simulate the dust-tails and transit light curves of disintegrating rocky exoplanets. The model combines a code to calculate the dynamics of dust particles and a radiative transfer code (MCMax3D) to produce transit light curves for the simulated tails. While the model correctly treats opacity both in the optically thick and thin regimes for the light curve calculations, the radiation pressure is calculated correctly only in the optically thin case. The model therefore neglects self-shielding which can affect the dust particle dynamics and the resulting tail morphology.

Aims. To make the model fully self-consistent, we aim to incorporate self-shielding and investigate how it affects the morphology and transit light curves of dust tails from disintegrating rocky exoplanets.

Methods. We extend the model to account for self-shielding in the dynamics of dust-particles by calculating optical depths to each particle on a spherical 3D grid using the Planck mean opacity. Shielded particles receive a reduced stellar flux, which decreases both the radiation pressure and the sublimation rate that they experience.

Results. We show that, self-shielding can have a strong influence on the dynamics and morphology of dust tails and their corresponding transit light curves. In the particular case of Kepler-1520 b, the average transit depth can be reproduced with a mass-loss rate of $3 - 3.9 M_{\oplus} \text{ Gyr}^{-1}$, which is lower than the value derived in Chapter 3 for non-self-shielding tails because the particles do not sublimate as quickly. However, this reduced sublimation rate makes it more likely that particles survive for more than one orbit, violating the observed lack of correlation between transits (van Werkhoven et al. 2014), except if the composition of the dust particles is such that they have a particularly high sublimation rate. We also show that the outbursts of mass-loss can be much shorter than an orbital period and that mass-loss rates $\gtrsim 10 M_{\oplus} \text{ Gyr}^{-1}$ only produce long tails if they are continuous for several orbits due to the strong self-shielding slowing the drift rate of particles away from the planet. Such tails produce correlated increasing transit depths, providing an observational signature that may be exploited in the era of TESS.

4.1 Introduction

The Kepler Space Telescope has revealed a class of small, short-period rocky exoplanets that have a ‘comet-like’ dust tail that produces variable and asymmetric transit light curves of which Kepler 1520 b (formerly known as KIC 12557548 b) is the archetype (Rappaport et al. 2012, 2014; Sanchis-Ojeda et al. 2015; Vanderburg et al. 2015). Studying the properties of this dust provides unique insights into the composition of the parent planet. By fitting the average transit shape with dust tail models, including brightening from forward scattering, parameters such as the particle size, particle composition and mass-loss rate have been constrained (Rappaport et al. 2012, 2014; Brogi et al. 2012; Budaj 2013; van Lieshout et al. 2014; Sanchis-Ojeda et al. 2015; van Lieshout et al. 2016), which can be further investigated using spectroscopic transit observations (e.g. Croll et al. 2014; Murgas 2013; Bochinski et al. 2015; Alonso et al. 2016).

Since a large amount of dust is released from a small planet, the dust is bound to be optically thick close to the planet. Previous modeling efforts confirm this (van Lieshout et al. 2016). We therefore embarked on an effort to develop a new model that simulates optically thick dust tails for the first time. A two-step approach was implemented in our earlier model (Chapter 3). First, a dust tail was built up by ejecting particles in 3D from the surface of a planet to calculate their subsequent dynamics under the influence of the star’s radiation pressure and the planet’s gravity assuming optically thin conditions. Subsequently, the 3D dust-mass distribution in the tail was gradually scaled up to make them partially or completely optically thick. Using this model, it was found that increasing the optical depth of a dust tail makes the transit depth more achromatic, and a constraint was derived on the particle ejection velocity for a given planet mass under the assumption that the particles are not accelerated by gas after they leave the planet. In Chapter 3, planet mass-loss rates for Kepler-1520 b were derived which are 10 – 100 times higher than those inferred by previous studies that used fully optically thin tail models. This is due to the fact that optically thick tails allow some mass to be ‘hidden’, which does not contribute to the transit depth.

The approach taken in Chapter 3 is, however, not completely self-consistent. In the case that a dust tail is (partially) optically thick, some fraction of the dust particles will be shielded from stellar radiation, slowing down their sublimation and decreasing the radiation pressure. This may affect the overall morphology (length and shape) of the dust tail. This motivates the work presented here, which extends the model in Chapter 3 to account for self-shielding when simulating the dust particle dynamics and evolution for the first time. We note that self-shielding of gas only has been implemented in a model by Bourrier et al. (2014) for a different astrophysical phenomenon, the comet-like gas-tails resulting from atmospheric escape of the hot Jupiters HD 209458 b and HD 189733 b.

This chapter is structured as follows: Section 4.2 explains the model, Section 4.3 presents and discusses the results of the simulations and Section 4.4 concludes.

4.2 Method: The model

The original model that forms the basis of this study was fully described in Chapter 3. In brief, it builds up a dust tail by ejecting meta-particles, which individually represent a large number of dust particles, from the surface of a small rocky exoplanet. After the meta-particles are ejected, they move under the influence of the planet's gravitational force, the stellar radiation pressure, and the stellar gravitational force. The ratio of the latter two forces, β , is independent of the distance from the star, and only depends on the stellar luminosity and the dust scattering properties, which are set by the particle composition, radius and shape (e.g. Burns et al. 1979).

Values of β were computed as in van Lieshout et al. (2014) by assuming a composition of corundum (Al_2O_3). This was found by van Lieshout et al. (2016) to be consistent with the observations, although other compositions such as iron-rich silicates are also possible. Our meta-particles become smaller with time due to sublimation, so we allow the value of β to change consistently with the change in particle radius. Transit light curves are subsequently generated for these simulated tails by using the radiative transfer code MCMaX3D¹ (Min et al. 2009) which calculates the wavelength-dependent light curves for optically thick dust tails.

In the original study of Chapter 3, dust particle dynamics were calculated using an optically thin approximation, meaning that each particle receives the full amount of radiation pressure. Total opacity calculations, including those in the optically thick regime, were achieved by scaling up the mass distribution only after the particle dynamics were determined. However, this is not a fully self-consistent approach, since optical depth effects can shield parts of the dust particle ensemble from stellar radiation. This self-shielding influences both the sublimation rate and the particle trajectories, and is included in the model presented here.

All of our self-shielding simulations use the input parameters shown in Table 3.1, with option #2 for the planet mass and radius. However, optical depths are calculated on a higher resolution grid, defined by the cell boundaries given in Table 4.1. As with Chapter 3, these boundaries were set such that the planet is located on an intersection of grid lines so that particles released from different sides of the planet fall into different grid cells. The optical depth was calculated for each grid

¹<http://www.michielmin.nl/codes/mcmax3D/>

position according to

$$\tau(r, \theta, \phi) = A \sum_{r=0}^R \sum_{a=a_{min}}^{a_{max}} \kappa(a) \rho(r, \theta, \phi, a) dr(\theta) \quad (4.1)$$

where a is the particle radius, r is the radial distance from the star, θ is the elevation angle relative to the orbital plane, ϕ is the azimuthal angle, $\kappa(a)$ is the particle size dependent Planck mean opacity², $\rho(r, \theta, \phi, a)$ is the mass density within a particular size bin, $dr(\theta)$ is the radial extent of the cell, which varies as a function of elevation relative to the planet's orbital plane, and A is the scaling factor to normalize the optical depths to those of MCM3D. This was determined by comparing the optical depths calculated for our tail dynamics by those of MCM3D. In the simulations for Kepler-1520 b, we set the $\kappa(a)$ dependence as for corundum particles in the appropriate radiation field set by the effective temperature of the host star. The optical properties of corundum were taken from Koike et al. (1995). The opacities were constructed assuming irregularly shaped particles computed using the distribution of hollow spheres (DHS) method from Min et al. (2005).

Subsequently, for each 3D grid position, the fractional flux \mathfrak{F} that is transmitted through the radial column in the tail equals $e^{-\tau(r)}$ (ignoring the scattered flux field). This allows β to be modified to

$$\beta' = \mathfrak{F} \frac{F_{rad\ star}}{F_{grav\ star}} = \mathfrak{F}\beta. \quad (4.2)$$

We also account for the attenuated flux driving a reduced meta-particle sublimation rate, \dot{a}' , according to

$$\dot{a}' = \mathfrak{F}\dot{a} \quad (4.3)$$

where \dot{a} is the assumed particle sublimation rate (change in radius per second) for particles that receive the unattenuated stellar flux.

As in Chapter 3, a value of \dot{a} is assumed such that an unshielded particle that is ejected with a radius of 1 μm will have completely sublimated after exactly one orbital period. This is only a first-order approximation because in reality, the particle sublimation rate will depend on the particle size and temperature. However, for this work our focus was on investigating a general, optically thick tail, so our only requirements on sublimation rate were that it produced a tail of reasonable length and that unshielded meta-particles did not survive for longer than one orbit (since there is no correlation between consecutive transit depths (van Werkhoven et al. 2014)), making our simple approximation reasonable. The model was implemented as in Section 3.2.1, except that β' replaced β in Equation 3.1.

²The mean opacity, weighted according to the host stars's normalized Planck black body radiation energy density distribution.

Table 4.1: Radiative transfer grid parameters for the self-shielding simulations.

Parameter	Value
Radial grid	
Inner radius	0.0130 au
Outer radius	0.0152 au
Bin size	1.65×10^6
Elevation grid ($0^\circ - 180^\circ$)	
Lower elevation	89.58° ⁽¹⁾
Upper elevation	90.42° ⁽²⁾
Bin size	0.0105°
Azimuthal grid ($0^\circ - 360^\circ$)	
Bin size	0.5°

⁽¹⁾ With an additional large bin containing $0^\circ - 89.58^\circ$.

⁽²⁾ With an additional large bin containing $90.42^\circ - 180^\circ$.

For a completely optically thin tail, self-shielding should have a negligible effect on the particle dynamics and tail morphology. To confirm that this was indeed the case with our new model, we compared tails that were simulated both with and without self-shielding at different mass-loss rates. For these simulations we chose to eject meta-particles with an initial radius of $1 \mu\text{m}$ in a continuous and spherically symmetric distribution with a velocity of 3.13 km s^{-1} (1.03 times the surface escape velocity) from a planet of mass $0.02 M_\oplus$. We assumed a planet bulk density equal to that of Mercury (5427 kg m^{-3}), giving a radius of $0.28 R_\oplus$. We found that accounting for self-shielding produced no significant effect in the tail for mass-loss rates $\lesssim 0.1 M_\oplus \text{ Gyr}^{-1}$, as shown by the first column of Fig. 4.2.

4.3 Results and Discussion

4.3.1 General effects of self-shielding

To investigate the effect of self-shielding on tail morphology and transit shape and depth, over a large mass-loss range, we first simulated self-shielding and non-self-shielding tails integrating the mass-loss over one orbital period of Kepler-1520 b. The transit depths are shown in the upper panel of Fig. 4.1, with their ratio shown in the lower panel. At mass-loss rates $< 1 M_\oplus \text{ Gyr}^{-1}$ both models show very similar depths due to the insignificant amount of self shielding. In the range $1 - 10 M_\oplus \text{ Gyr}^{-1}$ the self-shielding models give a 20 – 40% larger transit depth.

For mass-loss rates $\gtrsim 10 M_\oplus \text{ Gyr}^{-1}$ the self-shielding models give shallower transit depths (after one orbit). This behaviour is caused by self-shielding affecting

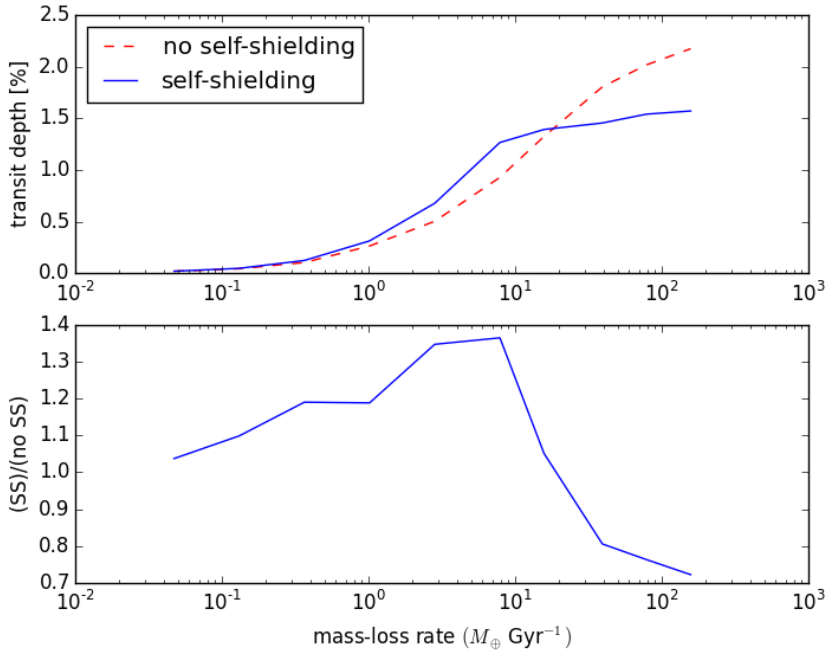


Figure 4.1: Top: Simulated transit depths from self-shielding (solid blue) and non-self-shielding (red dashed) tails after one orbit as a function of planet mass-loss rate. Bottom: Ratio of self-shielding to non-self-shielding transit depths after one orbit.

the transit depth in two opposing ways: #1) It reduces the particle sublimation rate so that more mass is retained in the tail, leading to deeper transit depths. #2) It reduces the radiation pressure, slowing the drift rate of particles away from the planet. This increases the time required for a long tail to form so that after one orbit, there is a smaller transit-cross section compared to the non-self-shielding case, leading to shallower transit depths. In the mass-loss rate range of $1 - 10 M_{\oplus} \text{ Gyr}^{-1}$, the moderate self-shielding causes reason #1 to dominate while for mass-loss rates $\gtrsim 10 M_{\oplus} \text{ Gyr}^{-1}$, the stronger self-shielding causes reason #2 to dominate. The long-term evolution of self-shielded tails is discussed in Section 4.3.5.

The effect of self-shielding on tail morphology is illustrated in Fig. 4.2 for mass-loss rates of 0.1, 1, 10, and $100 M_{\oplus} \text{ Gyr}^{-1}$. The top-row panels show the X-Y view (from above the orbital plane), the middle-row panels show the X-Z view (in the orbital plane), and the bottom row shows the transit light curves.

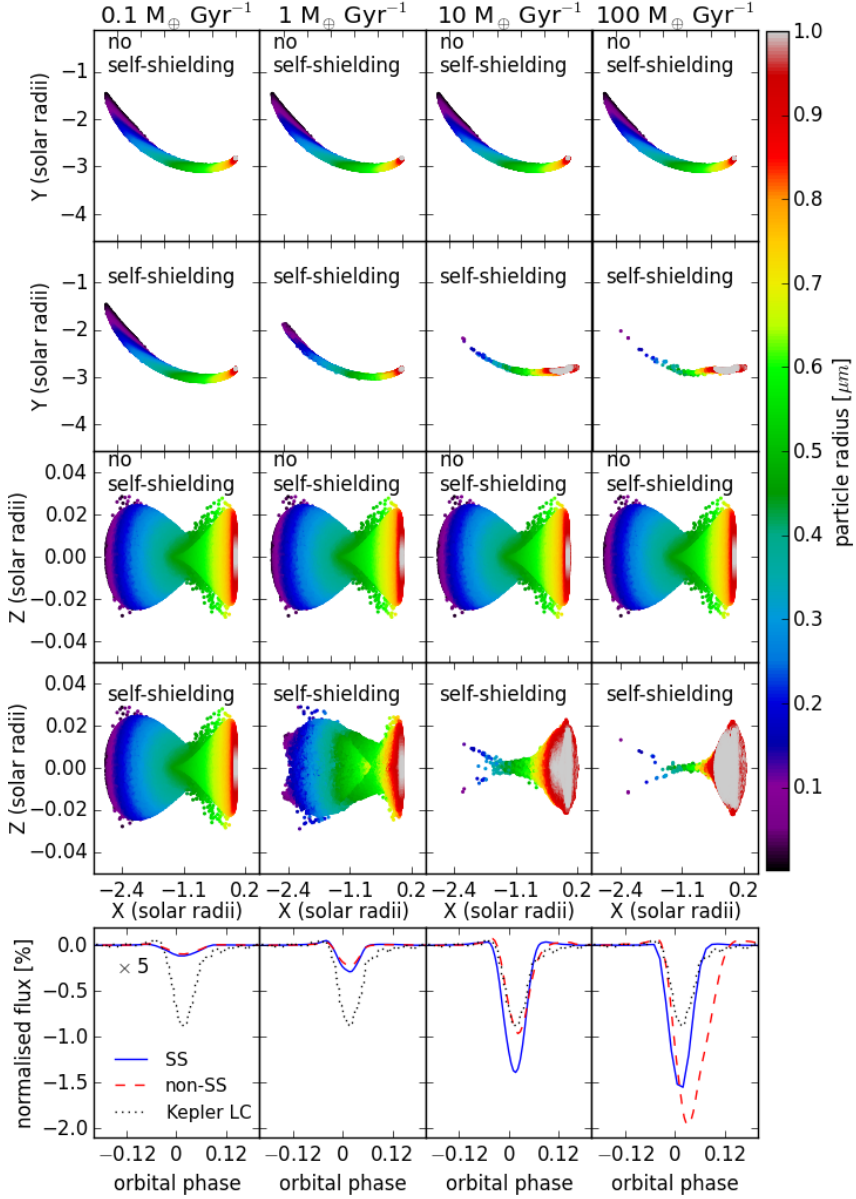


Figure 4.2: Simulated dust tails and their transit light curves after evolving over one orbit of Kepler-1520 b with and without accounting for self-shielding, for mass-loss rates of 0.1 , 1 , 10 and $100 M_{\oplus} \text{ Gyr}^{-1}$. The 3D tails are viewed from above the orbital plane (first two rows) and along the orbital plane (second two rows). The simulated light curves were convolved with the Kepler long cadence exposure window function and the transit depths for the $0.1 M_{\oplus} \text{ Gyr}^{-1}$ case were increased by a factor of 5 for clarity.

4.3.2 Fitting the average transit of Kepler-1520 b with the self-shielding model

Since accounting for self-shielding reduces the effective sublimation rate, the average transit depth of Kepler-1520 b can be produced with a lower mass-loss rate than was required in Chapter 3. To determine the required mass-loss rate, we decreased it in a trial-and-error manner, while keeping all other input parameters constant. We found that a mass-loss rate of $3.9 M_{\oplus} \text{ Gyr}^{-1}$ resulted after one orbit in a reasonable transit depth compared to that observed on average. However the tail had not reached a steady state. Evolving it for two more orbits allowed it to reach a quasi-steady state³, resulting in a significantly larger transit cross-section, producing deeper transits, as shown in Fig. 4.3. The light curve after one orbit matches the pre-ingress forward scattering peak, depth and width reasonably well but like the tails presented in Chapter 3, it over-estimates the forward scattering at egress. The light curves after evolving over a timescale of three orbits are deeper and better reproduce the extended egress. If the tail is allowed to evolve for several orbits until it reaches a steady state, a mass-loss rate of $3 M_{\oplus} \text{ Gyr}^{-1}$ (down from $7 M_{\oplus} \text{ Gyr}^{-1}$ in the non-self-shielding case) reproduces a transit depth comparable to the average long-cadence light curve of Kepler-1520 b.

The reduced sublimation rate allows particles to survive for more than one orbit, which violates the observed lack of correlation between consecutive transit depths (van Werkhoven et al. 2014). To estimate the magnitude of the correlation that would be produced, we stopped ejecting new particles into this tail after one orbit and let the tail evolve for two more orbits. The tail had completely sublimated by the time of the third transit, however, there was still a significant tail present at the time of the second transit, as shown in Fig. 4.4. The tail from these persisting particles is relatively optically thin with a maximum optical depth of $\tau = 0.57$ and a mean optical depth of 0.10. The transit light curve that this tail produces is shown in Fig. 4.4 and has a transit depth of approximately 0.3% and reproduces the extended egress better than the previously presented tails because the particles have had more time to be distributed along the tail.

4.3.3 Reduction of the intrinsic sublimation rate

To determine whether it is possible for a self-shielding tail produced by a mass-loss rate of $3.9 M_{\oplus} \text{ Gyr}^{-1}$ to result in uncorrelated consecutive transit depths as should be the case for Kepler-1520 b, we simulated a tail with the same input parameters

³The reduced sublimation rate from self-shielding prevents the particles being lost at the same rate as they are being added, however the tail morphology is constant after two orbits. We reduced the number of particles by a factor of 10 to allow us to run a simulation of continual mass-loss for many orbits and found that it reached an approximate steady state after 10 orbits.

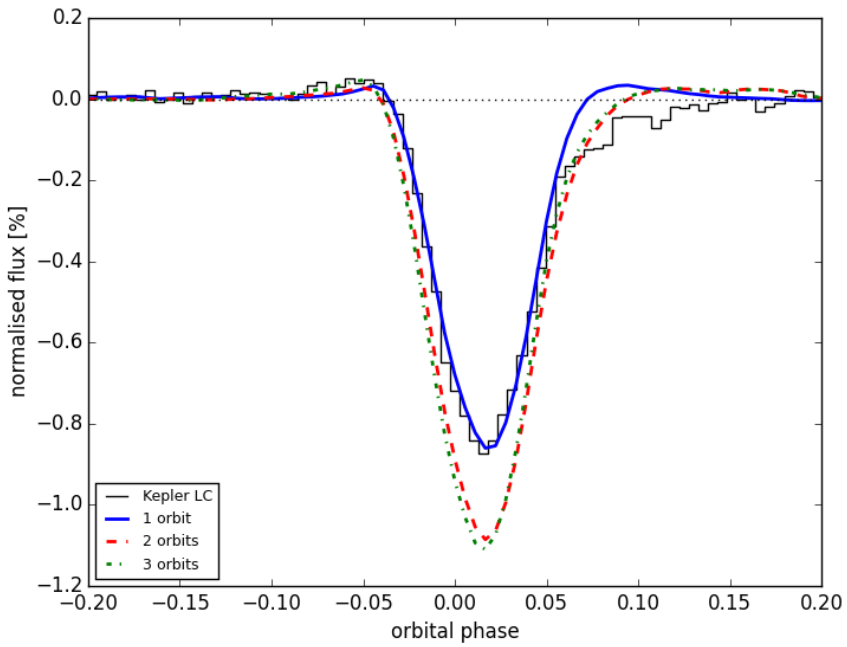


Figure 4.3: Light curves produced by a mass-loss rate of $3.9 M_{\oplus} \text{ Gyr}^{-1}$ after one (blue solid), two (red dashed) and three (green dashed-dotted) orbits of continuous mass-loss for Kepler-1520 b.

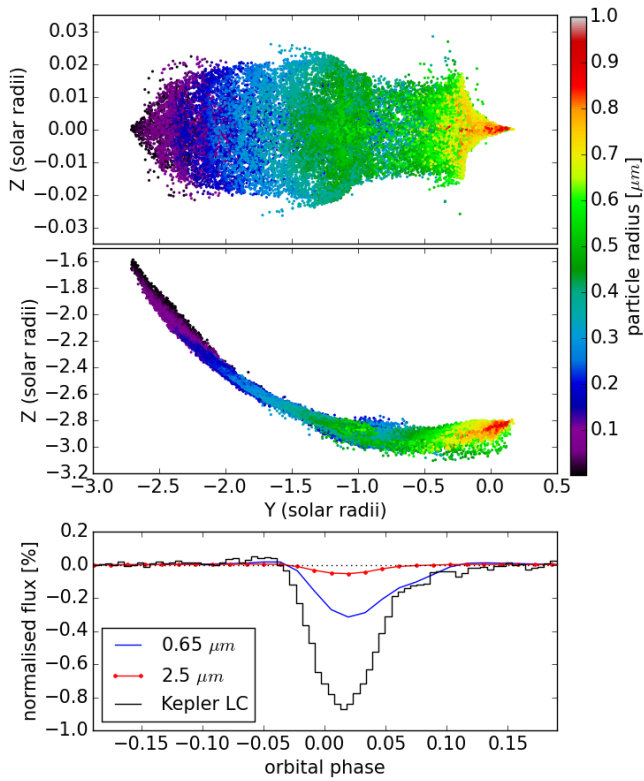


Figure 4.4: Same as a column in Fig. 4.2 after one orbit of losing mass at a rate of $3.9 M_{\oplus} \text{ Gyr}^{-1}$ and a second orbit without losing any mass for Kepler-1520 b.

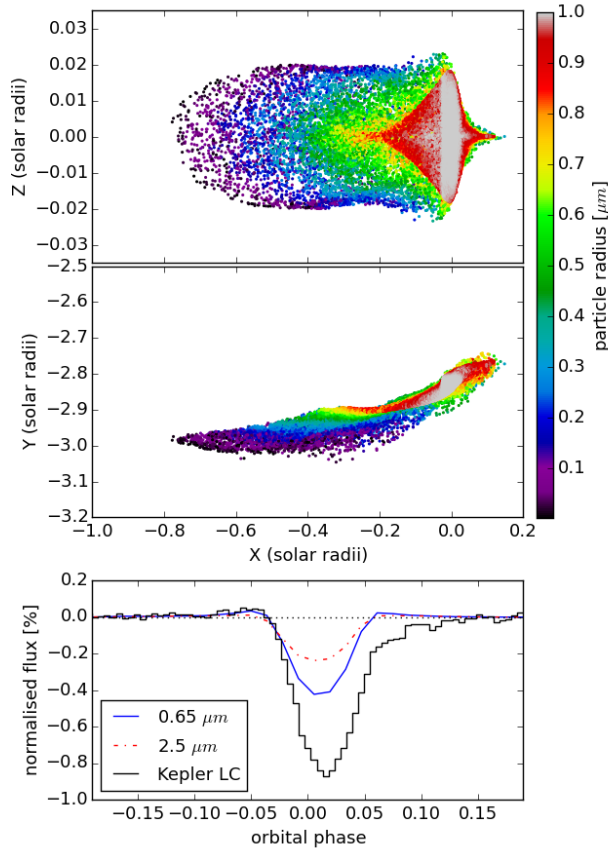


Figure 4.5: Same as a column in Fig. 4.2 except with a mass-loss rate of $3.9 M_{\oplus} \text{Gyr}^{-1}$ and an intrinsic sublimation rate increased by a factor of three.

as the one presented in Section 4.3.2 but increased the intrinsic sublimation rate by a factor of three. We continuously ejected particles for the first orbit, then stopped ejecting particles, and let the tail continue to evolve. With this increased sublimation rate, all of the particles had sublimated after 1.8 orbits, which may result in uncorrelated consecutive transit depths if the particles for the next orbit are ejected in the last 20% of its orbit. This tail and its light curve are shown in Fig. 4.5. The shorter length of this tail reduces the transit depth and duration.

4.3.4 Short-time scale outbursts

Shielded particles receive a reduced stellar flux which causes them to sublimate and drift away from the planet at a reduced rate. This means that a significant tail

can form, even if all of the particles are ejected on a timescale that is much shorter than the orbital period. To demonstrate this concept in the framework of Kepler-1520 b, we simulated a tail with a high initial mass-loss rate of $780 M_{\oplus} \text{ Gyr}^{-1}$ for only 1% of its first orbit and allowed it to evolve until three orbits had elapsed. This is equivalent to the mass-loss rate found in Chapter 3 that was needed for a non-self-shielding tail to match the average transit depth of Kepler-1520 b. To highlight the difference caused by accounting for the self-shielding, we also simulated a tail that neglected self-shielding but used almost identical input parameters. The only parameter that we changed was the sublimation rate, which we reduced by a factor of three. This was necessary to allow the particles in the non-self-shielding case to survive for three orbits to be comparable to the longer surviving particles in the self-shielding case. The simulated tails for both cases at the times of 0.6, 1.2, 1.8, 2.4 and 3.0 orbital periods are shown in Figs. 4.6 and 4.7.

In the non self-shielding case, all of the particles immediately experience the full radiation pressure and independently follow their rosette-like trajectories in a reference frame co-rotating with the planet (e.g. Rappaport et al. 2014; van Lieshout et al. 2014). If a single particle were tracked over these three orbits, it would pass through each of the arcs shown in the top left panel of Fig. 4.7. Without self-shielding to reduce the radiation pressure, the particles drift approximately half an orbital circumference away from the planet. Due to the particles moving far away from the planet, the timing of the transit varies.

In the self-shielding case, the tail initially has a high density and optical depth. The average optical depth for 0.6, 1.2, 1.8, 2.4 and 3.0 orbits are $\tau = 3.8, 1.2, 0.60, 0.76$ and 0.28 , respectively. This significantly changes the particle dynamics and the resulting tail morphology and transit light curve. It shows that the particle sublimation rate can be affected enough to allow a significant tail to be present three orbits after ejecting an optically thick cloud of particles. If the mass-loss from the planet did occur in bursts shorter than an orbital period, this could have an implication on the total mass-loss rate from the planet, because mass-loss is generally assumed to be continuous (e.g. Perez-Becker & Chiang 2013). However, such a scenario could not be responsible for the case of Kepler-1520 b because it would lead to a correlation between consecutive transits which is not observed (van Werkhoven et al. 2014).

Taking an average of the light curves at the times of 0.6, 1.2, 1.8, 2.4 and 3.0 orbits significantly reduces forward scattering at egress, alleviating the issue with some of our other models. This suggests that average light curves may be best reproduced by averaging the light curves produced by different tail morphologies, such as those shown in Fig. 4.6, which cancel out the forward scattering peak that would otherwise occur at egress.

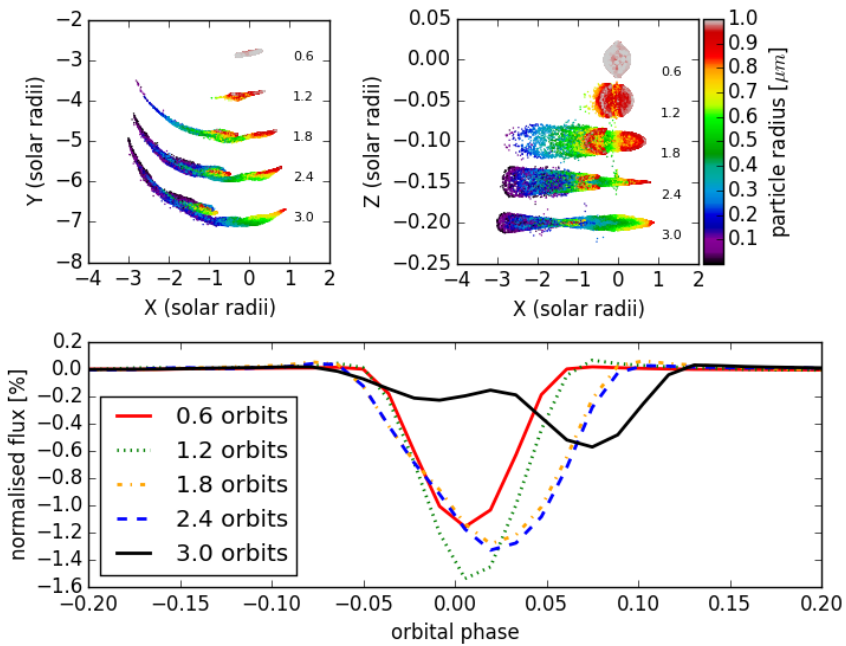


Figure 4.6: Series of snapshots of an optically thick tail that was produced by a large initial outburst with mass-loss rate $780 M_{\oplus} \text{Gyr}^{-1}$ that only lasted for 1% of the first orbit. This mass-loss rate is equivalent to a mass-loss rate of $7.8 M_{\oplus} \text{Gyr}^{-1}$ that lasts for the entire orbit.

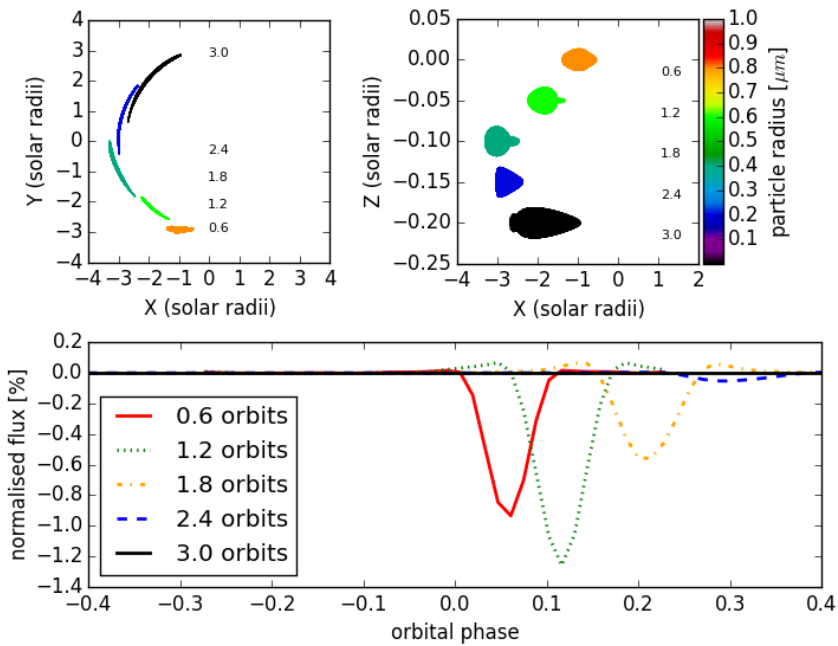


Figure 4.7: Like Fig. 4.6 except in this case the tail's self-shielding was neglected. The sublimation rate was also decreased by a factor of three to allow the non-shielded particles to survive for three orbits.

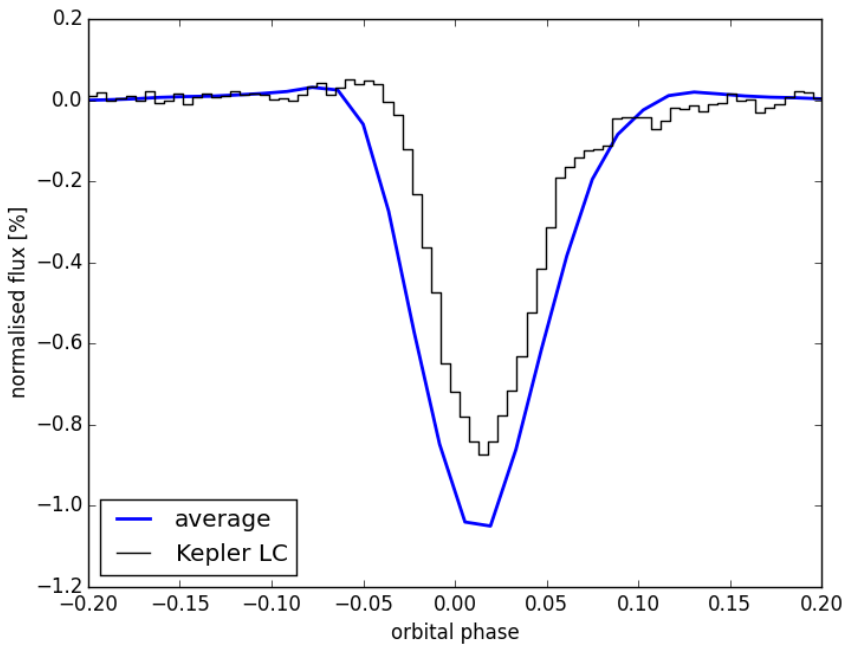


Figure 4.8: The average of the light curves shown in Fig. 4.6 (blue) compared the average Kepler long cadence light curve of Kepler-1520 b (black steps). The excessive forward scattering at egress that is present in some of our other individual light curves is not present in this average.

4.3.5 Highly optically thick regime

As shown in Fig. 4.2, a high mass-loss rate makes the tail form much slower because the shielded particles move away from the planet more slowly as a result of the reduced radiation pressure. However, if high mass-loss rate tails are allowed to evolve for more than one orbit, a significant tail can form, as shown in Figs. 4.9 and 4.10 for mass-loss rates of 10 and $100 M_{\oplus} \text{Gyr}^{-1}$, respectively. The first row shows a non-self-shielding tail that is in a steady state after one orbit. The middle three rows show the evolving tail after continuously losing mass for three orbits, and the bottom row shows the simulated transit light curves at these different times.

The $100 M_{\oplus} \text{Gyr}^{-1}$ tail was challenging to model because its high density required an optical depth grid that had a higher resolution than what we were able to use due to computational limitations. This prevented us from modeling the optically thin surface layer that should be present in an optically thick tail. However, we approximated it by setting the optical depth of the cells along the surface of the tail facing the star to zero, allowing all of the particles within these surface layer cells to experience the full radiation pressure. This is an upper limit because in reality only particles within part of the surface layer cells will experience the full radiation pressure. The number of particles in the 0.1 and $1 M_{\oplus} \text{Gyr}^{-1}$ cases in Fig. 4.2 stayed at a steady value after one orbit. However, after running for the maximum time of three orbits set by computational limitations, the 10 and $100 M_{\oplus} \text{Gyr}^{-1}$ cases did not reach a steady state in particle numbers. Despite this, the shape of the tail did not significantly change from the second to the third orbit, indicating that it had reached a quasi-steady state.

The slow tail formation occurs because the particles in the exposed surface layer sublimate and experience a stronger radiation pressure, which peaks for particle sizes around $0.1 \mu\text{m}$ (e.g. van Lieshout et al. 2014). This stronger radiation pressure pushes the surface layer particles further into the tail, which significantly reduces the radiation pressure that they experience.

This slow tail formation rate implies that very high mass-loss rates would produce correlated increasing transit depths, which has not been observed in any of the currently known disintegrating rocky exoplanets. However, it is likely that TESS will discover more of these objects and if some exhibit correlated transits that increase in depth, it may indicate an intermittent high mass-loss rate from the planet.

4.4 Conclusions

We have shown that self-shielding of dust tails from disintegrating rocky exoplanets can affect the tail morphology. In particular, we show that a self-shielding dust tail can produce a reasonable match to the Kepler average long cadence light curve

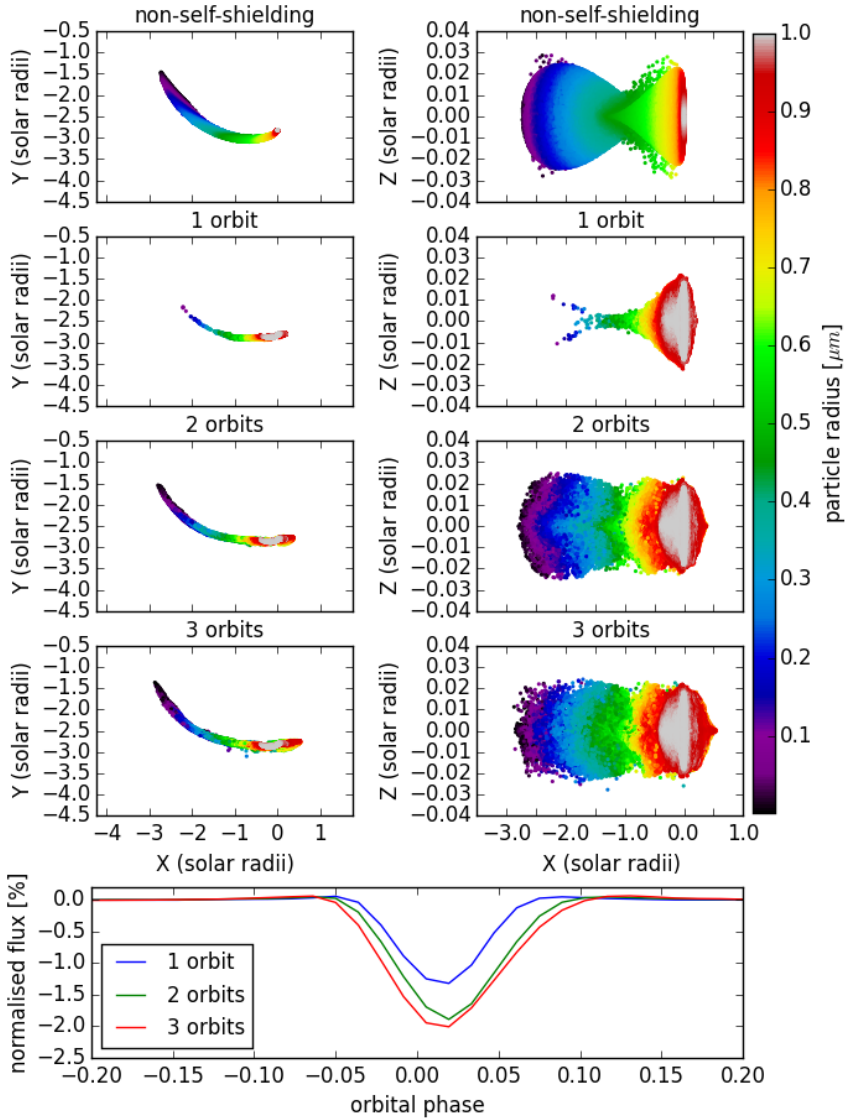


Figure 4.9: Evolution of a highly self-shielding tail produced by a planet mass-loss rate of $10 M_{\oplus} \text{ Gyr}^{-1}$. Left: View of the tail from above the orbital plane. Right: View of the tail from the orbital plane. The first row shows a non-self-shielding tail that is in a steady state after one orbital period. The three middle rows show a self-shielding tail of mass-loss rate $10 M_{\oplus} \text{ Gyr}^{-1}$ after one, two and three orbits. The last row shows the transit light curves produced by the self-shielding tail after evolving for one, two and three orbits.

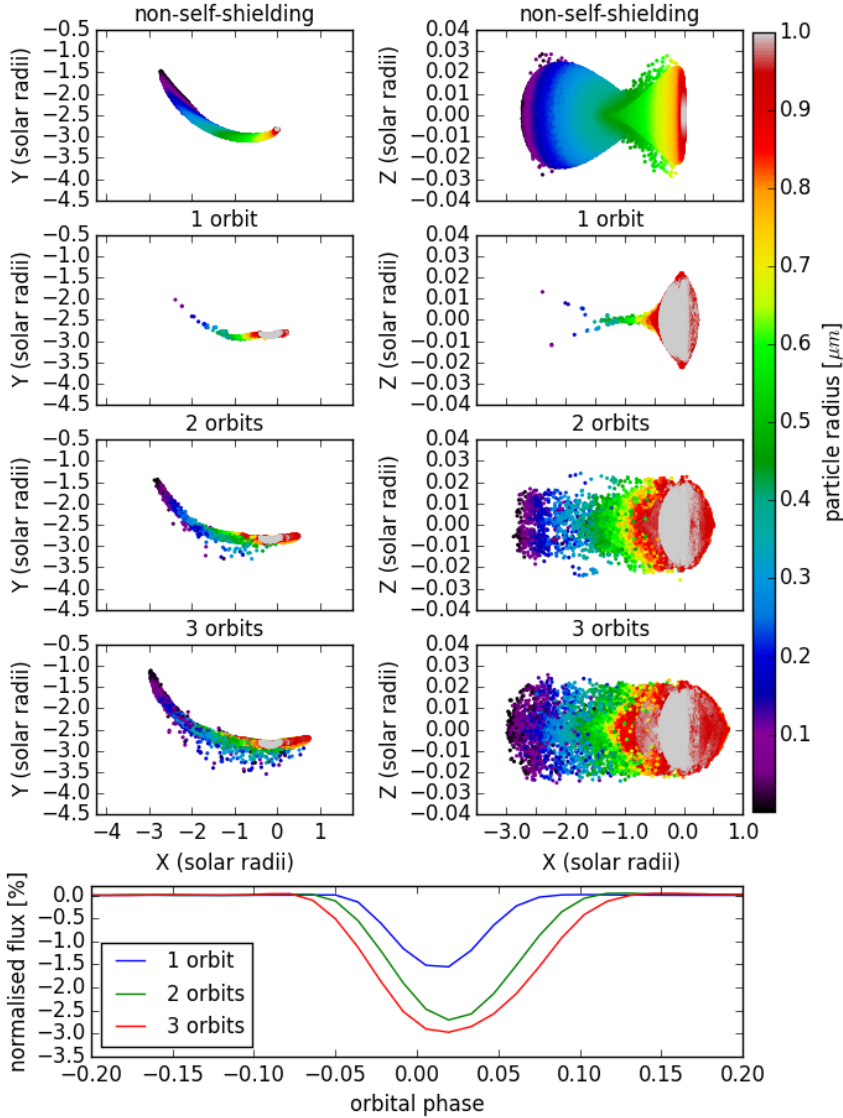


Figure 4.10: Same as for Fig. 4.9 except for using a mass-loss rate of $100 M_{\oplus} \text{ Gyr}^{-1}$.

of Kepler-1520 b with a mass-loss rate of $3 - 3.9 M_{\oplus} \text{ Gyr}^{-1}$ which is lower than the rate that was required for a non-self-shielding tail in Chapter 3. However, they provide so much self-shielding that particles can survive for more than one orbital period, leading to correlations between consecutive transit depths which are not observed (van Werkhoven et al. 2014). Lower mass-loss rates with a more volatile material (with a faster intrinsic sublimation rate) can alleviate this issue, however these tails produce shallow transit depths due to their reduced length and transit cross-section.

We demonstrate that a tail can form with a mass-loss time scale that is much shorter than an orbital period. This may have implications for calculated mass-loss rates, which are usually assumed to occur over an orbital period (e.g. Perez-Becker & Chiang 2013). We also show that tails with mass-loss rates $\gtrsim 10 M_{\oplus} \text{ Gyr}^{-1}$ take a significantly longer time to form due to the strong self-shielding reducing the radiation pressure and drift rate away from the planet. This scenario would produce correlated increasing transit depths, which may provide a way to identify tails that were produced by high mass-loss rates in the era of TESS.

4.5 Future outlook

TESS is expected to discover several disintegrating rocky exoplanets around brighter stars, making detailed observational characterisation possible. The interpretation of these observations will depend critically on the accuracy of the dust-tail models that are used.

Gas is expected to be present in dust tails because it will be produced by the sublimation of dust particles and the planet's mass-loss mechanism which likely involves a gaseous outflow (Perez-Becker & Chiang 2013). Therefore, future models should account for gas pressure affecting the particle dynamics. This modeling effort will be significantly aided by observational constraints on gas density.

Since the dust particles likely condense in a gaseous outflow from the planet (Perez-Becker & Chiang 2013), a better understanding of the density of gas may enable the initial dust-grain size distribution to be better understood. This distribution may affect the tail's density profile so it should also be accounted for in future models.

Acknowledgements

A. R. R.-H. is grateful to the Planetary and Exoplanetary Science (PEPSci) programme of the Netherlands Organisation for Scientific Research (NWO) for support. I. A. G. S. acknowledges support from an NWO VICI grant (639.043.107).

Bibliography

- Alonso, R., Rappaport, S., Deeg, H. J., & Pallé, E. 2016, *A&A*, 589, L6
- Bochinski, J. J., Haswell, C. A., Marsh, T. R., Dhillon, V. S., & Littlefair, S. P. 2015, *ApJ*, 800, L21
- Bourrier, V., Lecavelier des Etangs, A., & Vidal-Madjar, A. 2014, *A&A*, 565, A105
- Brogi, M., Keller, C. U., de Juan Ovelar, M., et al. 2012, *A&A*, 545, L5
- Budaj, J. 2013, *A&A*, 557, A72
- Burns, J. A., Lamy, P. L., & Soter, S. 1979, *Icarus*, 40, 1
- Croll, B., Rappaport, S., DeVore, J., et al. 2014, *ApJ*, 786, 100
- Koike, C., Kaito, C., Yamamoto, T., et al. 1995, *Icarus*, 114, 203
- Min, M., Dullemond, C. P., Dominik, C., de Koter, A., & Hovenier, J. W. 2009, *A&A*, 497, 155
- Min, M., Hovenier, J. W., & de Koter, A. 2005, *A&A*, 432, 909
- Murgas, F. 2013, PhD thesis, Departamento de astrofísica, universidad de La Laguna
- Perez-Becker, D. & Chiang, E. 2013, *MNRAS*, 433, 2294
- Rappaport, S., Barclay, T., DeVore, J., et al. 2014, *ApJ*, 784, 40
- Rappaport, S., Levine, A., Chiang, E., et al. 2012, *ApJ*, 752, 1
- Sanchis-Ojeda, R., Rappaport, S., Pallé, E., et al. 2015, *ApJ*, 812, 112
- van Lieshout, R., Min, M., & Dominik, C. 2014, *A&A*, 572, A76
- van Lieshout, R., Min, M., Dominik, C., et al. 2016, *A&A*, 596, A32
- van Werkhoven, T. I. M., Brogi, M., Snellen, I. A. G., & Keller, C. U. 2014, *A&A*, 561, A3
- Vanderburg, A., Johnson, J. A., Rappaport, S., et al. 2015, *Nature*, 526, 546

5 | Search for gas from the disintegrating rocky exoplanet K2-22b

Based on:

Ridden-Harper, A. R.; Snellen, I. A. G.; Keller, C. U.; P. Mollière, submitted to A&A

Context. The red dwarf star K2-22 is transited every 9.14 hours by an object which is best explained by being a disintegrating rocky exoplanet featuring a variable comet-like dust tail. While the dust is thought to dominate the transit light curve, gas is also expected to be present, either from being directly evaporated off the planet or by being produced by the sublimation of dust particles in the tail.

Aims. Both ionized calcium and sodium have large cross-sections, and although present at low abundance, exhibit the strongest atomic absorption features in comets. We therefore identify these species also as the most promising tracers of circumplanetary gas in evaporating rocky exoplanets and search for them in the tail of K2-22 b to constrain the gas-loss and sublimation processes in this enigmatic object.

Methods. We observed four transits of K2-22 b with X-shooter on ESO's Very Large Telescope to obtain time-series of intermediate-resolution ($R \sim 11400$) spectra. Our analysis focused on the two sodium D lines (588.995 nm and 589.592 nm) and the Ca^+ triplet (849.802 nm, 854.209 nm and 866.214 nm). The stellar calcium and sodium absorption is removed using the out-of-transit spectra. Planet-related absorption is searched for in the velocity rest frame of the planet, which changes from approximately -66 to $+66$ km s^{-1} during the transit.

Results. We reached 5σ upper-limits on the tail's sodium and ionized calcium absorption of 9% and 1.4%, respectively. Assuming their mass fractions to be similar to those in the Earth's crust, these limits correspond to scenarios in which only 0.01% and 0.3% of the transiting dust is sublimated and observed as absorbing gas. However, this assumes the gas to be co-moving with the planet. We show that for the high irradiation environment of K2-22 b, sodium and ionized calcium could be quickly accelerated to 100s of km s^{-1} due to radiation pressure and entrainment by the stellar wind, making them much more difficult to detect. No evidence for such possibly broad and blue-shifted signals are seen in our data.

Conclusions. Future observations aimed at observing circumplanetary gas should take into account the possible broad and blue-shifted velocity field of atomic and ionized species.

5.1 Introduction

The NASA Kepler and K2 space missions have unveiled a new class of stars which are transited in short regular intervals of a day or less by objects that are best explained as disintegrating, rocky planets. They produce light curves that randomly vary in depth and shape (typically at $<2\%$) from one orbit to the next, showing features attributed to dust tails, such as forward scattering peaks and asymmetric transit profiles (e.g. Rappaport et al. 2012; Sanchis-Ojeda et al. 2015). During some orbits, the transit can apparently be absent, implying that the transiting parent bodies themselves are too small to be detected, in line with the requirement of low surface gravities to allow a dust-tail to be launched from a planetary surface. A proposed mechanism for this mass-loss is a thermally driven hydrodynamic outflow that may be punctuated by volcanic eruptions (Perez-Becker & Chiang 2013). The composition of the dust likely reflects the composition of the planet, making them excellent targets to study their surface geology. For instance, mass loss and dust composition can be constrained by comparing dust-tail models to transit light curves (Rappaport et al. 2012, 2014; Brogi et al. 2012; Budaj 2013; van Lieshout et al. 2014; Sanchis-Ojeda et al. 2015; van Lieshout et al. 2016, Chapters 3 & 4), and wavelength dependent dust extinction models to spectrophotometric observations (e.g. Croll et al. 2014; Murgas 2013; Bochinski et al. 2015; Alonso et al. 2016).

However, potentially much stronger constraints on the underlying physical mechanisms of mass-loss and the composition of the lost material can be derived by observing the gas that is expected to be evaporated directly from the planet or produced by the sublimation of dust particles in the tail. No such observations yet exist except for the more exotic object transiting the white dwarf WD 1145+017, which appears to have several clumps of closely-orbiting material (Vanderburg et al. 2015; Rappaport et al. 2016). Redfield et al. (2017) observed this system with KECK/HIRES and VLT/X-shooter at five epochs over the course of a year and detected varying circumstellar absorption in more than 250 lines from 14 different atomic or ionized species (O I, Na I, Mg I, Al I, Ca I, Ca II, Ti I, Ti II, Cr II, Mn II, Fe I, Fe II, Ni I, and Ni II).

K2-22 b is one of the four disintegrating planet systems known to date, and is the most promising for detecting gas due to its relative brightness ($R=15.01$; Rappaport et al. 2012, 2014; Sanchis-Ojeda et al. 2015; Vanderburg et al. 2015). Its host star is an M dwarf ($T_{\text{eff}} = 3830$ K) that has a fainter ($R = 18.79$) M-dwarf companion ($T_{\text{eff}} = 3290$ K) approximately 2 arcsec away. It has an orbital period of 9.146 hours and produces transit depths that vary from approximately $\lesssim 0.14$ to 1.3%, with a mean depth of 0.55%. The minimum transit depth implies an upper-limit on the size of the disintegrating hard-body planet of $2.5 R_{\oplus}$, assuming a stellar radius of $0.57 R_{\odot}$ (Sanchis-Ojeda et al. 2015).

In contrast to the other known members of this class of object, it appears to exhibit a leading tail producing a large forward scattering peak at egress (Sanchis-Ojeda et al. 2015). This is possible for dust particles that experience a radiation pressure force to stellar gravitational force ratio (β) of $\lesssim 0.02$. Such particles could either have radii $\lesssim 0.1 \mu\text{m}$ or $\gtrsim 1 \mu\text{m}$. In contrast, the post-transit forward scattering bump requires particle sizes of approximately $0.5 \mu\text{m}$.

A wavelength dependence in transit depth has been observed on at least one occasion (Sanchis-Ojeda et al. 2015), which allowed the Angstrom exponent, α , to be computed, which is defined as $-d \ln \sigma / d \ln \lambda$, where σ is the effective extinction cross section and λ is the wavelength. It indicates a non-steep power-law dust size distribution with a maximum size of approximately $0.5 \mu\text{m}$. Considering all of these particle size constraints, Sanchis-Ojeda et al. (2015) conclude that a large fraction of particles must have sizes of approximately $1 \mu\text{m}$. Assuming a high-Z dust composition, they estimate a mass-loss rate of approximately $2 \times 10^{11} \text{ g s}^{-1}$.

In this paper we report on a search for sodium and ionized calcium in intermediate resolution spectroscopic time-series data from VLT/X-shooter, focusing on the sodium D lines and the ionized calcium infrared triplet lines. These species and lines were detected in WD 1145+017 by Redfield et al. (2017), which is expected due to their low sublimation temperatures (e.g. Haynes 2011), likely presence in terrestrial planet compositions and large absorption cross-sections (e.g. Mura et al. 2011). This paper is structured as follows: Section 5.2 describes our observational data, Sections 5.3 and 5.4 describe our methods, Section 5.5 presents and discusses our results and Section 5.6 concludes.

5.2 Observational data

We observed transits of the rocky disintegrating planet K2-22 b on the nights of March 18 & April 4, 2017, and March 10 & March, 18, 2018 with X-shooter (Vernet et al. 2011), installed at the Cassegrain focus of ESO’s Very Large Telescope Telescope (VLT) at the Paranal Observatory under program ID 098.C-0581(A) (PI:Ridden-Harper). The three-arm configuration of X-shooter, ultraviolet-blue (UVB), visual-red (VIS) and near-infrared (NIR), allows it to quasi-simultaneously observe the spectral range of 300 – 1500 nm.

These observations were carried out in nodding mode (in an ABBA pattern) with a nod-throw length of 4 arcsec along the slit. During the three hours of observations on each night, 26 individual exposures of 213 seconds were obtained in the VIS arm. The observing dates, transit timing, exposure times and orbital phase coverage are shown in Table 5.1. We used slit widths in the UVB, VIS and NIR arms of 0.5, 0.7 and 0.4 arcsec, which resulted in resolving powers of $R \approx 9700$, 11400 and 11600, respectively.

X-shooter does not have an atmospheric dispersion corrector (ADC). Therefore after every hour of observing the target was re-acquired and the slit was aligned again to the parallactic angle to minimize slit-losses. The observations were reduced using the standard nodding mode recipes from the X-shooter Common Pipeline Library (CPL)¹. To enable sky background subtraction, every two exposures (AB or BA) were combined, resulting in 13 1D wavelength-calibrated spectra.

The last four spectra of Night 1 were contaminated by the faint M-dwarf companion of K2-22 that moved into the slit. Due to the apparent difference in spectral type between the target and the companion, the observed depth of the stellar absorption lines changes, making accurate relative spectrophotometry impossible. We therefore excluded this night from the analysis.

5.3 Analyses

Our analyses focused on the two sodium D lines (588.995 nm and 589.592 nm) and the Ca⁺ near-infrared triplet (849.802 nm, 854.209 nm and 866.214 nm), which were both captured by the VIS arm of X-shooter. The observed spectral regions are dominated mainly by stellar and some telluric lines. Both the reflex motion of the star around the system's barycenter² and the change in the radial component of the velocity of the observatory towards the star are so small that they can be considered to be non-variable, as well as the position (but not the strength) of the telluric lines. In contrast, the orbital velocity of the planet is large, leading to a change in the radial component during transit from approximately -66 to $+66$ km s⁻¹. The resulting Doppler shift of the planetary lines can be used to separate them from the stellar and telluric features. The analysis was carried out as in Chapter 2, but is summarised below for completeness. It is comprised of the following steps, and is near identical for the investigation of both the calcium and sodium lines.

1. Normalization to a common flux level: Variable slit losses and atmospheric scattering cause the spectra to have different flux levels. This is corrected by division through their median value for a wavelength range close to the targeted lines (to avoid offsets due to variable low-frequency trends in the spectra). This normalization is possible because transmission spectroscopy depends on the relative change in flux as a function of wavelength and is therefore not an absolute measurement.

¹ Available at: <https://www.eso.org/sci/software/pipelines/xshooter/>

² Sanchis-Ojeda et al. (2015) did not detect any radial velocity variations in the spectrum of K2-22 (accurate to ± 0.3 km s⁻¹).

Table 5.1: Details of the observations. The orbital phases of K2-22 b are based on the orbital parameters derived by Sanchis-Ojeda et al. (2015).

data set	Night 1	Night 2	Night 3	Night 4
date (UTC)	19 March 2017	4 April 2017	11 March 2018	19 March 2018
start	0.832	0.833	0.856	0.806
phase	0.150	0.147	0.178	0.122
end	419.3	414.3	423.2	416.6
phase	213 [†]	213 [†]	213 [†]	213 [†]
cadence (s)	02:00:34	02:08:22	03:54:45	03:30:56
exposure	03:00:31	03:08:45	04:41:20	04:45:12
time (s)	03:24:31	03:32:45	05:05:20	05:09:12
observation	03:48:31	03:56:45	05:29:20	05:33:12
start (UTC)	04:55:18	05:01:00	06:51:06	06:24:31
transit	5	5	4	6
start* (UTC)	4	4	4	4
mid-transit	4	4	5	3
time* (UTC)	13	13	13	13
transit				
end* (UTC)				
observation				
end (UTC)				
Nr. spectra				
pre-transit				
Nr. spectra				
in transit				
Nr. spectra				
post-transit				
total Nr.				
of spectra				
Na D line region S/n. ¹				
average S/n.	30.79	38.44	35.65	27.92
per spectrum	61.58	76.89	71.30	55.84
total S/n				
Ca ⁺ triplet region S/n. ²				
average S/n.	101.17	111.27	113.65	111.34
per spectrum	202.33	222.54	227.29	222.69
total S/n				

* The transit times are barycentric adjusted to be as measured at the observatory.

† Except for the last two spectra which have exposure times of 211 s.

1 and 2: derived from the residuals after dividing by the mean spectrum of the featureless regions 5961.0 Å – 5965.2 Å and 8584.8 Å – 8591.8 Å, respectively.

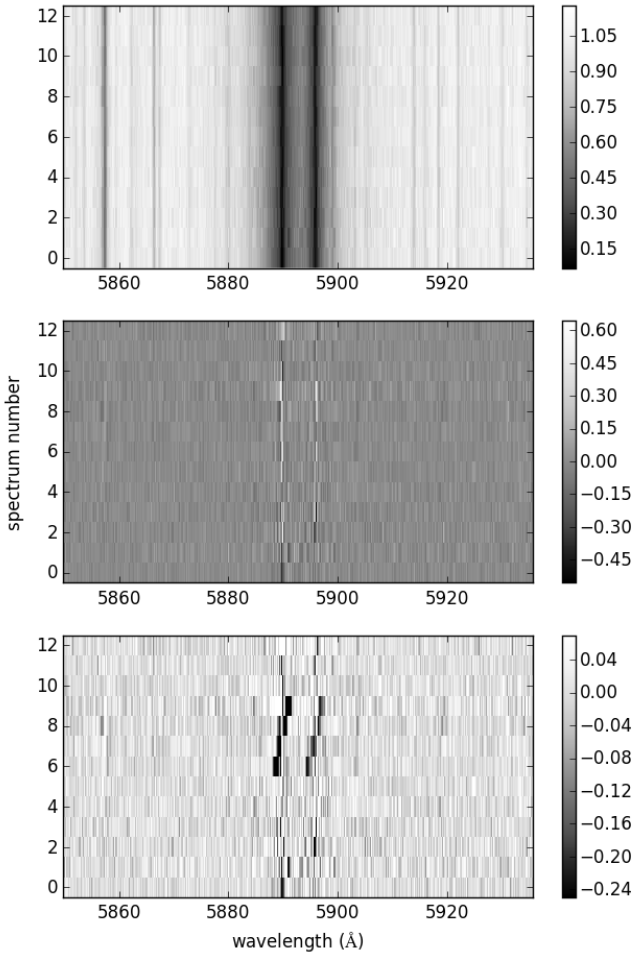


Figure 5.1: A visual representation of the processing steps as described in Section 5.3. This figure shows the data of Night 4, but the other nights are very similar. The vertical axis of each matrix represents the sequence number of the observed spectrum. The first panel shows the data around the sodium D lines after normalization and alignment in Step 2. The second panel shows the residual matrix after dividing through the average star spectrum and subtracting the mean (Step 4). The bottom panel shows the data after injecting an artificial planet signal before Step 2 that absorbs 50% of the stellar flux. The injected planet signal can be seen as a diagonal trace from spectrum number 6 to 9, resulting from the change in the radial component of the planet orbital velocity during transit.

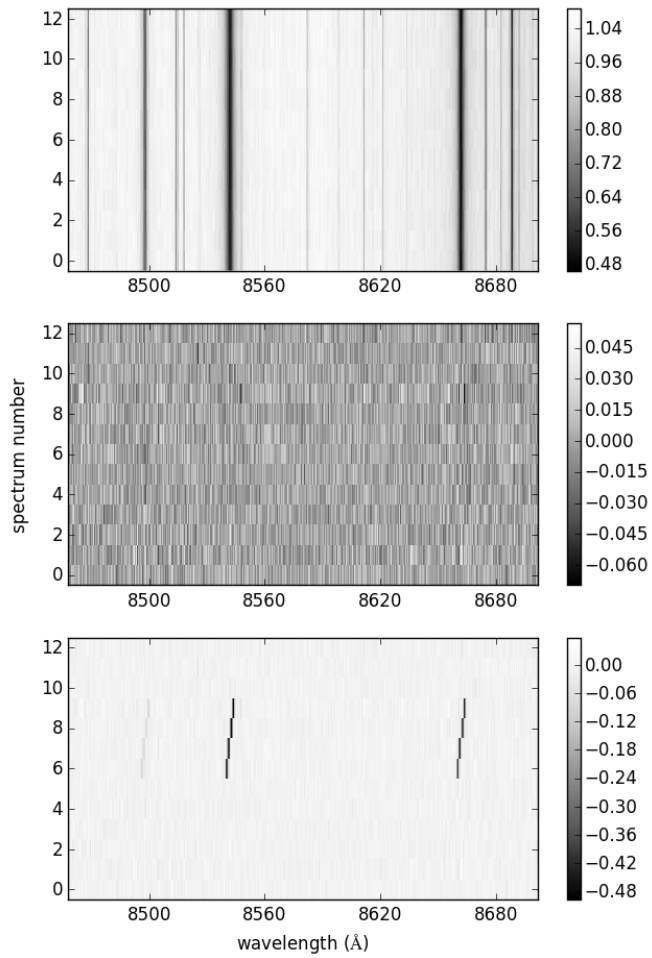


Figure 5.2: Same as Fig. 5.1 but for the ionized calcium near-infrared triplet.

2. Alignment of the spectra: Due to instrumental instability, the wavelength solution is prone to changes at a sub-pixel level. Since the absolute wavelength solution is not relevant for our analysis, the positions of strong spectral lines are fitted in each spectrum and used to shift all spectra to a common wavelength frame.
3. Removal of cosmic rays: Cosmic rays were removed by searching for 5σ outliers and replacing them with a value interpolated from a linear fit to the other spectra at the affected wavelength position.
4. Removal of stellar and telluric lines: All stationary spectral components in the spectra were removed by dividing every pixel in a spectrum by the mean value of the out-of-transit spectra at that wavelength position during the night. Since the Doppler shift of the planet lines changes by approximately 5 pixels during the transit, this procedure has only a limited effect on potential planet lines.
5. Down-weighting of noisy parts of the spectrum: Noisy parts of the spectrum, e.g. in the center of strong absorption lines or telluric lines can have a significant effect on the cross-correlation functions. Therefore the flux points at each wavelength are weighted down according to the signal-to-noise ratio as a function of wavelength, derived from the standard deviation of the residual spectra at each wavelength position. This function was scaled differently for each spectrum, such that the wavelengths where the planet's signal should be located were not changed (i.e. scaled by a factor of one). This preserved the fractional absorption of the injected planet signal relative to the stellar spectrum.
6. Combination of individual lines. The data from the three individual ionized calcium lines were combined after weighting by the line strengths. The two sodium lines were combined in the same way.
7. Combining the individual nights. We shifted the line-combined spectra to the planet rest frame using the transit timing parameters from Sanchis-Ojeda et al. (2015), and subsequently summed over all spectra taken during transit. These 1D spectra were subsequently combined for the different nights, weighted by their average signal-to-noise ratio during the night (See Table 5.1).

In many other data sets, variable telluric lines cause structure in the residual spectra that can be removed with a principle component analysis (PCA), which involves decomposing the data into principle components and removing the dominant structures by subtracting the first few dominant components (e.g. Chapter

2). However, the telluric lines did not significantly vary during these observations so PCA did not improve the recovery of our injected signals (see Section 5.4) and was not applied.

Visual representations of the data analysis process for both the Na D doublet and the Ca⁺ triplet are shown in Figs. 5.1 and 5.2, respectively.

5.4 Synthetic planet signal injection

Synthetic planet signals were injected after stage two of the analysis process (see above) to examine to what extent the analysis affects a potential planet signal and to assess the overall sensitivity of the data. The data with the artificial signals were treated in the same way as the unaltered data sets.

We injected a simple model of the Ca⁺ infrared triplet and the two Na D lines with relative line intensities approximated using Eq. 1 in Sharp & Burrows (2007), for now ignoring terms that relate to the energy level population (e.g. temperature and partition function). This means that the degeneracy factor, g , is not included in these calculations, because it is part of the level population terms. This approach assumes that the population of Na atoms is in the ground state and that all of the Ca⁺ ions are in the lower state of the triplet transition studied here. For Ca⁺ this is not the case, and we will adjust the mass limits derived for this ion using its expected population statistics in Section 5.5.1. We took the quantum parameters that describe the line transitions from the National Institute of Standards and Technology (NIST) Atomic Spectra Database (Kramida et al. 2018). The values and references are shown in Table 5.2. For the sodium D lines at 5889.95 Å and 5895.92 Å, we derive a line ratio of 2.0. For the ionized calcium triplet lines at 8498.02 Å 8542.09 Å and 8662.14 Å, the relative line strengths derived are 0.167, 1.000, 0.829, respectively.

During an exposure of 213 seconds, the radial component of the orbital velocity of the planet changes by approximately 7.5 km s⁻¹. Since each time two exposures are combined to generate one spectrum, this results in a convolution with a boxcar function with a width of 15 km s⁻¹, comparable to the instrumental resolution. The planet model spectrum was Doppler shifted to the appropriate planet velocity, assuming a circular orbit (Sanchis-Ojeda et al. 2015), and injected according to

$$F'(\lambda) = [1 - C \times F_{model}(\lambda, v_{rad})]F_{obs}(\lambda) \quad (5.1)$$

where $F_{obs}(\lambda)$ is the observed spectrum, $F_{model}(\lambda, v_{rad})$ is the Doppler-shifted model spectrum, with C as a scaling parameter that determines the amplitude of strongest line, and $F'(\lambda)$ is the resulting spectrum after injecting the synthetic

planet spectrum. To determine the upper-limits in the strength of the ionized calcium and sodium lines, the scaling parameter C was varied to reach a signal five times larger than the noise in the combined 1D planet-rest-frame spectrum.

5.5 Results and discussion

No significant signal from neither sodium nor ionized calcium was detected. Injection of synthetic planet signals indicate that 5σ upper-limits were reached when the strength of the strongest line (C in Equation 5.1) was set to 9% and 1.4% for the sodium D doublet and the Ca^+ triplet, respectively. We conservatively quote 5σ limits because a systematic noise is present at the 3σ level that was challenging to properly account for.

The combined (over individual lines and over nights 2 – 4) transmission spectrum as a function of orbital phase is shown in Figs. 5.3 and 5.4 for Na and Ca^+ , respectively. Nearest-pixel interpolation was used, necessary since observations at different nights were not performed at identical orbital phases. The panels show the data without injected signals (top), with injected signals at 5σ (middle), and at 10σ (bottom). The injected signal of sodium is significantly less pronounced around mid-transit, because it temporarily overlaps with the cores of the noisy stellar sodium absorption. These spectra are weighed down accordingly for the construction of the final 1D transmission spectrum.

The final 1D-spectra per night, and those combined over nights 2–4 are shown in Figs. 5.5 and 5.6 (with and without the injected signals) for the Na D lines and the Ca^+ triplet, respectively. The right panels are those binned by 0.8\AA to 40 km s^{-1} . Combining the two Na lines and three Ca^+ lines results in neighbouring lines being included in the combined 1D spectrum (e.g. for Na, the features at $\pm 285\text{ km s}^{-1}$).

5.5.1 Instantaneous gas-mass limits

To estimate what the observed limits mean in terms of Ca^+ , Na, and total gas mass-loss limits, we used the following equation for absorption line strength as described in Savage & Sembach (1991):

$$\tau(v) = \frac{\pi e^2}{m_e c} f \lambda N(v) = 2.654 \times 10^{-15} f \lambda N(v) \quad (5.2)$$

where f is the transition oscillator strength, λ is the wavelength in Angstroms, and $N(v)$ is the integral normalized column density per unit velocity in atoms $\text{cm}^{-2} (\text{km s}^{-1})^{-1}$. We assumed that lines from the gas would be too narrow to resolve at our instrument resolution of $R \sim 11400$ so our column density profile, $N(v)$, only accounted for the line's natural width. This was done by setting the

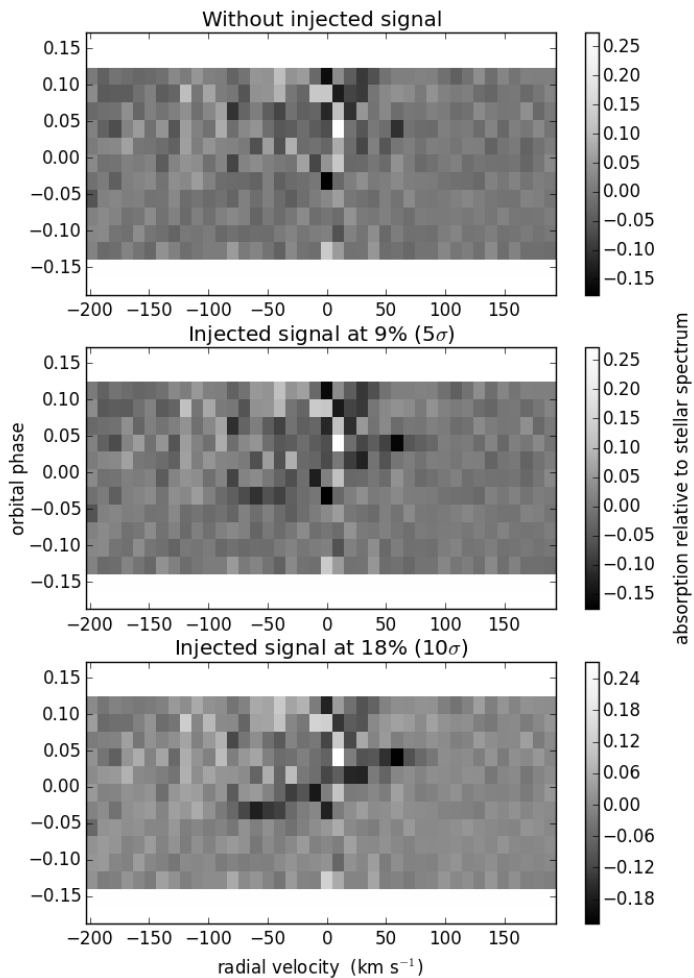


Figure 5.3: Planet Na D transmission spectrum combined from nights 2 – 4 as a function of orbital phase (vertical axis) and radial velocity in the planet rest frame, with no injected signal (top), a 9% injected signal corresponding to a 5σ limit (middle) and an 18% injected signal (bottom).

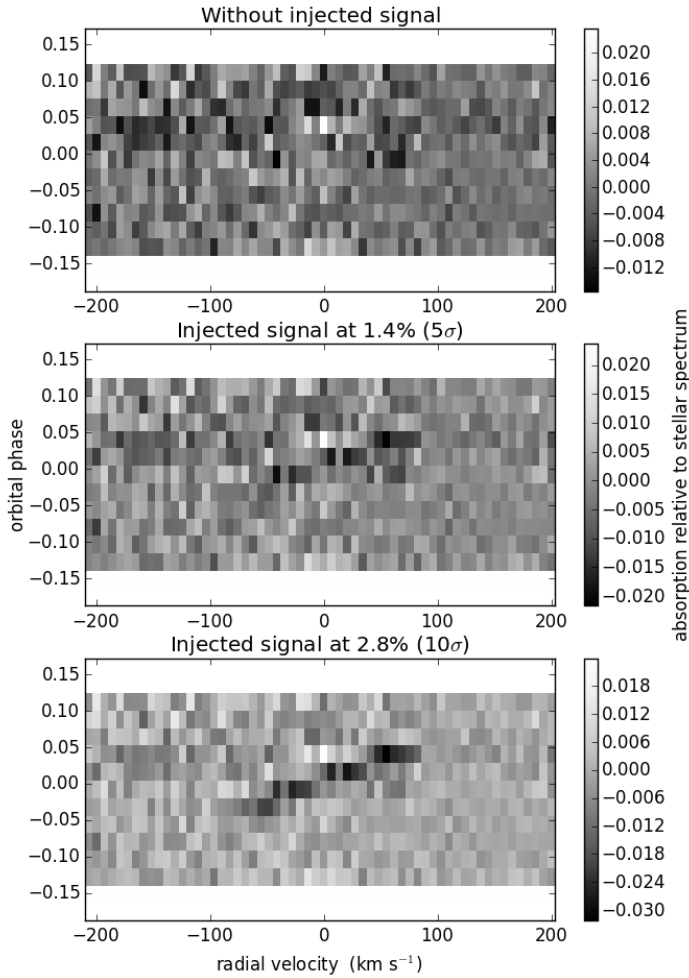


Figure 5.4: Same as Fig. 5.3, except for the calcium near infrared triplet. The middle panel shows an injected signal of 1.4% and the bottom panel shows an injected signal of 2.8%.

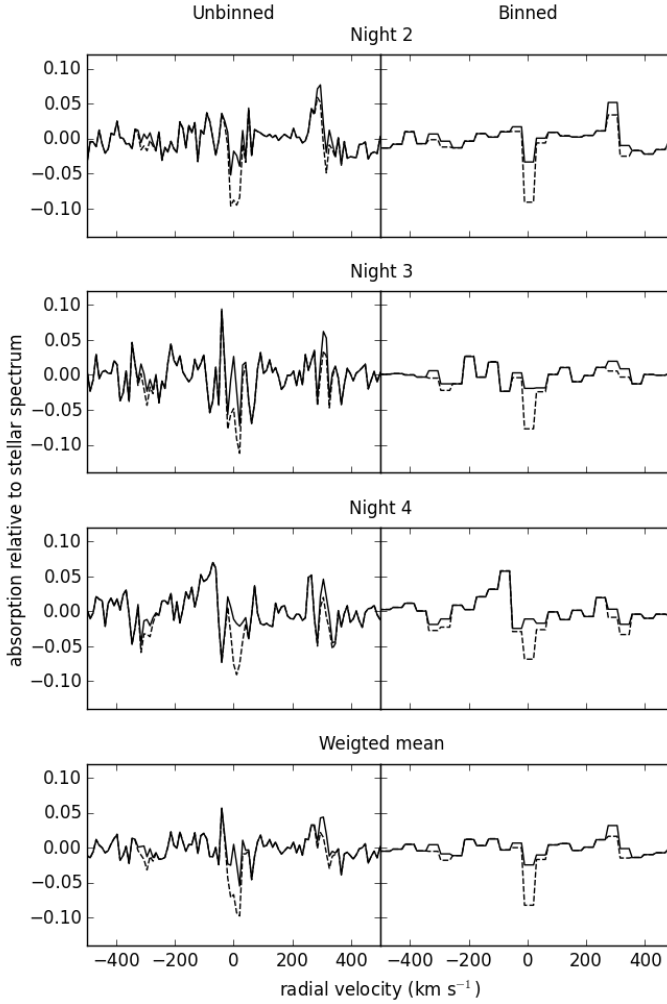


Figure 5.5: Planet transmission spectrum of the combined sodium D lines for Nights 2 to 4 and their combination (bottom panels). The left and right panels show the unbinned and binned (at 0.8\AA or 40 km s^{-1}) data, respectively. The solid and dashed lines indicated the non-injected and injected data (at a 9% depth) respectively.

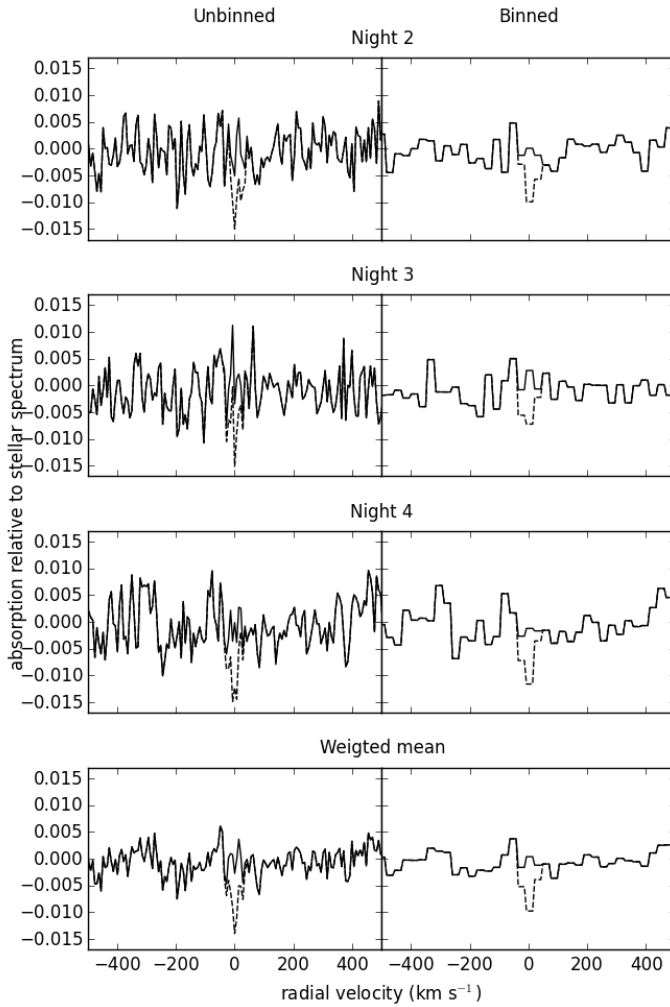


Figure 5.6: Same as Fig. 5.5 but for the ionized calcium near infrared triplet with an injected signal strength of 1.4% relative to the stellar spectrum.

Table 5.2: Spectral line transition parameters.

Spectral line (Å)	f_{ik}	A_{ki} (s^{-1})	Normalisation factor [†]	reference
Na				
5889.95	0.641	6.16×10^7	112.03	1
5895.92	0.320	6.14×10^7	112.28	1
Ca ⁺				
8498.02	0.0120	1.11×10^6	4309.09	2
8542.09	0.072	9.9×10^6	480.65	2
8662.14	0.0597	1.06×10^7	442.69	2

[†] Derived quantity.

Reference 1: Juncar et al. (1981).

Reference 1: Edlén & Risberg (1956).

Values retrieved from NIST Atomic Spectra Database (Kramida et al. 2018).

full-width-at-half-maximum (FWHM) of a Lorentzian line profile to the transition's natural line width given in angular frequency units by the Einstein A coefficient (or spontaneous decay rate, Γ). We then numerically integrated the line profile to find the required normalization factor. The parameters that we used are shown in Table 5.2. In reality, there will also be some kinetic broadening in the gas (see also the discussion below). To approximate this without making assumptions about its pressure and temperature, we convolved the optical depth profile with the instrument resolution to broaden the line. This maximized the broadening while minimizing optical thickness effects.

The line intensity profile, $I(\lambda)$, is estimated from the convolved optical depth profile according to

$$I(\lambda) = I_0(\lambda) \exp(-\tau(\lambda)) \quad (5.3)$$

where $I_0(\lambda)$ is the continuum intensity.

The 5σ upper-limit for sodium corresponds to a 9% absorption depth for the strongest line at 5889.95 Å, which requires an absorbing mass of sodium gas of 3.4×10^9 g assuming it is optically thin. This implies an upper-limit on the total gas mass of 1.4×10^{11} g, assuming that the dust's composition is the same as that of the Earth's crust.

While we assume that all sodium atoms are in the ground state and therefore can produce the targeted absorption lines, this is not the case for ionized calcium. The targeted lines originate from ions in the meta-stable $3d^2D_{3/2}$ and $3d^2D_{5/2}$ states. To estimate the fraction of calcium II ions in these energy states, we created a simple model consisting of three energy levels: E_0 , E_1 , and E_2 . E_0 is the ground state ($4s^2S_{1/2}$), E_1 is the average of the $3d^2D_{3/2}$ and $3d^2D_{5/2}$ states, and E_2 is the average of the $4p^2p_{3/2}^0$ and $4p^2p_{1/2}^0$ states. Transitions from the E_0 level to the E_2 level produce the H and K lines at 3934Å & 3963Å, while transitions from

the E_1 level to the E_2 level produce the near-infrared triplet lines, probed in this study. We also consider the classically forbidden transitions from the E_1 level to the E_0 level, which produce emission at 7291Å and 7324Å.

Spontaneous decay from a high to low energy state occurs at a rate that is proportional to the transition's Einstein A coefficient. Additionally, a transition from a low to high energy state occurs at a rate that is proportional to the rate of photons of energy equal to the energy difference between the states. We calculated the photon rates for the E_0 to E_2 and E_1 to E_2 transitions according to

$$\gamma = \int_{-\infty}^{\infty} F_{\nu} \left(\frac{R_s}{d} \right)^2 \frac{1}{h\nu} a(\nu) d\nu \quad (5.4)$$

where γ is the rate of photons per second, ν is the frequency, F_{ν} is the flux as a function of unit frequency, R_s is the radius of the star K2-22, d is the orbital distance of K2-22 b, h is the Planck constant and $a(\nu)$ is the transition's cross-section, assumed to be a Lorentzian profile of FWHM equal to the transition's natural width. For F_{ν} we used a PHOENIX model spectrum (Husser et al. 2013) of effective temperature $T_{\text{eff}} = 3820$ K that was normalized such that $\int_{-\infty}^{\infty} F_{\nu} = \sigma T_{\text{eff}}^4$, where σ is the Stefan-Boltzmann constant.

Using these calculated transition rates, the steady state solution of the system was found to have 0.26% of its calcium II ions in the infrared-triplet-forming E_1 state.

For the 5σ upper-limit for Ca^+ of 1.4% absorption of the strongest line at 8542.09 Å, the upper-limits on the mass of Ca^+ gas and the total dust mass are 2.1×10^{12} g and 7.1×10^{13} g, respectively.

5.5.2 Dust and gas mass-loss comparison

The dust mass-loss rate required to produce the observed optical transit depth can be estimated based on the rate at which dust particles pass through the area occulting the host star. Following the method described in Rappaport et al. (2014), Sanchis-Ojeda et al. (2015) estimate K2-22 b's mass-loss rate to be 2×10^{11} g s⁻¹.

We can compare our derived gas-mass upper-limits to the dust mass-loss rate if we assume an appropriate timescale for the absorption by the gas. We take this to be the photo-ionization lifetime of the absorbing species, since they are only able to absorb at the probed transitions until they are photo-ionized. We estimated these lifetimes by scaling the values given by Mura et al. (2011) for CoRoT-7 b to K2-22 b, based on the stellar fluxes and the planet orbital distances. The ionization of Na and Ca^+ requires photons of wavelength less than 240 nm and 104 nm, respectively. The flux at these wavelengths is produced by chromospheric emission and, for M-dwarfs, this flux is typically one to two orders of magnitude less than their flux in the u-band (e.g. Stelzer et al. 2013). To allow for the possibility of

high chromospheric emission caused by stellar activity, we conservatively use the Johnson u-band magnitude for this scaling, and find that the u-band flux at K2-22 b is only 27 times larger than what the Sun produces at 1 au distance in the solar system, giving ionization lifetimes of 7.0×10^3 s and 1.2×10^5 s for Na and Ca^+ , respectively. We neglected the photo-ionization timescale of Ca because it is only $\sim 5.0 \times 10^2$ s. For comparison, the photo-ionization lifetimes of Na and Ca at 1 au in the solar system are 1.9×10^5 s and 1.4×10^4 s, respectively (Fulle et al. 2007; Mura et al. 2011). The photo-ionization lifetime of Ca^+ is not well constrained and was estimated by Mura et al. (2011).

From the dust mass-loss rate and photo-ionization lifetimes, we can predict the expected gas column density using

$$M_{gas} = Q \dot{M}_{dust} \tau_{ph} \quad (5.5)$$

where \dot{M}_{dust} is the dust mass-loss rate of K2-22 b, τ_{ph} is the photo-ionization lifetime of the species and Q is the fraction of available dust mass that becomes absorbing gas for a given species. We converted the gas mass into a column density by assuming that the atoms are evenly distributed across the stellar disk. In reality, the gas will probably not cover the entire stellar disk but this is a reasonable assumption because the gas is expected to be optically thin. The expected line strengths as a function of Q are shown in Fig. 5.7 for the sodium D lines and the Ca^+ triplet. Our conservative scaling of the photo-ionization timescale means that Q is an upper-limit.

Fig. 5.7 implies that if the gas were co-moving with the planet, we could have expected to detect absorption by Na and Ca^+ if only $Q = 0.01\%$ and 0.3% of the available lost mass in dust became absorbing gas, respectively. In contrast, it may well be that all of the dust sublimates and becomes gas ($Q = 1$) and that Q may even be >1 because additional gas may be directly lost from the planet. It is clear that under our simplified assumptions there is no evidence for such a high Q value.

5.5.3 Important Caveats: high velocity gas

Our estimated gas absorptions were based on important assumptions: We assume that the dust particles completely sublimate in the time it takes them to drift across the stellar disk. This is a reasonable assumption because the tail's exponential scale length, l , is estimated to be $0.19 < l < 0.48$ stellar radii (Sanchis-Ojeda et al. 2015). We also assume that the gas has the same orbital velocity as the planet. However, this may not be valid as the gas could be highly accelerated by the stellar wind and radiation pressure, giving a very broad spectral line with gas radial velocities ranging from the planet's radial velocity to 100s of km s^{-1} .

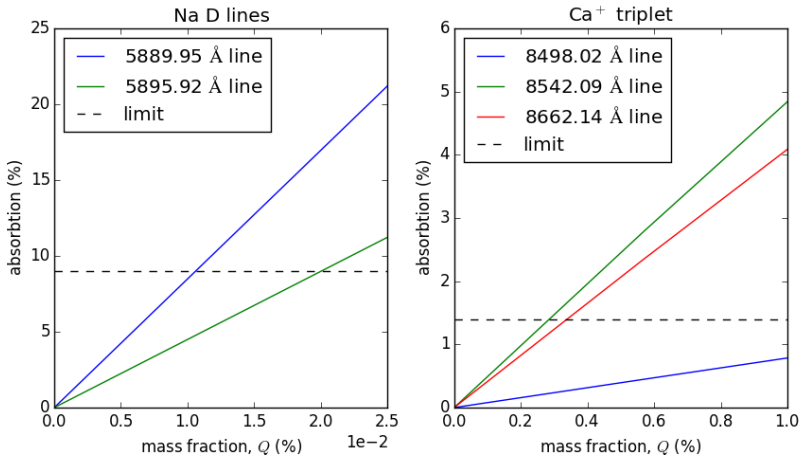


Figure 5.7: Absorption by the Na D lines (left) and the Ca^+ triplet (right) as a function of fraction of available lost mass that becomes absorbing gas, assuming a dust-mass loss rate of $2 \times 10^{11} \text{ g s}^{-1}$, Earth crust abundances and absorption lifetimes equal to the photo-ionization lifetimes of $7.0 \times 10^3 \text{ s}$ and $1.2 \times 10^5 \text{ s}$, respectively.

Acceleration of Ca^+ by the stellar wind

In the absence of a strong planetary magnetic field, ionized calcium (Ca^+) will be dragged along by the stellar wind and quickly reach the velocity of the wind, which is typically on the order of a few hundred km s^{-1} (e.g. Johnstone et al. 2015). However, if the planet were to have a magnetic field, it can trap the Ca^+ ions, preventing them from being swept away by the stellar wind. This may explain the potential detection of Ca^+ around 55 Cancri e in Chapter 2.

The MESSENGER spacecraft detected Ca^+ in the exosphere of Mercury, however it was trapped by Mercury’s magnetic field. It was detected in a narrow region 2 – 3 Mercury radii in the anti-solar direction, exhibiting velocities of hundreds of km s^{-1} . The distribution and velocities of Ca^+ ions is likely due to a combination of magnetospheric convection and centrifugal acceleration (Vervack et al. 2010).

Ionized calcium has also been observed in Sun-grazing comets (e.g Marsden 1967). Additionally, Gulyaev & Shcheglov (2001) detected Ca^+ at distances of 5 – 20 R_{\odot} from the Sun and found that it had radial velocities of 170 – 280 km s^{-1} . They propose that the Ca^+ is produced by the sublimation of orbiting interplanetary dust so that its final velocity is a result of its orbital motion and acceleration by the solar wind.

If the Ca^+ ions are swept away by the stellar wind, their spectral lines will be significantly blue shifted and the line width will be broadened from velocities on the order of the planet’s radial velocity, to the velocity of the stellar wind. This

would strongly hamper the detectability of this gas with the instrumental set-up discussed here.

Stellar radiation pressure

Atoms in an asymmetric photon field will experience a radiation pressure governed by the wavelength-dependent photon density and their absorption cross-sections. If an atom has a radial velocity relative to the photon source, the wavelength-dependency of the absorption cross-section will Doppler-shift accordingly. This can have a large effect e.g. for sodium for which the stellar absorption lines can be very deep. Doppler-shifting these lines significantly can increase the relevant photon flux by an order of magnitude for stellar absorption lines that are 90% deep, causing high accelerations.

Typical accelerations of neutral sodium in the exospheric tail of Mercury are $0.2 - 2 \text{ m s}^{-2}$ (Potter et al. 2007). The final velocity that an accelerated atom can reach depends on the timescale over which it is accelerated, which in the case of neutral atoms equals the photo-ionization lifetime. Cremonese et al. (1997) observed a neutral sodium tail from comet Hale-Bopp when it was at a distance of 1 au, and measured radial velocities of sodium atoms of $60 - 180 \text{ km s}^{-1}$, along its tail of sky-projected length $31 \times 10^6 \text{ km}$. Similarly, radiation pressure accelerates hydrogen that has escaped from the evaporating atmospheres of the hot Jupiters HD 209458 b and HD 189733 b to velocities of approximately 130 km s^{-1} (e.g. Bourrier & Lecavelier des Etangs 2013).

The final velocity that such atoms reach in a given system is expected to be roughly independent of the distance from the host star, since the acceleration scales as d^{-2} , with d the orbital distance, and the ionization time scale as d^2 , the latter counteracting the former.

Comparing the solar spectrum with that of K2-22, using the solar absolute magnitudes from Willmer (2018) and calculating the absolute magnitudes of K2-22 from Sanchis-Ojeda et al. (2015), we find that the optical radiation pressure acting on the neutral sodium atoms at the location of K2-22 b is approximately 150 times higher than for the Earth in the solar system. The stellar u-band flux at K2-22 b is ~ 30 times larger than on Earth, leading to a shorter ionization time scale by a similar factor. Combining these two effects leads to a maximum velocity of $\sim 150/30 = 5$ times larger than that of sodium tails in the solar system. Note that potential effects of high energy activity such as flares are neglected.

We searched for blueshifted signals of Na and Ca^+ using the ratio of the average in-transit to out-of-transit signals in the residual spectra, after removing the stellar and telluric features. Figs. 5.8 and 5.9 show these ratios for Na and Ca^+ , respectively, which do not exhibit any statistically significant features over the radial velocity range of $\pm 1000 \text{ km s}^{-1}$. There are a few outlying points but these are

only due to the high noise in the cores of the targeted lines.

5.5.4 Alternative interpretations

An alternative explanation for our non-detection is that the planet and dust particles may not have a typical terrestrial planet composition. Furthermore, even if the planet overall does have an expected composition, the dust particles may not directly reflect this. By modelling the light curve of the similar disintegrating planet Kepler-1520 b, van Lieshout et al. (2016) found its dust composition to be consistent with corundum (Al_2O_3), which is somewhat surprising because it is not a major constituent of typical terrestrial planet compositions. They suggest that this may be due to the dust grain formation process favouring the condensation of particular species or the planet's surface being covered in a magma ocean that has been distilled to the point of containing mostly calcium and aluminium oxides. A similar process may be occurring on K2-22 b, reducing the abundance of Na and Ca in the dust particles.

Another potential explanation of our non-detection is that all of our observed transits happened to be during quiescent periods of low mass-loss rates. However, based on the observed transit depth variability, we consider this to be unlikely. It would be beneficial for future spectroscopic observations to be carried out simultaneously with optical photometric observations to allow the contemporaneous mass-loss rate to be estimated.

5.6 Conclusions and future outlook

We observed four transits of the disintegrating rocky exoplanet K2-22 b with X-shooter/VLT to search for absorption by gas that is lost directly by the planet or produced by the sublimation of dust particles in its tail. In particular, we focused on the sodium D line doublet (588.995 nm and 589.592 nm) and the Ca^+ near infrared triplet (849.802 nm, 854.209 nm and 866.214 nm).

We detect no significant Na nor Ca^+ associated with the planet, and derive 5σ upper-limits on their possible absorptions of 9% and 1.4% relative to the stellar continuum, respectively, which points to low gas-loss limits compared to the estimated average dust mass loss derived for this system. We suggest that the probed gases are probably accelerated by the stellar wind and radiation pressure, leading to very broad, blueshifted signals with widths up to 900 km s^{-1} , which would be hard to detect with the instrumental set-up used. We searched for such signals in our data but did not find them.

If the signals from gas-loss are indeed very broad, it may be good to search for them using spectrographs with lower spectral resolution, either using ground-based telescopes utilizing multi-object spectroscopy for calibration, or using the

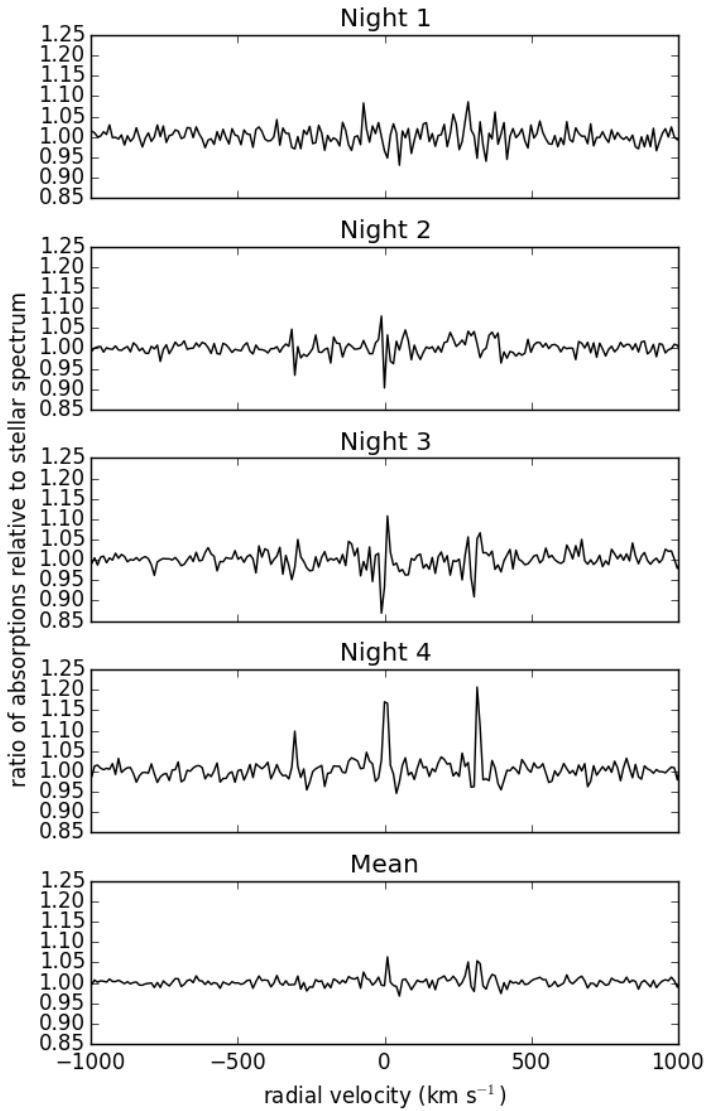


Figure 5.8: Ratio of the average in-transit to out-of-transit signal of blueshifted sodium gas.

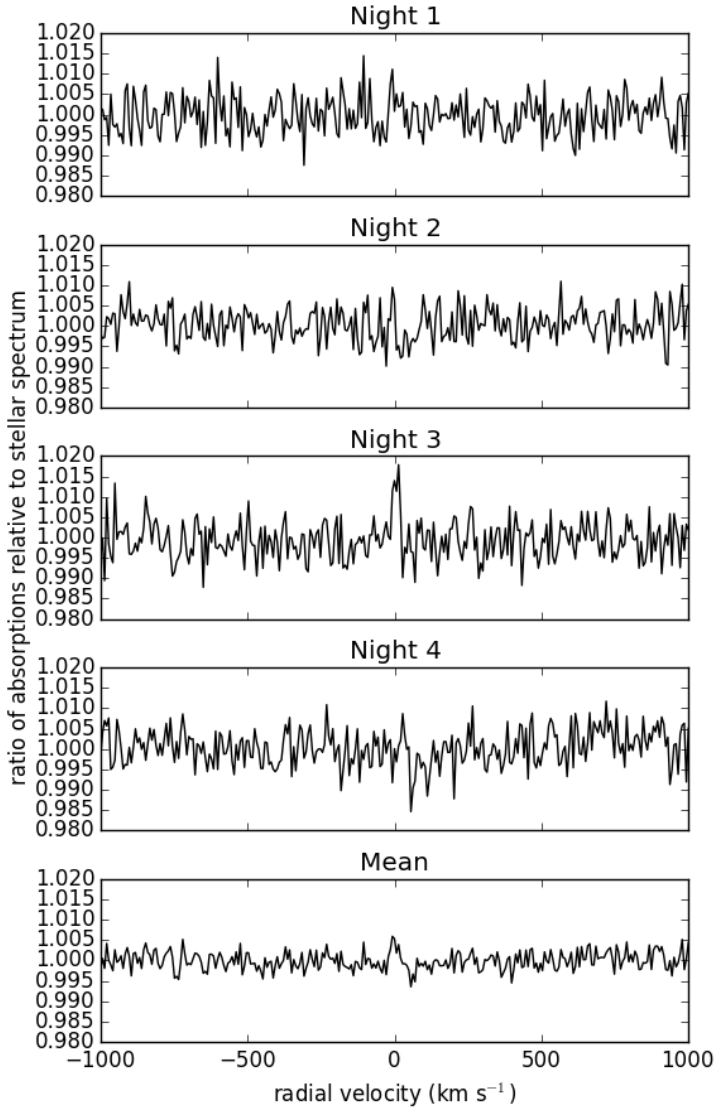


Figure 5.9: Same as Fig. 5.8 except for Ca^+ gas.

future JWST – although the sodium D lines are just outside the wavelength range covered by NIRSPEC. In addition, other species such as O, Mg, Ti, Cr, Mn Fe and Ni could be searched for as they were detected in the circumstellar disk of the white dwarf WD 1145+017, which is thought to originate from disintegrating planetesimals (Redfield et al. 2017). While in principle, the combination of multiple species in the transit model would increase the chance of detection – since many lines can be combined, they may all be at a different levels of sensitivity to radiation pressure and acceleration by the stellar wind, making combination more challenging.

Acknowledgements

A. R. R.-H. is grateful to the Planetary and Exoplanetary Science (PEPSci) programme of the Netherlands Organisation for Scientific Research (NWO) for support. I. A. G. S. acknowledges support from an NWO VICI grant (639.043.107), and from the European Research Council under the European Union’s Horizon 2020 research and innovation programme under grant agreement No. 694513.

Bibliography

- Alonso, R., Rappaport, S., Deeg, H. J., & Pallé, E. 2016, *A&A*, 589, L6
- Bochinski, J. J., Haswell, C. A., Marsh, T. R., Dhillon, V. S., & Littlefair, S. P. 2015, *ApJ*, 800, L21
- Bourrier, V. & Lecavelier des Etangs, A. 2013, *A&A*, 557, A124
- Brogi, M., Keller, C. U., de Juan Ovelar, M., et al. 2012, *A&A*, 545, L5
- Budaj, J. 2013, *A&A*, 557, A72
- Cremonese, G., Boehnhardt, H., Crovisier, J., et al. 1997, *ApJ*, 490, L199
- Croll, B., Rappaport, S., DeVore, J., et al. 2014, *ApJ*, 786, 100
- Edlén, B. & Risberg, P. 1956, *Ark. Fys. (Stockholm)*, 10, 553
- Fulle, M., Leblanc, F., Harrison, R. A., et al. 2007, *ApJ*, 661, L93
- Gulyaev, R. A. & Shcheglov, P. V. 2001, *Physics Uspekhi*, 44, 203
- Haynes, W. M. 2011, *CRC Handbook of Chemistry and Physics*, 92nd edn. (CRC Press)
- Husser, T.-O., Wende-von Berg, S., Dreizler, S., et al. 2013, *A&A*, 553, A6
- Johnstone, C. P., Güdel, M., Lüftinger, T., Toth, G., & Brott, I. 2015, *A&A*, 577, A27
- Juncar, P., Pinard, J., Hamon, J., & Chartier, A. 1981, *Metrologia*, 17, 77
- Kramida, A., Yu. Ralchenko, Reader, J., & and NIST ASD Team. 2018, *NIST Atomic Spectra Database (ver. 5.5.6)*, [Online]. Available: <https://physics.nist.gov/asd> [2018, June 29]. National Institute of Standards and Technology, Gaithersburg, MD.
- Marsden, B. G. 1967, *AJ*, 72, 1170
- Mura, A., Wurz, P., Schneider, J., et al. 2011, *Icarus*, 211, 1
- Murgas, F. 2013, PhD thesis, Departamento de astrofísica, universidad de La Laguna
- Perez-Becker, D. & Chiang, E. 2013, *MNRAS*, 433, 2294
- Potter, A. E., Killen, R. M., & Morgan, T. H. 2007, *Icarus*, 186, 571
- Rappaport, S., Barclay, T., DeVore, J., et al. 2014, *ApJ*, 784, 40
- Rappaport, S., Gary, B. L., Kaye, T., et al. 2016, *MNRAS*, 458, 3904
- Rappaport, S., Levine, A., Chiang, E., et al. 2012, *ApJ*, 752, 1

- Redfield, S., Farihi, J., Cauley, P. W., et al. 2017, *ApJ*, 839, 42
- Sanchis-Ojeda, R., Rappaport, S., Pallè, E., et al. 2015, *ApJ*, 812, 112
- Savage, B. D. & Sembach, K. R. 1991, *ApJ*, 379, 245
- Sharp, C. M. & Burrows, A. 2007, *ApJS*, 168, 140
- Stelzer, B., Marino, A., Micela, G., López-Santiago, J., & Liefke, C. 2013, *Monthly Notices of the Royal Astronomical Society*, 431, 2063
- van Lieshout, R., Min, M., & Dominik, C. 2014, *A&A*, 572, A76
- van Lieshout, R., Min, M., Dominik, C., et al. 2016, *A&A*, 596, A32
- Vanderburg, A., Johnson, J. A., Rappaport, S., et al. 2015, *Nature*, 526, 546
- Vernet, J., Dekker, H., D’Odorico, S., et al. 2011, *A&A*, 536, A105
- Vervack, R. J., McClintock, W. E., Killen, R. M., et al. 2010, *Science*, 329, 672
- Willmer, C. N. A. 2018, *The Astrophysical Journal Supplement Series*, 236, 47

6 | Samenvatting

Het beeld van planeten in een baan rond verre sterren wordt al lang gebruikt om te fascineren en te vermaken in science fiction romans en films. In de afgelopen decennia hebben planeten rond andere sterren dan de zon (zogenoeten ‘exoplaneten’) echter het domein van science fiction verlaten en zijn ze volledig terechtgekomen in het wetenschapsgebied.

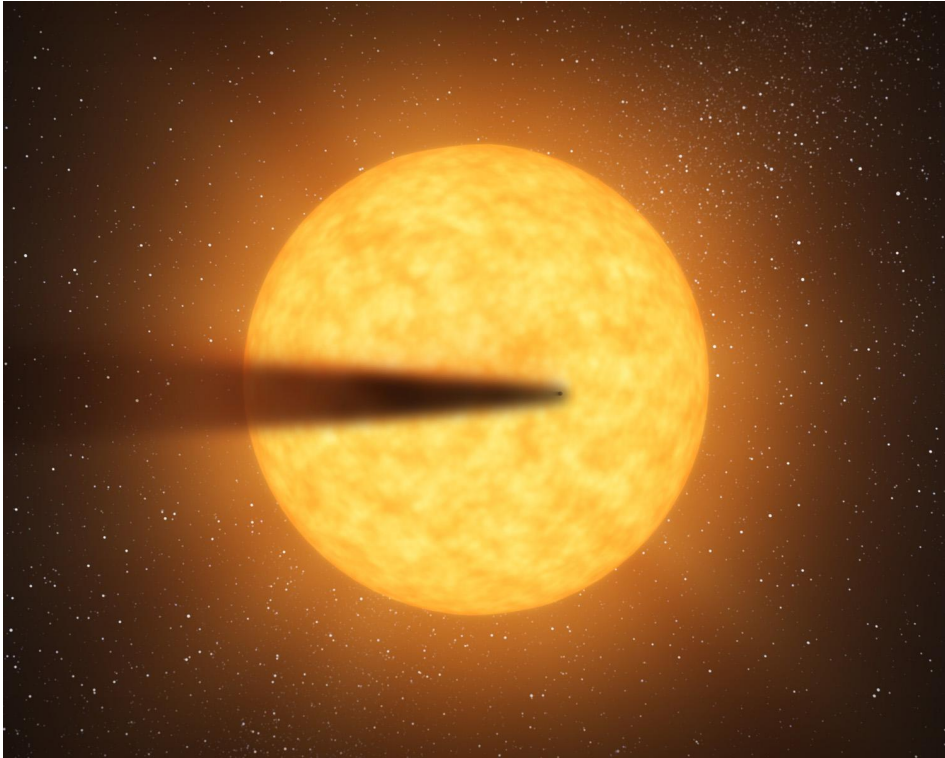
Na ongeveer 25 jaar aan ontdekkingen van exoplaneten, kennen we er nu meer dan 3500. Het is makkelijker om exoplaneten te detecteren die dichtbij hun ster staan, en dus staat de meerderheid van de bekende exoplaneten dicht bij hun ster dan de planeten in ons zonnestelsel bij de zon staan. Over het algemeen hebben planeten die dicht bij hun ster staan ook kortere omlooptijden, waardoor de exoplaneten met de kortste afstanden een omlooptijd van minder minder dan een dag kunnen hebben. Deze planeten bevinden zich zo dichtbij hun sterren dat ze normaal gesproken temperaturen hebben van rond de 2000 °C. Ter vergelijking, de planeet die het dicht bij de zon staat in ons zonnestelsel is Mercurius, met een omlooptijd van 88 dagen en een temperatuur van ongeveer 430° C.

Dit proefschrift richt zich op planeten met korte omlooptijden en overwegend rotsachtige samenstellingen (in tegenstelling tot ‘gasreuzen’ zoals Jupiter). Deze ‘hete rotsachtige exoplaneten’ vertonen vanwege hun hoge temperaturen interessante eigenschappen die ons in staat stellen hun samenstelling in veel meer detail te bestuderen dan mogelijk zou zijn voor koelere rotsachtige planeten.

6.1 Gas van hete rotsachtige planeten

Rotsachtige planeten die dicht bij hun sterren staan, worden blootgesteld aan een sterke sterrenwind en worden tot zeer hoge temperaturen verwarmd.

Als ze geen dikke atmosfeer hebben, kunnen we deze planeten als extreme versies van Mercurius beschouwen. Mercurius heeft een exosfeer (een heel dunne atmosfeer), die wordt geproduceerd doordat het oppervlak sputtert. Dit wordt veroorzaakt door geladen deeltjes met hoge energie van de zonnwind die het oppervlak raken en ervoor zorgen dat atomen vrijkomen. Elementen zoals natrium,



Figuur 6.1: Een impressie van de desintegrerende rotsachtige exoplaneet Kepler-1520 b. Afbeelding van: NASA/JPL-Caltech - NASA Jet Propulsion Laboratory.

magnesium en calcium zijn gedetecteerd in de exosfeer van Mercurius. Gezien de exosferen van hete rotsachtige exoplaneten nog groter kunnen zijn vanwege hun kortere afstanden tot hun sterren, zijn ze mogelijk ook waarneembaar. Het is ook mogelijk dat hun hoge temperaturen ervoor zorgen dat het oppervlak verdampt, waardoor er atmosferen ontstaan die uit minerale dampen bestaan en die mogelijk ook kunnen worden waargenomen.

In de meest extreme gevallen desintegreren hete rotsachtige exoplaneten en produceren ze komeet-achtige stofstaarten. Een artistieke indruk van de desintegrerende rotsachtige exoplaneet, Kepler-1520 b, wordt getoond in Fig. 6.1. Men denkt dat het stof verloren gaat van de planeet als gevolg van de uitzetting en afkoeling van de mineraal-dampen atmosfeer, tot een deel van de damp kan condenseren tot stofdeeltjes en van de planeet worden weggeslept door het resterende uitzettende gas. Daarnaast kan vulkanische activiteit ook een rol spelen. Zowel het gas dat direct van de planeet verloren gaat, als het gas dat wordt geproduceerd door het verdampen van stof in de staart, kan mogelijk worden gedetecteerd.

In al deze gevallen is het gas afkomstig van het oppervlak van de planeet, dus de samenstelling van het gas moet de samenstelling van de planeet weerspiegelen. Daarom bieden deze objecten ons de mogelijkheid om ongekend inzicht te krijgen in de samenstelling van rotsachtige planeten. Deze informatie zou in grote mate bijdragen aan ons begrip van hoe deze planeten werden gevormd en hoe ze zich zullen ontwikkelen.

6.2 Waarnemen van exoplaneet atmosferen

Wanneer licht door een gas doorkruist, worden unieke golflengten geabsorbeerd door atomen of moleculen in het gas. Deze absorpties worden spectraallijnen genoemd en zijn afhankelijk van de samenstelling van het gas. Ze kunnen worden bestudeerd met spectrografen, instrumenten die wit licht verspreiden in hun regenboog van samenstellende kleuren (of golflengten). Met deze techniek kunnen de composities van verre astronomische objecten worden bepaald. Wanneer toegepast op exoplaneten kan het worden gebruikt om de samenstellingen van hun atmosferen te bepalen. Dit kan het makkelijkst worden toegepast op exoplaneten die, vanaf de Aarde gezien, voor hun ster langs gaan (een transit), omdat dat ons in staat stelt te zien hoe het licht van de ster veranderd doordat het door de atmosfeer van de exoplaneet gaat. Dit is echter een uitdaging omdat de moederster en de atmosfeer van de Aarde ook hun eigen spectraallijnen in beeld brengen, die veel sterker zijn dan de spectraallijnen van de atmosfeer van de planeet. Daarom is het noodzakelijk om de bijdragen van de ster en de atmosfeer van de Aarde te verwijderen om de bijdrage van de atmosfeer van de exoplaneet te meten.

Dit kan worden bereikt door gebruik te maken van het feit dat de exoplaneet een veranderende radiële snelheid heeft tijdens de transit, omdat deze bij aan het begin (wanneer de planeet zich voor het eerst voor zijn ster beweegt) een snelheidscomponent naar de waarnemer toe heeft en aan het einde (wanneer de planeet bijna voorbij de schijf van ster is) een snelheidscomponent weg van de waarnemer heeft. Een relatieve snelheid tussen een lichtbron en een waarnemer verandert de golflengte van het waargenomen licht vanwege het Doppler-effect. Daarom zal de veranderende radiële snelheid van de planeet tijdens de transit ertoe leiden dat zijn spectraallijnen wegschuiven van de lijnen van de ster en de atmosfeer van de Aarde.

Deze techniek wordt in hoofdstuk 2 van dit proefschrift gebruikt om te zoeken naar natrium en geïoniseerd calcium in de atmosfeer van de hete super-Aarde, 55 Cancri e. Hoewel we geen definitieve detectie konden maken, hebben we in slechts één van onze waarnemingen een sterk signaal van geïoniseerd calcium gevonden, wat mogelijk suggereert dat de exosfeer ervan variabel is, zoals de exosfeer van Mercurius.

Het wordt ook in hoofdstuk 5 van dit proefschrift gebruikt om gas te zoeken rond de desintegrerende planeet K2-22 b. Hoewel we verwachten dat een grote hoeveelheid gas wordt geproduceerd door het verdampen van de stofstaart, konden we deze niet detecteren. We redeneren dat dit waarschijnlijk te wijten is aan het feit dat de gasatomen aanzienlijk blauwverschoven zijn door stralingsdruk van de ster, waarbij fotonen van licht hun momentum aan de gasatomen overdragen.

6.3 Stofstaarten

De stofstaarten van desintegrerende rotsachtige exoplaneten die voor hun ster langs gaan produceren karakteristieke lichtkrommes die kunnen worden bestudeerd om de eigenschappen van de stofdeeltjes, zoals hun gemiddelde grootte en samenstelling, te begrenzen. Dit is zeer waardevolle informatie omdat het inzicht kan geven in de samenstelling en geofysische processen van de planeet. Deze informatie kan echter alleen worden afgeleid als de vorming en evolutie van de staarten wordt begrepen, en die hangen af van de banen waarop de stofdeeltjes in de staart zich bewegen. De stofdeeltjes ondervinden een stralingsdruk, waardoor ze worden weggeduwd van de ster en de zwaartekracht van de ster, waardoor ze naar de ster worden toegetrokken. Voor de stofdeeltjes in deze staarten is de zwaartekracht van de ster iets sterker dan de stralingsdruk, zodat de totale kracht die op de deeltjes inwerkt een verminderde kracht richting de ster is, waardoor ze in vaste banen blijven. Hoofdstukken 3 en 4 gebruiken een code om lichtkrommes te simuleren door een staart op te bouwen uit virtuele stofdeeltjes die van het planeet oppervlak worden gelanceerd, de staart te laten evolueren onder invloed van stralingsdruk, en tot slot met een stralingstransport code de lichtkrommes te simuleren die de staart zou produceren.

In Hoofdstuk 3 gebruiken we deze code om grenzen te zetten op de snelheid waarmee de stofdeeltjes worden gelanceerd van de planeet, waardoor mogelijk inzicht wordt verkregen in het geofysische mechanisme dat het massaverlies veroorzaakt. We onderzoeken ook hoe de hoeveelheid stof in de staart de diepte van de transit beïnvloed op verschillende golflengten, en zien dat staarten met meer stof minder variatie vertonen met golflengte, wat mogelijk verklaart waarom slechts enkele waarnemingen op meerdere golflengtes een dergelijke variatie zien.

In hoofdstuk 4 passen we deze code aan om te onderzoeken hoe de banen van de stofdeeltjes worden beïnvloed door zelfafscherming in de staart, wat betekent dat stofdeeltjes aan de ster-zijde van de staart een deel van het sterlicht absorberen, waardoor deeltjes die verder van de ster staan in de staart minder licht ontvangen en dus een zwakkere stralingsdruk ervaren en minder snel verdampen. We vonden dat zelfafscherming in sommige gevallen een grote impact heeft op de vorm van de staart en dat het stof een samenstelling moet hebben die uit zichzelf snel verdampt

om het waargenomen gebrek aan correlatie tussen de dieptes van opeenvolgende transits te reproduceren.

7 | Summary

The concept of planets orbiting distant stars has long been used to fascinate and entertain in science fiction novels and films. However, in recent decades, extrasolar planets (or exoplanets) have left the realm of science fiction, and entered squarely into the realm of science fact.

After about 25 years of exoplanet discoveries, we now know of more than 3500 exoplanets. It is easier to detect exoplanets that have short orbital distances from their host stars, so the majority of these known exoplanets have orbits that are closer to their host stars than any planet in our solar system is to the Sun. In general, planets that are nearer to their host stars also have shorter orbital periods, so the closest of these exoplanets can have orbital periods of less than a day. These planets are at such short distances from their host stars, that they typically have temperatures on the order of 2000 °C. For comparison, the nearest planet to the Sun in our solar system is Mercury, which has an orbital period of 88 days and a day-side temperature of approximately 430 °C.

This thesis focuses on short orbital period planets that have mostly rocky compositions (in contrast to ‘gas giant’ planets like Jupiter). These ‘hot rocky exoplanets’ exhibit interesting properties due to their high temperatures that allow their composition to be studied in far greater detail than would be possible for cooler rocky planets.

7.1 Gas from hot rocky planets

Rocky planets that are close to their host stars are exposed to strong stellar winds and are heated to very high temperatures.

If they do not have thick atmospheres, they may be like extreme versions of Mercury, which has an exosphere (like a very thin atmosphere), that is produced by sputtering of its surface. This is when high energy charged particles from the Sun’s solar wind impact the surface material and cause atoms to be released. Elements like sodium, magnesium and calcium have been detected in the exosphere of Mercury. Considering that the exospheres of hot rocky exoplanets may be even

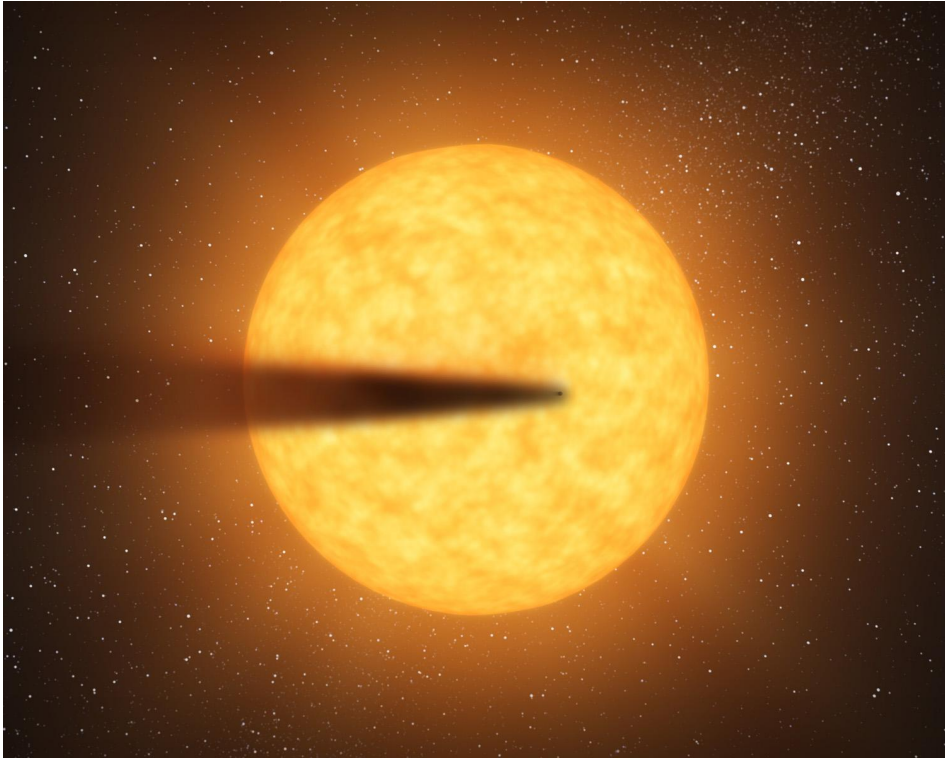


Figure 7.1: Artist's impression of the disintegrating rocky exoplanet, Kepler-1520 b. Image credit: NASA/JPL-Caltech - NASA Jet Propulsion Laboratory.

larger due to their shorter orbital distances from their host stars, they are also potentially detectable. It is also possible that their high temperatures will cause their surfaces to vaporise, producing atmospheres consisting of mineral vapours that can also potentially be detected.

In the most extreme cases, hot rocky exoplanets actively disintegrate and produce comet-like dust tails. An artist's impression of the disintegrating rocky exoplanet, Kepler-1520 b, is shown in Fig. 7.1. It is thought that the dust is lost from the planet as a result of its mineral vapour atmosphere expanding and cooling until some of the vapour can condense into dust grains and be dragged away from the planet by the remaining expanding gas. Additionally, volcanic activity may also play a role. Both the gas that is directly lost from the planet, and the gas that is produced by the sublimation of dust in the tail can potentially be detected.

In all of these cases the gas originates from the surface of the planet, so its composition must reflect the composition of the planet. Therefore, these objects offer us the possibility of gaining unprecedented insight into the composition of

rocky planets. This information would greatly contribute to our understanding of how these planets formed and how they will evolve.

7.2 Observing exoplanet atmospheres

When light passes through a gas, unique wavelengths are absorbed by atoms or molecules in the gas. These absorptions are called spectral lines and depend on the composition of the gas. They can be studied with spectrographs which are instruments that disperse white light into its rainbow of constituent colours (or wavelengths). This technique allows the compositions of distant astronomical objects to be determined. When applied to exoplanets, it can be used to determine the compositions of their atmospheres. It can be most readily applied to exoplanets that transit (or pass in front of their host stars) as seen from Earth, because they allow us to observe how the star's light is changed by passing through the exoplanet's atmosphere. However, this is challenging because the host star and the Earth's atmosphere also imprint their own spectral lines, which are much stronger than the spectral lines from the planet's atmosphere. Therefore, it is necessary to remove the contributions of the host star and Earth's atmosphere to measure the contribution of the exoplanet's atmosphere.

This can be achieved by exploiting the fact that the exoplanet has a changing radial velocity during transit because at ingress (when it first moves in front of its host star), it will have a component of its velocity towards the observer and at egress (when it starts to move past the disk of its host star), it will have a component of its velocity away from the observer.

A relative velocity between a light source and an observer changes the wavelength of the observed light, due to the Doppler effect. Therefore, the changing radial velocity of the planet during transit will result in its spectral lines being shifted away from the lines of its host star and the Earth's atmosphere.

This technique is used in Chapter 2 of this thesis to search for sodium and ionized calcium in the atmosphere of the hot super-Earth, 55 Cancri e. While we were not able to make a definitive detection, we detected a strong signal of ionized calcium in only one of our data sets, tentatively suggesting that its exosphere may be variable, like the exosphere of Mercury.

It is also used in Chapter 5 of this thesis to search for gas around the disintegrating planet, K2-22 b. While we expect a large quantity of gas to be produced by the sublimation of its dust tail, we were not able to detect it. We argue that this is likely due to the gas atoms being significantly blueshifted by radiation pressure from the host star, caused by photons of light transferring their momentum to the gas atoms.

7.3 Dust tails

The dust tails of transiting disintegrating rocky exoplanets produce characteristic transit light curves that can be studied to constrain properties of the dust particles such as their average size and composition. This is very valuable information because it can give insight into the composition and geophysical processes of the planet. However, this information can only be inferred if the formation and evolution of the tails is understood, which depends on the orbital dynamics of their constituent dust particles.

The dust particles experience a radiation pressure, which acts to push them away from the host star and the host star's gravity, which acts to pull them towards the host star. For the dust particles in these tails, the star's gravity is somewhat stronger than the radiation pressure, so the overall force that acts on the particles is a reduced force towards the star, allowing them to stay in bound orbits.

Chapters 3 and 4 use a code to simulate transit light curves by building up a tail by ejecting virtual dust particles from the surface of a planet, letting the tail evolve under the influence of radiation pressure, then using a radiative transfer code to simulate the transit light curve that it would produce.

In Chapter 3, we use this code to derive some approximate constraints on the velocity with which the dust particles are ejected from the planet, potentially giving insight into the geophysical mechanism that causes the mass-loss. We also investigate how the amount of dust in the tail can affect the transit depth in different wavelengths and find that tails with more dust show less transit depth variation in different wavelengths, potentially explaining why only some multi-wavelength observations find such a variation.

In Chapter 4 we adapt this code to investigate how the orbital trajectories of the dust particles are affected by self-shielding within the tail, which is when dust particles on the edge of the tail facing the host star absorb some of the star's light, resulting in the particles deeper in the tail receiving less light and experiencing a weaker radiation pressure and reduced sublimation rate. We found that self-shielding can have a significant influence on the tail morphology in some cases and that dust compositions with fast intrinsic sublimation rates may be required to reproduce the observed lack of correlation between consecutive transit depths.

Curriculum Vitae

I was born on the 6th of August 1991 in Christchurch, Canterbury, New Zealand, and grew up in the neighbouring satellite town of Rolleston. In my youth, this area had relatively little light pollution, which may have contributed to my interest in astronomy.

I have always been interested in science, but it was during high school at Hagley Community College when I started to favour physics and astronomy. During my latter years of high school, I became involved with the Canterbury Astronomical Society, where I learned how to use my own small reflecting telescope, used larger amateur telescopes and volunteered at public open nights at the R. F. Joyce Observatory in West Melton.

I started studying physics and astronomy at the University of Canterbury in 2010 where I completed a four-year Bachelor of Science with First Class Honours degree¹ in astronomy. While at the University of Canterbury, I did my bachelor and honours research projects and a summer research project with Professor Peter Cottrell on investigating the chemical evolution of giant stars in globular clusters with multi-object spectroscopic data from the Robert Stobie Spectrograph on the Southern African Large Telescope. During the university summer break of 2010, I worked as a tour guide at the astro-tourism company Earth and Sky Ltd. in the New Zealand town of Lake Tekapo, located in the Aoraki Mackenzie International Dark Sky Reserve. In this role I showed visually appealing astronomical objects to visitors through telescopes, while explaining their significance and physical properties.

I was awarded summer research scholarships at the Australian National University in 2012 and 2013. My first project there was supervised by Dr. Elizabeth Wylie de Boer and involved testing the spectral fitting codes used in the GALactic Archaeology with HERMES (GALAH) project. My second project there was supervised by Dr. Frank Mills and involved benchmarking a photochemistry code that simulated the upper atmosphere of Venus.

¹This is a typical Ph.D. preparation programme in New Zealand and Australia, and is similar to the four year integrated masters degree in the UK.

I started my Ph.D. at Leiden Observatory in June 2014 under the guidance of Professors Ignas Snellen and Christoph Keller. During my Ph.D., I have worked on: searching for gas in the exosphere of the hot super Earth, 55 Cancri e (Chapter 2), simulating the dust tail of the disintegrating rocky exoplanet, Kepler-1520 b (Chapters 3 & 4) and searching for gas that was lost from the disintegrating rocky exoplanet, K2-22 b (Chapter 5). During this time, I have presented my research at international conferences in Canada, the United Kingdom, Switzerland, and the Czech Republic.

As of the 26th of November 2018, I will be a post doctoral researcher in the group of Professor Ray Jayawardhana at Cornell University in the United States of America.

List of publications

- **A. R. Ridden-Harper**, I. A. G. Snellen, C. U. Keller, P. Mollière, *Search for gas from the disintegrating rocky exoplanet K2-22b*, A&A, submitted
- **A. R. Ridden-Harper**, C. U. Keller, M. Min, R. van Lieshout, I. A. G. Snellen, *Chromatic transit light curves of disintegrating rocky planets*, A&A, in press (2018)
- R. van Lieshout, M. Min, C. Dominik, M. Brogi, T. de Graaff, S. Hekker, M. Kama, C. U. Keller, **A. R. Ridden-Harper** and T. I. M. van Werkhoven, *Dusty tails of evaporating exoplanets II. Physical modelling of the KIC 12557548b light curve*, A&A 596, A32 (2016)
- **A. R. Ridden-Harper**, I. A. G. Snellen, C. U. Keller, R. J. de Kok, E. Di Gloria, H. J. Hoeijmakers, M. Brogi, M. Fridlund, B. L. A. Vermeersen and W. van Westrenen, *Search for an exosphere in sodium and calcium in the transmission spectrum of exoplanet 55 Cancri e*, A&A 593, A129 (2016).

Acknowledgements

The road leading to the completion of a Ph.D. is sometimes bumpy. However, my journey along this road was made a little less bumpy by some special people, many of whom are mentioned here.

I would first like to thank my supervisors, Ignas Snellen and Christoph Keller. I will always be grateful to both of you for your patience, approachable personalities, and guidance in all aspects of academic life.

Next, I would like to thank my parents. You always did whatever you could to help me succeed and encouraged me to follow my dreams, even though they took me to the other side of the world. I am also grateful to my brother, Ryan. Thanks for your support and for always being willing to talk about whatever was on my mind. Good luck with finishing your own Ph.D.!

I would also like to thank the people that keep the institute running smoothly. In particular, thanks to Evelijn Gerstel for her helpful insight into financial matters, the secretariat staff for their support on a wide range of day-to-day activities, and Erik Deul and the computer systems support group for quickly resolving my technical issues. I am also grateful to Xander Tielens for his support and encouragement in the final months of my Ph.D.

To my colleagues in the exoplanet research group: Geert Jan Talens, Dilon van Serindag, Sebastiaan Haffert, Patrick Dorval, Paul Mollière, Francisco Javier Alonso Floriano, Alex Cridland, Aurélien Wyttenbach and to those who were previously part of the group: Vincent van Eylen, Paul Wilson, Jens Hoeijmakers, Emanuele Di Gloria, Henriette Schwarz, Remco de Kok, Matteo Brogi, Julien Spronck, Anna-Lea Lesage & Jayne Birkby, I have followed your research with interest and have greatly enjoyed and benefited from your suggestions and comments on my own work. Thanks also to Michiel Min, Rik van Lieshout and Ernst de Mooij for our fruitful collaborations.

To Claudia-Corina Giese, Vincent Kofman, Kaustubh Hakim, Kateryna (Katya) Frantseva, Lucas Patty, Edgar Steenstra, Loïc Rossi, Yue Zhao and Maaïke Damen and all my other colleagues in the Planetary and ExoPlanetary Science (PEPSci) network, thanks for all of the great interdisciplinary presentations and discussions

that really broadened my perspectives on planetary science. Special thanks to: Alex Cridland, Bram Mooij, Nina Poplawska-Kopacz and Teresa Steinke for taking over the organizational duties now that the ‘old guard’ is leaving.

To the bachelor and masters students that I have had the pleasure of helping to supervise: Esmee Stoop, Michelle Willebrands, Matt Fields, and Jianfei Liang, I really enjoyed our stimulating discussions and being impressed by your nice results!

To the friends that I made during my Ph.D.: Chris Barber (Batman), Zoe Sharp, Christian Eistrup, Iris Nijman, Ann-Sofie Bak Nielsen, Jeroen Franse, Eva Bøgelund, Niels Ligterink, Michael Wilby, Charlotte Moss, Nico Blok-Salinas, Wijnand Blok-Salinas, Jorryt Matthee, Valeria Korol, Luke Maud, Aayush Saxena, Mieke Paalvast, Gabriela (Gabby) Calistro Rivera, Marco Velliscig, Soumyajit (Jit) Mandal, Andrej Dvornik, Eleonora Zari, Clément Bonnerot, Allison Hill, David Carton, Heather Andrews Mancilla, Sierk van Terwisga, Christos Georgiou, Maria Cristina Fortuna, Pedro Salas Munoz, Santiago Torres Rodriguez, Kimberly Emig, Joshua (Josh) Albert & Tommaso Marchetti. I am very grateful for all of the fun and good times that we’ve had with things like getting ice-cream after lunch, movie and board game nights, borrels, parties, and complaining about the Dutch weather ;) Also, thanks to Marissa Rosenberg and Tiffany Meshkat for really making me feel welcome during my first few months in Leiden.

To my office mates, past and present: Tim Shimwell, Yannick Bahé, Bruno Ribeiro, Caroline D’Angelo & Adam Muzzin, thanks for making our office a pleasant place to work. Also, thanks to my ex-officemate Ricardo Herbonnet for our interesting discussions and strolls in the fresh air.

To my old University of Canterbury friends Robert Culling, Edward Ashton and Benedict Morrissey, thanks for encouraging me with your interest in my research. Also, thanks to my fellow Kiwis in the Netherlands: Aaron Greenwood, Alexander Rimoldi and Alan Heays, for discussing New Zealand matters with me and letting me hear that familiar accent.